Copyright
by
Chen Shi
2011

The Dissertation Committee for Chen Shi
certifies that this is the approved version of the following dissertation:

Fatigue Damage Prediction in Deepwater Marine Risers due to Vortex-Induced Vibration

Committee:

Lance Manuel, Supervisor

Loukas F. Kallivokas

Spyros A. Kinnas

Edward J. Powers

Michael A. Tognarelli

Fatigue Damage Prediction in Deepwater Marine Risers due to Vortex-Induced Vibration

by

Chen Shi, B.S., M.S.

DISSERTATION

Presented to the Faculty of the Graduate School of

The University of Texas at Austin

in Partial Fulfillment

of the Requirements

for the Degree of

DOCTOR OF PHILOSOPHY

THE UNIVERSITY OF TEXAS AT AUSTIN

August 2011

To my wife, Tian Huang, and my daughter, Taozhuo Shi.

Acknowledgments

Upon the finishing of this long doctoral study journey, I am thankful for many people who have been with me all the way along. It has been a great privilege to spend several years in the Department of Civil, Architectural and Environmental Engineering at The University of Texas at Austin, and its members will remain dear to me.

First, I would like to express my deep appreciation and gratitude to my advisor, Dr. Lance Manuel, for his guidance, encouragement, insight, and patience during my graduate studies at UT Austin. He inspired me in many ways. He encouraged me to grow as an independent thinker and gave me the opportunity to develop my own individuality and self-sufficiency by allowing me to work with such independence. I would also like to thank Drs. Loukas Kallivokas, Spyros Kinnas, Edward Powers, and Michael Tognarelli for serving on my doctoral dissertation committee, and for their time and valuable input.

I am grateful for the generous financial support provided by BP American Production Co. which made my doctoral studies possible. I must thank Drs. Michael Tognarelli, Vasileios Gkaras, Hugh Banon, and Mr. Tammer Botros of BP American Production Co. Their insights and assistance shed light on this work. I must also acknowledge the Norwegian Deepwater Programme (NDP) Riser and Mooring project for allowing me to use the data of Riser High Mode VIV tests. In addition, I would like to thank Jinkyoo Park, my fellow graduate student, for his effort and assistance regarding solving several technical problems.

Finally, I would like to thank my wife, Tian Huang. Her support, encouragement, patience and love were the bedrock upon which the past ten years of my life have been built. I am indebted with my parents, Xinkui Shi and Enfang Peng, for their faith in me and their unconditional love for the past thirty years. I also would like to thank Tian's parents, Xuchun Huang and Guijun Li for their unending encouragement and support. Let me finish with a special thank to my daughter, Taozhuo Shi, for the joys and responsibilities she brought to my life. Most importantly, her staggering steps motivated me to speed up at the finishing line.

Fatigue Damage Prediction in Deepwater Marine Risers due to Vortex-Induced Vibration

Publication No. __________________

Chen Shi, Ph.D.
The University of Texas at Austin, 2011

Supervisor: Lance Manuel

Slender marine risers used in deepwater applications often experience vortex-induced vibration (VIV). Fatigue damage associated with VIV is of great concern to offshore engineers; however, it has proven difficult to predict this fatigue damage using existing semi-empirical tools. Similarly, approaches based on theoretical and computational fluid dynamics (CFD) generally rely on simplified assumptions on the fluid flow fields and response characteristics. To gain an understanding of VIV and associated fatigue damage, full-scale field monitoring campaigns as well as reduced-scale laboratory experiments are often carried out, wherein the riser response in the form of strains and/or accelerations is recorded using an array of a limited number of sensors distributed over the length of the riser. Simultaneously, current velocities at a proximate location are also recorded. Such measurements generally reveal complex characteristics of the dynamic response of a riser undergoing VIV, including the presence of multiple vibration harmonics, non-stationary behavior, and the existence of sustained or intermittent traveling wave patterns. Such complex features, often not accounted for in some semi-empirical and theoretical approaches, are critical to take into consideration for accurate fatigue damage estimation.

In this study, several empirical methods are employed to first reconstruct the response of an instrumented riser and, then, estimate fatigue damage rates over the entire span of the riser based on a limited number of discrete measurements. The methods presented employ the measured data in different ways. One method, referred to as "weighted waveform analysis" relies on expressing the riser response as a summation of several weighted waveforms or riser modes; the mode shapes are "assumed" and time-varying weights for each mode are estimated directly from the measurements. The riser response over the entire span is reconstructed based on these assumed mode shapes and estimated modal weights. Other methods presented extract discrete mode shapes from the data directly. With the help of interpolation techniques, continuous mode shapes are formed, and the riser response is again reconstructed. Fatigue damage rates estimated based on the reconstructed strains obtained using the various empirical methods are cross-validated by comparing predictions against direct measurements available at the same locations (but not used in the analyses). Results show that the empirical methods developed here may be employed to accurately estimate fatigue damage rates associated with individual recorded segments of measurements.

Finally, a procedure for prediction of long-term fatigue damage rates of an instrumented marine riser is presented that relies on combining (multiplying) the fatigue damage rates associated with short recorded segments

for specific current profile types, with the relative likelihood of different incident current profiles, and integration over all current profiles. It should be noted that the empirical approaches to fatigue damage estimation presented in this study are based only on measured data; also, they explicitly account for different riser response characteristics and for site-specific current profiles developed from metocean studies. Importantly, too, such estimation procedures can easily accommodate additional data that become available in any ongoing field monitoring campaign to improve and update long-term fatigue damage prediction.

Table of Contents

List of Tables

List of Figures

Chapter 1

Introduction

1.1 Background

Increasing demands for energy, especially oil and gas, are pushing the petroleum industry to explore in increasingly deeper waters in search for petroleum resources (see Fig. 1.1). In 2010, according to a survey conducted, there were 262 operating/installed production vessels in the world. Among them, 48 were located in the Gulf of Mexico—these included Petronius (compliant tower, water depth 531 m), Magnolia (tension leg platform (TLP), $1,425$ m), Perdido (spar, $2,383$ m), and Independence Hub (semi-submersible floating production unit (Semi-FPU), 2,414 m) [61]. Drilling risers, as well as other slender structural components of deepwater production systems, such as mooring cables, TLP tension members, and suspended spans of pipelines, can experience vortex-induced vibration (VIV). Large-amplitude VIV can lead to collisions among closely spaced slender structural members. More importantly, VIV is a major contributor to fatigue damage in these structural members. Fatigue failure, if it occurs, can cause suspension of production, loss of revenue, or even marine pollution. Thus, VIV is a major concern in all stages of deepwater oil production.

A marine riser is a critical component of an offshore drilling and production system. It connects the well structure on the seabed and the platform at the sea surface, and conveys fluids between them [2]. When studying vortex-induced vibration (VIV) response, risers are often simplified as long flexible cylinders. Vortex-induced vibration of slender cylinders has been extensively studied over the past 50 years and much progress has been made in improving our understanding of the phenomenon. Experiments using short rigid cylinders in well-controlled laboratory conditions were often used to assess the conditions of synchronization of vortex shedding on a cylinder's motions, and to measure the hydrodynamic forces exerted on the cylinder during vortex shedding. Experiments using long flexible cylinders, exposed to spatially varying fluid flow fields, paved the way for studies of the physics behind VIV of slender marine structures in real ocean currents. These studies have significantly improved our understanding of VIV encountered by marine structures and have led to the development of semi-empirical/analytical tools for prediction of VIV occurrence and associated response of such marine structures.

Semi-empirical computer programs, such as SHEAR7 [56], VIVA [53], and VIVANA [32], have the ability to capture some characteristics of the cross-flow (CF) response of slender structures undergoing VIV. Given the current profile and physical properties of the cylinder as inputs, these computer programs predict the steady cross-flow vibration response at the fundamental vortex-shedding frequency (i.e., the Strouhal frequency). However, complex response characteristics often observed in flexible cylinder experiments and drilling riser monitoring campaigns, such as the presence of higher harmonics (vibration at frequencies that are multiples of the Strouhal frequency), traveling waves, and non-stationary behavior of the cylinder's response, usually cannot be accurately represented by these computer programs. Ignor-

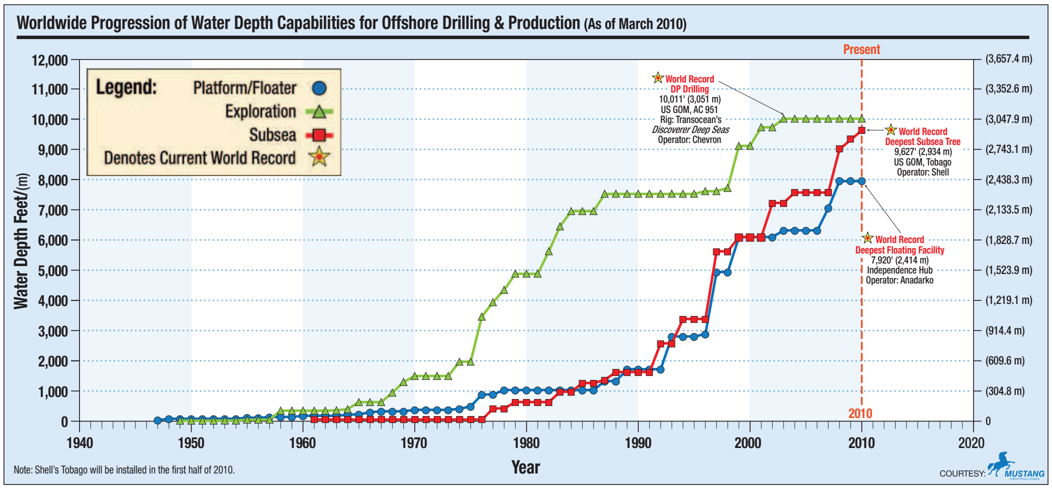

Figure 1.1: Worldwide advances in capabilities for offshore drilling and production as a function of time and water depth (as of March 2010) [61].

ing these important characteristics in VIV response computations can lead to large errors in predicted fatigue damage rates. For example, SHEAR7-V4.5 does not always correctly predict the location and magnitude of the maximum root-mean-square (RMS) strains along the length of a long cylinder; the predicted fatigue damage rate based on only including vibrations around the Strouhal frequency was found to be twenty times smaller than the fatigue damage rate inferred from measurements at a location on an instrumented riser where the maximum RMS strain value was measured [26]. When utilized to analyze measurements from full-scale drilling risers without VIV suppression, SHEAR7-V4.5 overpredicted the maximum fatigue damage rate, on average, by a factor of thirty, when compared with measured values [52].

In the past decade, numerous reduced-scale model riser experiments have been conducted by measuring the VIV response at discrete locations along long flexible cylinders. It is also becoming increasingly common to install data loggers onto full-scale drilling risers to monitor risers excited by real ocean currents as part of field monitoring campaigns. The objectives of this study are twofold: (i) to deepen our understanding of the phenomenon of VIV of long flexible cylindrical structures, such as drilling risers, by proposing robust empirical methods for analysis of measured data; and (ii) to accurately reconstruct the VIV response over the entire span of a cylinder and estimate fatigue damage rates based on the discrete measurements and the empirical analysis tools developed. The ultimate goal is, given measurements of the riser response and accompanying current flow conditions, to establish "short-term" fatigue damage rate distributions conditional on current type; these "short-term" fatigue damage distributions, combined with current profile/type probability distributions or occurrence likelihoods, can yield integrated "long-term" fatigue damage rates over the entire span of the monitored riser.

1.2 Vortex-Induced Vibration

1.2.1 Vortex Shedding and Vortex-Induced Vibration

When fluid flow encounters a cylinder, or any other bluff body, the fluid is forced to deviate from its original path and move around the cylinder. The flow pattern on the leeward (downstream) side of the cylinder depends on the Reynolds number (Re). As illustrated in Fig. 1.2, at $Re < 5$, the fluid flows smoothly over the cylinder and remains unseparated on the downstream side. In the regime, $5 < Re < 40$, a pair of vortices are formed and remain attached to the cylinder. Increasing to $Re > 40$, a street of vortices with opposite rotations are periodically formed and shed behind the cylinder; these vortices

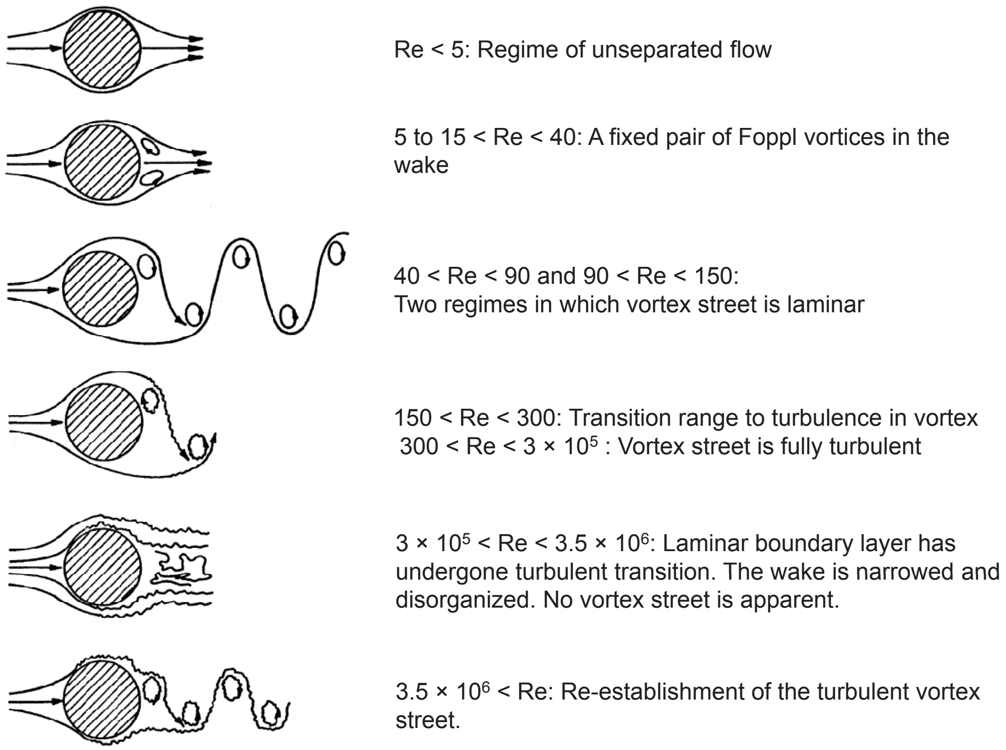

Figure 1.2: Regimes of fluid flow past a circular cylinder [34].

make up what is referred to as a Kármán vortex street.

The formation and shedding of vortices alters the local pressure around the cylinder, exerts alternating forces on it at the frequency of the vortex shedding, and causes the cylinder to deflect or vibrate if it is allowed to do so. If a natural frequency of the cylinder is close to the frequency of vortex shedding, the vortex shedding alters the natural frequency by modifying the added mass; as well, the vibration of the cylinder alters the frequency of the vortex shedding. The interaction between the vortex shedding and the cylinder vibration causes the frequency of vortex shedding and the natural frequency of the cylinder coalesce, leading the cylinder to vibrate with large amplitude in a direction transverse to the direction of the incoming flow (this transverse direction is termed the cross-flow direction). This phenomenon, characterized by the vortex shedding captured by or synchronized with the cylinder's motion, is referred to as lock-in synchronization. The sustained large-amplitude vibration is called vortex-induced vibration (VIV).

The forces exerted on a cylinder by vortex shedding have components in two orthogonal directions. The lift force, which is in the cross-flow (CF) direction (i.e., the direction transverse to the incoming flow direction), has a frequency equal to the frequency of the vortex shedding. The drag force, which is in the in-line (IL) direction (i.e., the direction of the incoming flow), has a frequency that is two times that of the frequency of the vortex shedding. This is because during one cycle of vortex shedding, for the CF direction, a vortex or a group of vortices is shed from one side of the cylinder, and then a vortex or a group of vortices is shed from the other side of the cylinder; while, with respect to the IL direction, both pairs of vortices are shed from the downstream side. As a result, the frequency of the drag force is two times that of the frequency of the lift force; under lock-in conditions, the frequency of IL vibration is two times that of the frequency of CF vibration.

Vortex-induced vibration (VIV) of a cylinder is self-regulating or self-limiting, i.e., when the amplitude of the vibration increases to a certain level, the energy transferred to the cylinder and the energy transferred out of the cylinder reach a balance; the amplitude of the vibrations will then not increase any more but will remain stable. The maximum observed CF vibration amplitude is about $1.5D$ (where D is the diameter of the cylinder) and the maximum observed IL vibration amplitude is about $0.5D$; these maximum values depend on the mass, damping, etc. Thus, unlike unstable flow-induced vibrations, such as in the case of flutter and galloping, the self-limiting nature of VIV will generally not cause stresses in the cylinder to exceed yield strength levels of the material involved. Instead, it is fatigue damage and fatigue limit states that are of concern particularly if VIV response episodes are sustained for long periods of time.

1.2.2 Influencing Parameters in Vortex-Induced Vibration

The study of vortex-induced vibration (VIV) involves understanding important concepts in fluid mechanics, structural dynamics, materials, statistics, etc. VIV is encountered in many engineering applications, such as in the vibration of bridges, aircraft structures, offshore structures, etc. Because of its theoretical complexity and practical importance, VIV has been extensively studied over the past 50 years. Through experimental studies and numerical simulations, especially tests conducted on short rigid cylinders in laboratory conditions, much progress related to VIV has been made, such as in gaining an understanding of synchronization conditions, maximum motion amplitudes, response modes, vertex patterns, etc. Details related to these studies are discussed in comprehensive reviews by Blevins [8], Sarpkaya [45], [46], Bearman [5], Pantazopoulos [43], Khalak and Williamson [29], and Williamson and Govardhan [62], [63]. In lieu of restating the discussions presented in the cited studies, in this section, some influencing parameters often used to predict or examine the phenomenon of VIV, are briefly summarized.

Reynolds number, Re, (named after Osborne Reynolds, an English physicist) is a dimensionless number that measures the ratio of inertial forces to viscous forces for a given flow condition. Reynolds number is used to characterize whether a flow is laminar (typically when $Re < 2000$) or turbulent (typically when $Re > 4000$). The definition of Reynolds number is given by:

$$Re = \frac{UD\rho}{\mu} = \frac{UD}{\nu} \tag{1.1}$$

where U is the mean fluid velocity, D is the diameter of the cylinder's cross-section, ρ is the density of the fluid, μ is the dynamic viscosity of the fluid, and ν is the kinematic viscosity of the fluid (note that $\nu = \mu/\rho$).

Figure 1.2 depicts various wake patterns behind a cylinder in different Reynolds number regimes. The Reynolds number range, $300 < Re < 1.5 \times 10^5$, is referred to as the subcritical region; in this region, the cylinder boundary layer is laminar flow and vortex shedding is strong and periodic. The Reynolds number range, $1.5 \times 10^5 < Re < 3.5 \times 10^6$, is referred to as the transitional regime; in this regime, the cylinder boundary layer becomes turbulent and the vortex shedding becomes irregular. In the supercritical Reynolds number range, $Re > 3.5 \times 10^6$, the cylinder boundary layer is turbulent but the vortex shedding gains some regularity again [8]. Most engineering applications of VIV are associated with the upper subcritical and the transitional Reynolds number regimes [43].

Strouhal number, St, (named after Vincenc Strouhal, a Czech physicist) is a dimensionless number describing oscillating flow mechanisms and is defined as:

$$St = \frac{f_s D}{U} \tag{1.2}$$

where f_s is the vortex-shedding frequency (also referred to as the Strouhal frequency), D is the diameter of the cylinder, and U is the mean fluid velocity. The Strouhal number is a function of the Reynolds number. Over a wide range of Reynolds numbers (covering the subcritical and transitional regimes), vortex-induced vibration of cylinders generally occurs at $St \approx 0.2$. Given a constant St value, Eq. 1.2 suggests that the vortex-shedding frequency is proportional to the current speed and inversely proportional to the diameter of the cylinder.

Reduced velocity, V_r, is the ratio of the length of the stream path per cycle to the diameter of the cylinder:

$$V_r = \frac{U}{fD} \tag{1.3}$$

where U is the mean fluid velocity, f is the frequency of vibration, and D is the diameter of the cylinder. During lock-in conditions, the vortex shedding is trapped by the vibration of the cylinder, and the vortex-shedding frequency is synchronized with the frequency of vibration, i.e., $f_s = f$. Recall that, under lock-in conditions, $St \approx 0.2$; thus, $V_r = 1/St \approx 5$. Because of the interaction mechanism of VIV with the variation in added mass, however, the actual reduced velocity range for lock-in is much wider; usually we have $4 < V_r < 8$. The bounds of the reduced velocity range for lock-in depend on many factors; one of the most important of these is the mass ratio.

Mass ratio, m_r, is defined as the ratio of the mass of the cylinder per unit length to the mass of the displaced fluid. It is expressed as:

$$m_r = \frac{m}{\rho \pi D^2/4} \tag{1.4}$$

where m is the mass of the cylinder per unit length, ρ is the density of the fluid, and D is the diameter of the cylinder. The mass ratio is a measure of the susceptibility of a cylinder to vortex-induced vibration. The range of reduced velocity values over which synchronization occurs is primarily controlled by the mass ratio. A lower mass ratio indicates a wider synchronization range, while a larger mass ratio indicates a narrower synchronization range. This is because the effect of variation of the added mass is more important for low mass-ratio cylinders. The mass ratios of deepwater drilling risers are relatively low; usually, they are slightly above unity for steel risers, and may be even less than unity for composite risers.

Mass-damping parameter, $m_r\zeta$, is a combined parameter which is the product of the mass ratio, m_r, and the material damping factor, ζ. The mass-damping parameter can be related directly to several other parameters; these include:

$$\begin{aligned} &\text{Stability parameter:} \quad K_s = \pi^2 m_r \zeta \\ &\text{Scruton number:} \quad Sc = \frac{\pi}{2} m_r \zeta \\ &\text{Skop-Griffin parameter:} \quad S_G = 2\pi^3 St^2 m_r \zeta \end{aligned} \tag{1.5}$$

where St is the Strouhal number. Among these, the Skop-Griffin parameter might be the most widely used form that is related to the mass-damping parameter. Under lock-in conditions, the mass-damping parameter is thought to control the peak amplitude of VIV motion.

Added mass coefficient, C_a, is defined as the ratio of the (effective) added mass, m_a, to the mass of the displaced water, $\rho\pi D^2/4$, expressed as:

$$C_a = \frac{m_a}{\rho\pi D^2/4} \tag{1.6}$$

When a cylinder oscillates in a fluid, the movement of the cylinder causes the surrounding fluid particles to accelerate from their original positions. The force exerted by the accelerated fluid particles on the cylinder, which is in phase with the inertial force of the cylinder, contributes to the effective added mass force. The vortex shedding also results in a force in phase with the inertial force of the cylinder. The effective added mass force, consisting of these two components, is represented by the added mass, m_a, and the added mass coefficient, C_a. The added mass coefficient is not a constant. From forced-oscillation experiments, Sarpkaya [46] presented the variation of the added mass coefficient with reduced velocity for different values of the normalized vibration amplitude (see Fig. 1.3). The x-axis in the figure refers to the reduced velocity, the y-axis shows the added mass coefficient; the normalized vibration amplitude, A/D, is the ratio of the amplitude of the CF vibration to the diameter of the cylinder. Consider the curve for $A/D = 0.5$ to illustrate the variation of C_a with reduced velocity. The value of C_a rapidly decreases from about 5 to -0.7 when the value of V_r increases from 3 to 5.8; then, it increases very slightly to about -0.4 as the value of V_r increases further to 8.

The variation of C_a has a more dominant effect on a cylinder with a low mass ratio. The virtual mass, which is the sum of the mass of the cylinder and the added mass, may be expressed as:

$$m + m_a = (m_r + C_a)\,\frac{\rho\pi D^2}{4} \tag{1.7}$$

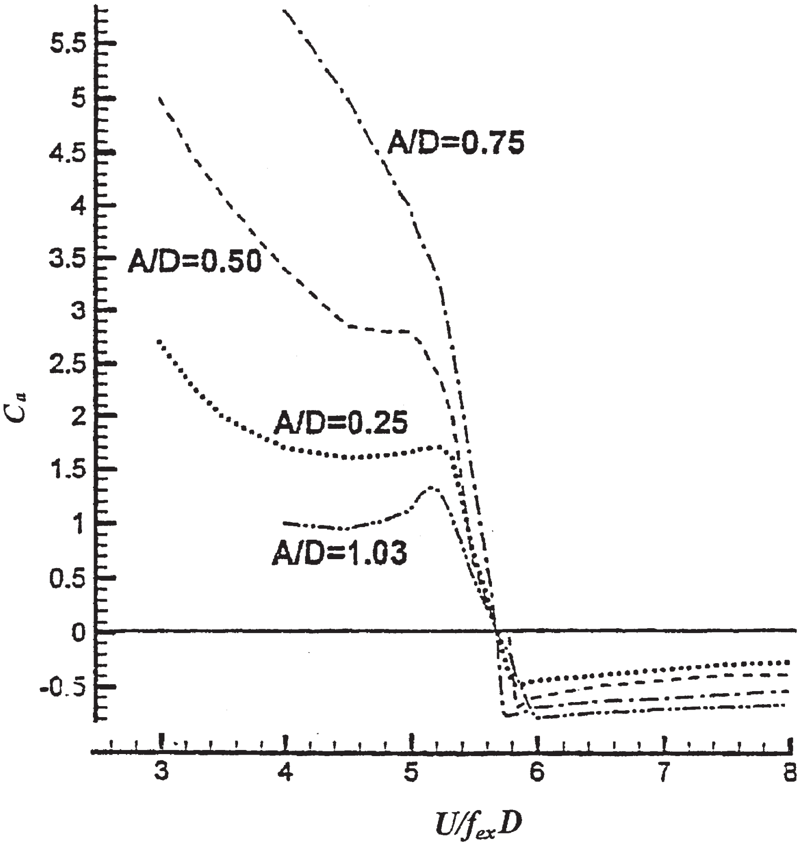

Figure 1.3: Variation of the added mass coefficient with reduced velocity for different values of the normalized vibration amplitude [46].

For a cylinder with a low mass ratio, under lock-in conditions, the virtual mass is much less than the mass of the cylinder itself; this explains why the actual VIV amplitude of a cylinder can be much larger than the amplitude that can be excited by a relatively small lift force exerted by vortex shedding.

The variation of C_a also helps explain possible wide synchronization ranges for VIV. With an increase in the reduced velocity, the added mass decreases, and the natural frequency of the cylinder increases; this causes synchronization to persist out to higher values of fluid speed [55].

1.3 Studies on VIV of risers

Vortex-induced vibration of short rigid cylinders is far less complex compared to VIV of long flexible cylinders (such as risers), where spatial effects along the cylinder's length cannot be ignored. Experimental studies on short rigid cylinders can help to reveal some basic physics about the VIV phenomenon and the interaction between the cylinder oscillation and the downstream wake. Experimental studies on VIV of long flexible cylinders serve to bridge the gap between the studies on short rigid cylinders and those on full-scale field risers.

1.3.1 Experimental Studies

Experimental studies on long flexible cylinders subjected to spatially varying current flows reveal the complexity of riser VIV. They provide measurements to update the database and to refine models used by semi-empirical software tools; they offer a benchmark for numerical simulations.

Over the past 30 years, researchers led by Prof. Vandiver at Massachusetts Institute of Technology (MIT) have carried out comprehensive experimental studies on VIV of long flexible cylinders.

In 1975 and 1976, the first Castine experiments were conducted in a tidal flow at Castine, Maine. The tested cylinders included synthetic fiber and wire cables, with a length of 22.9 meters, and diameters varying from 0.64 to 1.59 cm [57], [55].

The second Castine experiments were conducted in 1981 at the same site. Two types of cylinders were tested: a steel cable of 22.9 meters length and 3.18 cm diameter, and a steel pipe of 22.9 meters length and 4.14 cm diameter. The cylinders were subjected to uniform tidal current profiles with a maximum speed of about 0.7 m/s. The current speed, drag, tension, and biaxial accelerations at several locations along the cylinder length were measured. The main objective of these experiments was to study the response of long flexible cylinders subjected to VIV caused by uniform currents, and to assess the effects of the bending stiffness and mass ratio [27].

The Lawrence experiments were conducted in 1986 in Lawrence, Massachusetts. The length of the tested cylinder was 17.45 m and the diameter was 2.86 cm. Three current profiles with different shears were generated. The purpose of this test was to study the response characteristics of a long flexible cylinder in sheared flow [13].

Based on the two Castine experiments and the Lawrence experiments, but not limited to them, Vandiver [55] evaluated conditions favorable to large-amplitude VIV of long flexible cylinders subjected to uniform and sheared current flows. Some dimensionless parameters, which are important for predicting the VIV response of long flexible cylinders, were also studied [55].

The experiments conducted in the 1970's and 1980's have some limitations in that: (i) the VIV response excited was confined to lower modes of vibration; (ii) the response was measured at only a very small number of locations along the cylinder span; and (iii) the incoming current was difficult to control.

As oil exploration moves into deeper waters, marine risers become longer and more susceptible to vibration at higher mode numbers (such as in the 10th mode and higher) when subjected to ocean currents. In order to mitigate flow-induced vibrations, vibration suppression devices, such as strakes and fairings, are often installed on risers. Thus, understanding the dynamics of VIV of long cylinders, especially high-mode number VIV, is extremely important. In addition, the effectiveness of vibration suppression devices and their side effects, e.g., in increasing drag on these long cylinders, also needs to be studied.

In order to gain knowledge of VIV on very long cylinders, both bare and suppressed, the research group led by Prof. Vandiver at MIT conducted a series of experiments including the Lake Seneca experiments in 2004 and two Miami Gulf Stream experiments in 2004 and 2006, respectively.

The Lake Seneca experiment was conducted at the Naval Acoustic Test Facility at Lake Seneca, New York in 2004. During the experiments, a fiberglass pipe was towed by a boat with a railroad wheel attached at the bottom end of the pipe. The tested pipes were of a diameter of 3.33 cm and two different lengths, 61.26 m and 122.23 m. The pipes were positioned in calm water and were exposed to uniform currents when towed by the boat. The towing speed varied roughly from 0.3 to 1.1 m/s. The response was measured by twelve evenly spaced triaxial accelerometers for the 61.26 m long pipe and twenty-four evenly spaced triaxial accelerometers for the 122.23 m long pipe. The length, diameter, and tension of the pipes were carefully selected to permit cross-flow response up to the 25th mode. In addition to bare pipes, pipes with a triple helical strake were also tested in the Lake Seneca experiment [49].

The two Gulf Stream experiments were conducted in the Gulf Stream off the coast of Miami in 2004 and 2006. During the experiments, a fiberglass pipe was hung onto and towed by the Research Vessel F.G. Walton Smith owned by the University of Miami. A railroad wheel was attached at the bottom of the pipe to provide tension. Steering the vessel heading in different directions relative to the direction of the ocean current exposed the towed pipe to a variety of current profiles with different speeds and spatial profiles. Two fiber optic strain gauges were embedded in each quadrant of the pipe during manufacture, which allowed strains in each quadrant of the pipe to be measured at 70 locations, spaced seven feet apart. The current speed along the length of the pipe was recorded by two Acoustic Doppler Current Profilers (ADCPs) equipped on the Research Vessel F.G. Walton Smith. The pipe tested in the first Gulf Stream experiment was 147.92 m long with a diameter of 3.56 cm; and the pipe tested in the second Gulf Stream experiment was 153.77 m long with a diameter of 3.58 cm. In addition to bare pipes, pipes of helical strakes or fairings with different spatial coverage, were also tested. The length, diameter, and tension of the pipes were carefully selected to make high mode-number VIV possible [49].

Some interesting response characteristics were observed from these field experiments, and these led to a variety of studies on the VIV response of long cylinders. For high mode-number VIV of bare pipes, pure standing waves were seldom observed; instead, traveling waves often dominated the cylinder responses [37]. The power-in region, where energy is transferred from the fluid to the cylinder and vibrations are originated, was identified [50], [49]. Strong higher harmonics (responses at integer multiples of the fundamental vortex-shedding frequency, also called Strouhal frequency) were also often observed. In some test runs, higher harmonics accounted for a large portion of the total root-mean-square (RMS) value of the strains. The fatigue damage rate calculated based on the measured strains containing higher harmonic components was up to forty times larger than the fatigue damage rate if only responses around the Strouhal frequency were considered [58]. Most analytical software, such as VIVA [53], VIVANA [32], and SHEAR7 [56], do not have the ability (based on the author's knowledge and, at least, at the date of this writing) to directly account for higher harmonics in the predicted response of cylinders and the resulting fatigue damage rate. The predicted fatigue damage rate needs to be corrected, such as by multiplicative factors, to take into account the effects of higher harmonics [25], [26]. In addition to studying VIV of bare pipes, the effects of strakes in the suppression of high mode-number VIV of long pipes were also studied [59], [60].

In addition to the experiments conducted by researchers at MIT, experiments using long flexible cylinders were also conducted by other researchers. In 1997, the Hanøytangen experiments were performed in a Norwegian fjord at Hanøytangen, on the west coast of Norway [23], [33]. The test cylinder was a 90 m long stainless steel pipe, with an outer diameter of 30 mm. The pipe was excited by a simulated linearly sheared current. Biaxial strains (CF and IL) were measured at 29 locations, evenly spaced 3 m apart, along the length of the pipe. Based on the discrete measurements, the CF and IL responses along the entire length of the pipe was reconstructed [33]. Note that the reconstruction technique employed generally only took into consideration the response around the Strouhal frequency for the CF direction, and at two times the Strouhal frequency for the IL direction, since higher harmonic components were pre-filtered out before the reconstruction. In addition, the fatigue damage rates caused by the CF and IL vibrations were calculated at the discrete locations, and compared with the predictions using an analytical program [3].

Experiments of vortex-induced vibration using a long flexible cylinder were also conducted in well-controlled laboratory conditions. In 2003, ExxonMobil performed VIV testing on a long flexible cylinder at the Norwegian Marine Technology Research Institute (Marintek). The tested cylinder was 9.63 m long with a diameter of 20 mm. Uniform and linearly sheared current profiles were simulated. Bending strains and accelerations in the CF and IL directions were measured. Some characteristics of the VIV response, such as identification of excited modes as well as understanding the relationship between frequency, amplitude and the current speed, were all studied. The fatigue damage rate based on the CF response and the IL response were compared. In addition, the effectiveness of strakes in suppressing VIV was also investigated [19], [51].

In 2003, the Norwegian Deepwater Programme (NDP) high-mode VIV experiment was carried out at Marintek, by horizontally towing a flexible cylinder (model riser) in the Ocean Basin test facility. The cylinder was made of fiberglass with a length of 38 meters and an outer diameter of 27 mm. Uniform and linearly sheared current profiles were simulated. Axial strains and transverse accelerations in the CF and IL directions were measured at discrete locations. The tests were conducted both on a bare riser and two straked risers with different strake geometries and spatial coverages. The objectives of the model test program were: (i) to improve the understanding of high-mode VIV response of flexible risers and associated fatigue damages; and (ii) to assess the effectiveness of the strakes in VIV mitigation [10]. Trim et al. [54] applied a modal analysis approach to evaluate the NDP data and compared response characteristics such as excited modes and frequencies, maximum amplitudes, and fatigue damage rates of the bare cylinder and the straked cylinder.

The studies documented in this dissertation are based on the NDP data because the NDP experiments were carefully designed, well conducted, and densely instrumented. Furthermore, part of the NDP data set is also publicly available at the VIV data repository [11]. More details on the NDP experiments that relate to the test setup and other physical properties of the model riser may be found in Appendix A, as well as in other studies [10], [54].

In addition to the reduced-scale experiments using model risers, measurements of full-scale marine risers were also conducted as part of a riser monitoring campaign [7], [52]. These measurements confirmed some characteristics of the VIV response also observed in reduced-scale long flexible cylinder experiments, such as the presence of non-stationary characteristics, higher harmonics, and traveling waves [7]. Furthermore, it was found that the selected semi-empirical software underpredicts the fatigue damage rate caused by VIV [52].

1.3.2 Semi-Empirical VIV Response Computational Tools

Based on experimental studies (using short rigid cylinders and long flexible cylinders) and theoretical studies, semi-empirical computer programs, such as SHEAR7 [56], VIVA [53] and VIVANA [32], were developed for predicting the VIV response of marine risers. A key assumption that these semi-empirical programs rely on is that of the validity of the strip theory—namely, that the hydrodynamic coefficients (lift, drag, damping, added mass, etc.) depend only on the local vibration and flow conditions. Thus, a long flexible cylinder is subdivided into short sections and each of them is modeled as an elastically mounted rigid cylinder. The hydrodynamic forces exerted on each section (short rigid cylinder) are estimated using an empirical database obtained from simplified experiments; the total forces over the entire cylinder span are obtained by integrating the local spatial forces. By applying the forces onto a finite element model of the long flexible cylinder, the response of the cylinder is predicted. Note that, because of the feedback mechanism of VIV, a number of iterations are needed before final convergence and an energy-balanced state can be reached.

Given detailed riser physical properties and current profile informaton, semi-empirical programs are often used to predict riser VIV response. However, their intrinsic limitations introduce errors in these predictions. First, the strip theory assumption neglects the flow and vortex shedding along the riser axis by simplifying the 3-dimensional fluid-structure problem as a 2-dimensional problem. Second, the databases employed by the software were mainly obtained from simplified laboratory experiments, with limited Reynolds number and where cylinder motion was restricted to the cross-flow direction. In order to improve the semi-empirical programs, several studies have been conducted. Dahl [14] obtained a database of force coefficients by conducting forced-oscillation experiments using short rigid cylinders where both cross-flow and in-line motions were allowed. Jhingran [25] extracted spatially averaged drag force coefficients for long flexible cylinders experiencing high mode-number VIV. Mukundan [41] optimized lift force coefficient by minimizing the error between the predictions and the measurements of the VIV response of a long flexible cylinder. The programs are continuously improved; still, only the cross-flow response at the Strouhal frequency (vortex-shedding frequency) can be predicted. Experiments show that predictions excluding higher harmonics (i.e., the response at frequencies that are multiples of the Strouhal frequency) can underestimate the fatigue damage rate by a factor exceeding twenty [26].

1.3.3 Numerical Simulation

Numerical simulation using computational fluid dynamics (CFD) is an alternative approach widely used to assess the VIV response of cylinders. Dixon and Charlesworth [16] discussed several key CFD modeling issues, including the selection of turbulence models, grids, time steps, etc. With rapid progress in computational techniques and capabilities, CFD offers the potential capability to accurately predict the VIV response of deepwater marine risers. Josefsson and Dalton [28] analyzed a top-tensioned riser with a length to diameter (L/D) ratio of 5,380, by employing the strip theory assumption. The riser was divided into a number of segments; in the planes at the ends of each segment, the flow was treated as a 2D flow; and the forces at each plane were obtained by solving the 2D Navier-Stokes equation. Huang et al. [22] analyzed a 10 m long riser with a L/D ratio of 482. Instead of relying on the strip theory assumption, the flow field around the riser was calculated by solving the 3D Navier-Stokes equation; the mesh along the riser's spanwise direction was much coarser than that on the riser cross-section planes. Despite dramatic progress in the application of CFD for VIV analysis of risers, the fully three-dimensional numerical simulation of VIV for deepwater risers in realistic Reynolds number regimes is still prohibitive due to the overwhelming complexity and the intensive computational requirements.

1.4 Research Objectives

Response measurements on long flexible cylinders, either from reduced-scale experiments or from full-scale riser monitoring campaigns, have great importance in the study of VIV and associated fatigue in risers. The measurements guide the development and improvement of semi-empirical programs and numerical simulations in several ways: (i) response characteristics observed in the measurements provide directions for refinement of predictive software; (ii) the data extracted from the measurements can be used to update the predictive software; and (iii) the measurements can be used to benchmark and validate the prediction software. Thus, response measurements, especially on long flexible cylinders, have a central role in the study of riser VIV.

The overall objective of this study is to develop a method for empirical prediction of long-term fatigue damage rates and life of risers solely based on measured data. Specifically, the research objective are three:

(i) *To assess the complex characteristics of VIV response in long flexible cylinders.* Experiments conducted on short rigid cylinders have uncovered the complex nonlinear interaction mechanism between the structure and the wake. Experiments using long flexible cylinders, including field measurements on real marine risers, reveal the presence of even more complex characteristics such as the non-stationary behavior, a combination of traveling waves and standing waves, and higher harmonics. Assessment and visualization of these complex phenomena can help to better understand and analyze riser VIV response and its effects such as in fatigue damage. This study shows that numerical techniques, such as spectral analysis, the use of Hilbert transforms, wavelet analysis, etc., are useful tools for this purpose. By applying these techniques in analyses of data, we show that these complex response characteristics are not generally transient and negligible; instead, they can be persistent and associated with a large portion of energy, and should be considered in the prediction or reconstruction of the VIV response over the entire riser span.

(ii) *To reconstruct the VIV response over the entire span of a cylinder using different empirical methods with measurements at a limited number of locations.* During experiments or full-scale riser monitoring campaigns, VIV response is often measured in the form of bending strains and/or lateral accelerations taken at a limited number of locations where sensors are installed. If, at the point of interest, such as the location of a critical fatigue detail, a sensor were installed, fatigue damage can be estimated directly from the measurements at that location. However, it is impossible to install a sensor at every location of interest because deepwater risers can be very long and costs for sensor deployment are high. Thus, it is desirable to reconstruct the riser response over its entire span from a limited number of measurements. In this study, five different empirical methods are employed for this purpose. Some empirical methods have the ability to directly account for the complex characteristics of the VIV response in the riser response reconstruction. Fatigue damage rates are estimated based on the reconstruction and compared with the similar estimates based on direct measurements at discrete locations (this is possible if such checks are selectively performed at the locations of sensors not used in the empirical reconstruction, but where measurements are available—we refer to this as cross-validation). Results show that all the empirical methods presented, despite different underlying assumptions in each of them, may be employed to estimate fatigue damage rates quite well from limited strain measurements. In addition, the influence of the spatial arrangement of sensors on the quality of fatigue estimation is studied.

(iii) *To predict the long-term fatigue damage rate and life of instrumented risers by utilizing empirical methods, response measurements, and metocean data.* It is becoming increasingly common to instrument marine risers as part of long-term monitoring campaigns during which response measurements, such as strains and/or accelerations, at a limited number of locations are recorded. This is especially useful during operation. Simultaneously, current profiles at a nearby location are also often recorded. Such data are all that is needed for long-term empirical fatigue damage prediction. Short-term fatigue damage rates caused by each distinct current type may be estimated using various empirical methods supported by the discrete response measurements. The long-term fatigue damage rate probability distribution is then estimated by combining/multiplying the short-term fatigue damage rate probability distribution (conditional on current type) with the relative likelihood of each current type (based on metocean studies), and integrating over current types. We note that the empirical approaches presented rely only on measured strain and/or acceleration data; the data explicitly account for the different response characteristics and for the different current profiles experienced by the riser. In addition, estimates of fatigue damage and life for any location of interest are easily updated as more data become available from any ongoing field monitoring.

Studies that address the objectives mentioned above were conducted by utilizing measurements from a long flexible cylinder that were part of the Norwegian Deepwater Programme (NDP) experiments. The cylinder resembles real drilling risers with a length to diameter (L/D) ratio of 1,400 and a mass ratio of 1.6. The cylinder was densely instrumented and experienced high mode-number VIV when excited by uniform and sheared currents. Additional details related to the NDP experiments can be found in Appendix A and in other studies [10], [54].

1.5 Organization of the Dissertation

This dissertation is organized as six chapters. In this first chapter, the phenomena of vortex shedding and vortex-induced vibration (VIV) of cylinders, including some important parameters related to VIV have been briefly described. The different approaches used in studies of riser VIV have also been discussed. The research objectives of this study have been outlined. The content of the remaining chapters is described next.

Chapter 2 describes studies of complex VIV response features of the selected model riser, including non-stationary characteristics, traveling wave patterns, and higher harmonics. Several useful tools, such as the Hilbert transform and the wavelet transform, are adopted to assess and visualize the complexity of riser response.

Chapter 3 presents details of the empirical methods used for riser response reconstruction given data. Five empirical methods are studied and the underlying assumptions, equations, applications, results, advantages, and disadvantages are discussed. The influence of alternative spatial arrangements of sensors on fatigue damage estimation is also studied.

Chapter 4 describes a data-driven mode identification algorithm—i.e., the dominant riser VIV mode is empirically identified through a spatial spectral analysis of the data. This is an improvement on one of the empirical methods used for response reconstruction.

Chapter 5 demonstrates the methodology of empirical long-term prediction of fatigue damage rates and life for an instrumented marine riser. Sensitivity studies related to the number of available sensors and the number of data sets are conducted.

Chapter 6 is a summary of the main results presented in this dissertation. Suggestions for future work are also discussed in this chapter.

Chapter 2

Characteristics of VIV Response of Long Flexible Marine Risers

2.1 Introduction

Vortex-induced vibration is of great interest in the context of fatigue design of marine risers as oil and gas production moves into deeper waters. Model tests provide valuable insight into the VIV phenomenon and associated riser response characteristics. Experiments, especially on long flexible cylinders, which better resemble real deepwater marine risers, help to study complex response features in a more realistic manner than can those conducted on short rigid cylinders under similar current/flow conditions [12].

In this study, measurements (strains and accelerations) available from the Norwegian Deepwater Programme (NDP) experiments on an instrumented model riser are employed to examine characteristics of the VIV response of a long flexible cylinder (the model riser) placed in uniform as well as sheared currents.

The riser dynamic response measured at discrete locations is stored as a suite of time series. The energy distribution by frequency of the response is uncovered by carrying out a spectral analysis on each time series, assuming stationarity of the response process. As we shall see, power spectral density (PSD) plots based on the acceleration or strain measurements provide evidence of strong higher harmonics (i.e., dominant response energy at frequencies that are multiplies of the Strouhal frequency); in the data sets analyzed, sometimes the third harmonic (i.e., response at a frequency that is 3 times that of the Strouhal frequency) is seen to possess a large portion of the total energy. The frequencies of each spectral peak (harmonic) can be identified from the PSD plots. Generally, a strong linear relationship between the (response) spectral peak frequency and the maximum current speed is evident; the proportionality constant between this spectral peak frequency and the current speed is estimated using linear least squares fitting. Such analyses of the model test data can be useful in estimating parameters such as the Strouhal number for these long flexible cylinders undergoing VIV.

The instantaneous amplitudes of the CF and IL displacements as well as the phase difference between these displacements (estimated from the phase angles associated with the motion orbits) can be estimated from their analytic signals obtained using Hilbert transforms. The widely varying spatial patterns of the displacement amplitudes and phase angles (motion orbits) over the riser length confirm that the motion of a long flexible cylinder is far more complex than that of a rigid cylinder; similarly, the temporal variation in riser response, even within a single recorded event where the current velocity profile is unchanged, serves to illustrate non-stationary behavior which is generally more pronounced for uniform current profiles than for sheared currents.

Wavelet transforms provide a useful time-frequency representation of the complex VIV response characteristics of risers. Using continuous wavelet transforms, the energy content in a signal in the time and frequency domains can be represented using scalograms which, describe time, scale (related to frequency), and wavelet transform coefficient value (where the latter is often squared and shown by varying intensity or color). In this study, scalograms of the measured NDP model riser CF accelerations reveal that (i) higher harmonics are commonly observed when the riser is subjected either to uniform or sheared currents; and (ii) the energy distribution among the first and higher harmonics can vary considerably even within one record, especially for uniform current profiles.

Besides non-stationary characteristics and the presence of higher harmonics in the response, the presence of traveling waves along the NDP bare model riser, when subjected either to uniform or sheared currents, is evident in the data. It is expected that the consideration of these complex response characteristics is necessary in studies of riser VIV response and associated fatigue damage analysis.

2.2 Higher Harmonics and Linear Relationship between Harmonic Frequencies and Maximum Current Speed

Spectral analysis is commonly used to study the energy distribution by frequency of time series, such as those of the model riser's measured acceleration or strain signals. A power spectral density (PSD) plot, obtained using Welch's method, of accelerations measured at eight locations for a uniform current data set, NDP2120, is presented in Fig. 2.1. The figure at the top depicts the PSDs of the CF accelerations; the figure at the bottom depicts the PSDs of the IL accelerations. Each ribbon represents an acceleration time series measured by a single sensor (the location of each sensor is indicated in

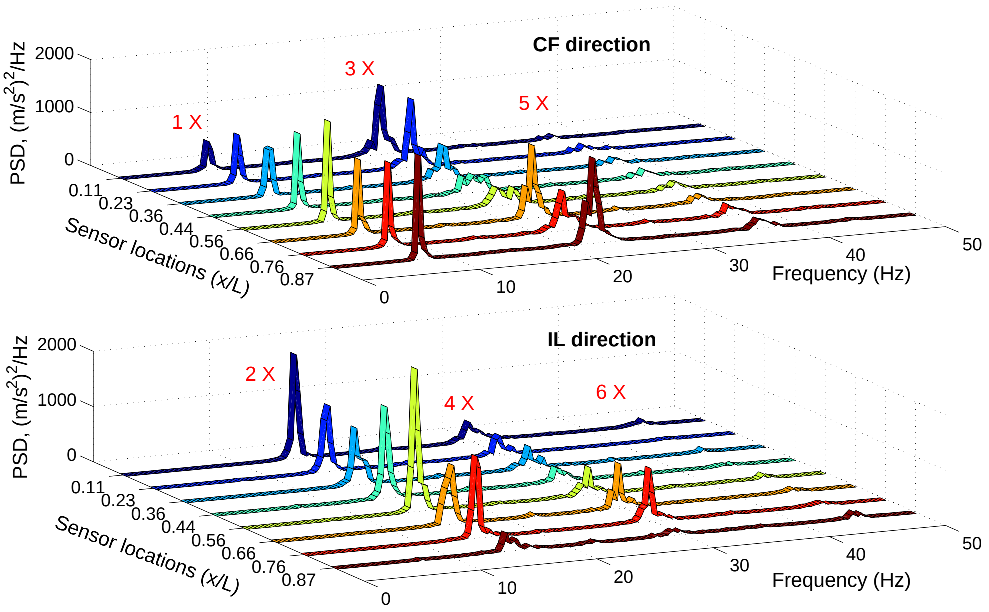

Figure 2.1: Power spectral density (PSD) plot of accelerations in the cross-flow and inline directions for the NDP2120 (uniform current) data set.

the figure). As illustrated in Fig. 2.1, the eight acceleration power spectra indicate very similar frequency content. All these spectra show the presence of the 1st, 3rd, and 5th harmonics in the CF accelerations; and the presence of the 2nd, 4th, and 6th harmonics in the IL accelerations. Note that the 3rd harmonic in the CF acceleration spectra is quite strong and, at some locations, it is even stronger than the 1st harmonic.

Higher harmonics are often observed in the acceleration or strain signals measured on long flexible cylinders, and their consideration is of interest in recent studies related to riser VIV. For instance, the Lake Seneca experiment and the Gulf Stream experiment, conducted by researchers led by Prof. Vandiver of MIT, showed the presence of higher harmonics in the strain signals measured on a long flexible cylinder experiencing uniform or sheared currents [37].

Higher harmonics have also been observed in measurements from full-scale drilling risers [7], [52].

The features and causes of higher harmonics in riser VIV response have been studied by many researchers. Mukundan [41] separated each harmonic of the CF strain signals obtained from the NDP experiments by using band-pass filters and plotted Lissajous curves using the first and third harmonics, and the first and fifth harmonics separately. A Lissajous curve is a graph often used to depict the frequency ratio and phase difference between two harmonic signals. By visual inspection of the Lissajous curves, Mukundan [41] found that the frequency ratio between the third and first harmonic, and that between the fifth and first harmonic were integers and remained constant. He stated that this condition indicated that the third and fifth harmonics were phase-locked on the first harmonic.

Jauvtis and Williamson [24] carried out VIV experiments using spring-mounted rigid cylinders that were of low mass ratios (< 6) and were free to vibrate in both the CF and IL directions. They found that the third harmonic component in the lift force is caused by a “2T” periodic vortex wake pattern, where three vortices are shed in each half-cycle. Dahl [14] observed that a significant third-harmonic lift force can exist either in the case of a “2T” vortex pattern or in the case where the cylinder moves according to a “2P” vortex pattern (where two pairs of vortices are formed in each cycle).

At the present time, some semi-empirical computer programs, such as SHEAR7 [56] and VIVA [53], assume only the presence of the first harmonic in any riser VIV response. Studies conducted by Jhingran [52], and Jhingran and Vandiver [26] have shown that fatigue damage rates, calculated based only on the first harmonic and neglecting the contributions of higher harmonics, can be underestimated by a factor exceeding twenty. Hence, Jhingran and Vandiver [26] and Modarres-Sadeghi et al. [40] proposed different methods to correct predictions of fatigue damage for higher-harmonic effects. In both their approaches, the basic idea is to make corrections related to estimates from available data of the ratio of the stress or lift contribution from the higher harmonics to that from the first harmonic and, thus, account for the contributions of higher harmonics. These methods are purely empirical and the "correction factors" are estimated from limited measurements.

Higher harmonics were commonly observed for bare risers subjected to both uniform currents and linearly sheared currents in the NDP experiments. As depicted in Fig. 2.1, the spectral peak frequencies for accelerations measured at the different locations along the riser are almost same. Their mean values (averaged over all locations) were calculated for each data set and plotted against current speed in Figs. 2.2(a) and 2.2(b), respectively, for the uniform current data sets and the sheared current data sets ((in the case of the sheared current data, the plots used the maximum current speed). The 1st, 3rd, and 5th harmonic peak frequencies were identified from the CF accelerations and plotted in blue; similarly, the 2nd, 4th, and 6th harmonic peak frequencies were identified from the IL accelerations and plotted in red. Note that, in some cases, the highest harmonics could not be clearly identified; hence, for some current speeds, points are missing from Figs. 2.2(a) and 2.2(b) for those harmonics.

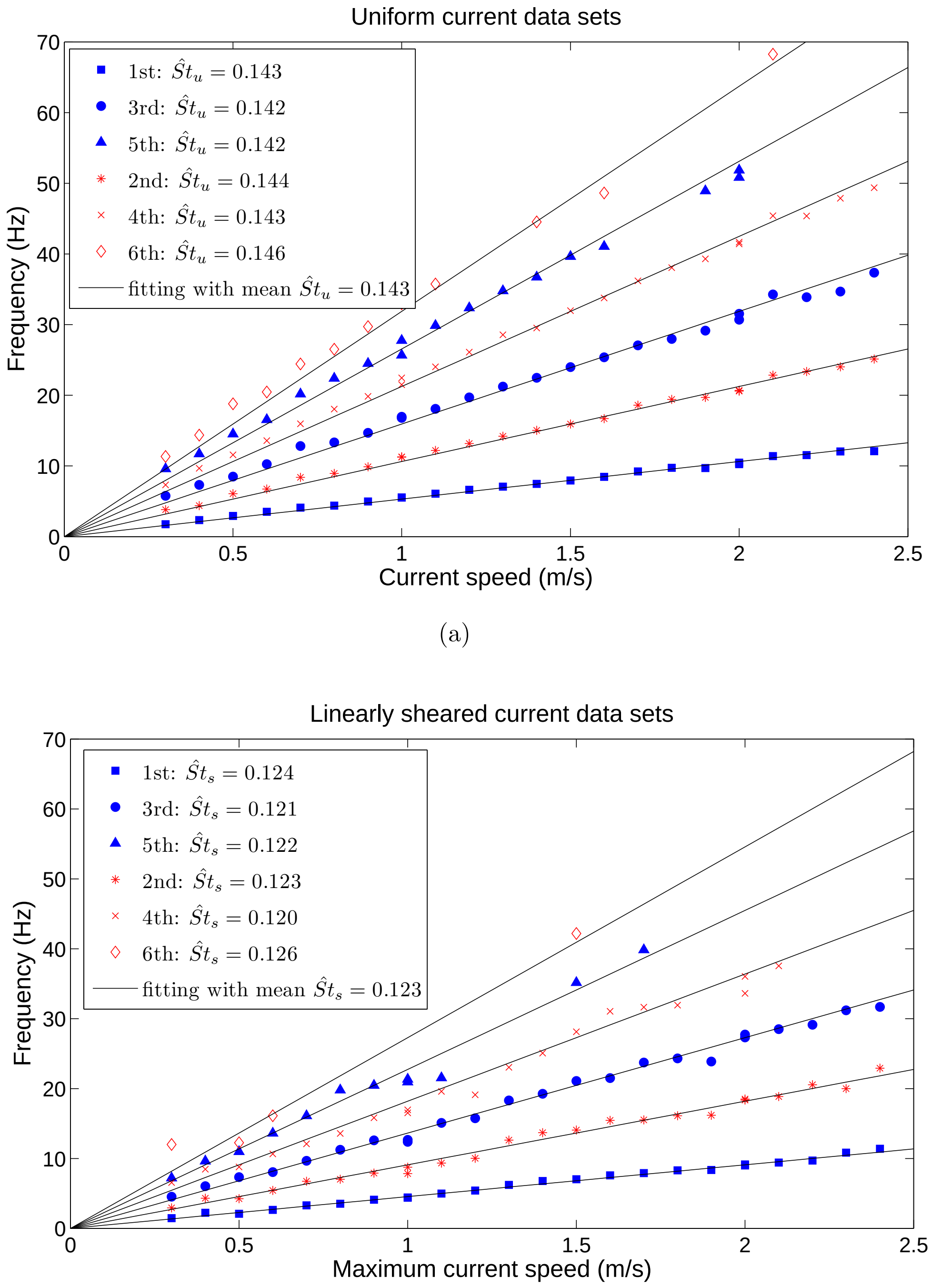

(a)

(b)

Figure 2.2: Linear relationships estimated between the riser response peak frequency (harmonic) and the maximum current speed: (a) uniform current data sets; and (b) linearly sheared current data sets.

Figures 2.2(a) and 2.2(b) show fairly strong linear trends in plots of the cylinder's peak spectral frequencies and the (maximum) current speed. Under lock-in conditions, the vortex shedding is synchronized with the cylinder's oscillation; thus, the vortex-shedding frequency and the cylinder's oscillation frequency are the same. The vortex-shedding frequency, f, is linearly proportional to the current speed, U, because $f = St\,U/D$, where D is the cylinder diameter and St is the Strouhal number. The Strouhal number of a stationary circular cylinder is about 0.2 for large Reynolds numbers, including the upper subcritical regime and the transitional regime. In the following, the Strouhal number for a long flexible cylinder of circular cross-section with Reynolds number up to 7×10^4 is estimated assuming a linear relationship between the peak spectral frequency and the maximum current speed based on the NDP experiments. Assume that the n^{th} harmonic frequency equals n times the vortex-shedding frequency, we have:

$$\hat{St} = \frac{nfD}{U} \tag{2.1}$$

where $\hat{St}$ is the estimated Strouhal number for the long flexible NDP model riser with $D = 0.027$ mm, and U is the maximum current speed. In Figs. 2.2(a) and 2.2(b), the Strouhal number estimates based on least squares fits are presented. For example, the Strouhal number estimated from the uniform current data sets, denoted as $\hat{St}_u$, is 0.143 based on the 1^{th} harmonic peak frequencies; similarly, $\hat{St}_u = 0.144$ based on the 2^{nd} harmonic peak frequencies. The estimates based on all six frequencies are very similar with a mean value of 0.143. The solid lines in Fig. 2.2(a) are based on the estimated mean value of 0.143 for $\hat{St}_u$.

Similarly, for the sheared current data sets, depicted in Fig. 2.2(b), the six Strouhal number estimates, $\hat{S}t_s$, are also very close and the mean value based on all six frequencies is 0.123. For these linearly sheared current profiles, the maximum current occurs at one end of the cylinder where it cannot oscillate. The "effective" current speed that brings about the VIV response occurs at a location some distance away from the cylinder end and is smaller than the "nominal" maximum current in the test. This is why $\hat{S}t_s$ is found to be smaller than $\hat{S}t_u$. Other researchers such as Tognarelli et al. [51] and Lie and Kaasen [33] also showed that the Strouhal number for long flexible circular cylinders is smaller than the value of 0.2 which was estimated from experiments using stationary circular cylinders.

2.3 Non-Stationary Characteristics: Variation Amplitude and Phase in Displacement Orbits

The VIV response of short rigid cylinders in laboratory conditions is periodic and stable if the incoming current does not vary with time. On the other hand, the VIV response of long flexible cylinders is more complex and can exhibit strong non-stationary characteristics if even the current remains unchanged. For the NDP experiments, CF and IL accelerations were measured at eight locations along the length of the riser. Displacements were obtained by double integration of the acceleration signals and minimizing low-frequency noise by the use of high-pass filters. The temporal evolution and spatial variation of discrete displacement orbits (at sensors) observed for the NDP2120 (uniform current) data set and the NDP2350 (sheared current) data set, are plotted in Figs. 2.3 and 2.4, respectively. In the figures, each row depicts the temporal evolution of the displacement orbit measured at a single spatial location; each column depicts the spatial variation of the displacement orbits over a short time interval beginning at the time instant indicated. For example, the top row is associated with the location, $x/L = 0.11$, close to the higher current end for the sheared current cases; likewise, the first column is associated with a short time interval that begins at 0 seconds. To avoid plotting displacement orbits that overlap each other making it difficult to study individual orbital patterns, only eight full cycles of vibration are presented. For data set NDP2120, displacement orbits at two-second intervals from 0 to 14 seconds are shown. Over a single two-second interval, about 15 cycles of vibration actually occur but only one of them is plotted. The duration of 14 seconds is about one-half of the total duration of the NDP2120 record. Similarly, for data set NDP2350, displacement orbits at four-second intervals from 0 to 28 seconds are shown. Over a single four-second interval, about 15 cycles of vibration occur but, again, only one of them is plotted. The duration of 28 seconds is about one-half of the total duration of the NDP2350 record. In each displacement orbit, the IL direction is horizontal and the CF direction is vertical. All displacement orbits in each figure are plotted to the same scale; a vertical bar of a length, $2D$, is shown in the figure for reference (D is the cylinder diameter). The direction of the motion in time of the oscillations at each sensor is indicated using three dots—the motion starts at the largest dot, then proceeds to the smaller ones. The current flows from right to left as is indicated in the figures.

The displacement orbits can be broadly classified into three types: (i) the orbit assumes a figure-eight shape and the IL motion is upstream (i.e., from left to right) at the outermost CF positions; this is termed counter-clockwise figure-eight motion and is colored red; (ii) the orbit assumes a figure-eight shape, but the IL motion is downstream (i.e., from right to left) at the outermost CF positions; this is termed clockwise figure-eight motion and is colored blue; and (iii) the orbit does not assume a figure-eight shape, and is colored green.

First, let us study Fig. 2.3. At a single location (i.e., along any single row), the shape and amplitude of the displacement orbits show some variation with time; this reveals non-stationary characteristics of the VIV displacement response. At a single time instant (i.e., along any column), the shape and amplitude of the displacement orbits show some variation with position along the riser; this suggests that the deformed shape of the riser is complex. Note that the largest peak-to-peak amplitude of the CF displacement is about $2D$, which occurs at the location, $x/L = 0.36$ for the 8-second trace.

As distinct from the uniform current data set NDP2120 shown in Fig. 2.3, the displacement orbits for the sheared current data set, NDP2350, in Fig. 2.4, have shapes and amplitudes that remain relatively stable with time; this suggests fairly stationary behavior of the VIV response in this case. The displacement orbital shapes, however, exhibit some variation in space (i.e., at the different locations); this suggests that the deformed shape of the riser is quite complex. The peak-to-peak CF amplitudes are smaller than those observed with the uniform current data set, NDP2120 (the smaller maximum current speed of 0.7 m/s for NDP2350 versus the uniform current speed of 1.4 m/s for NDP2120 might be the main reason for the smaller vibration amplitude).

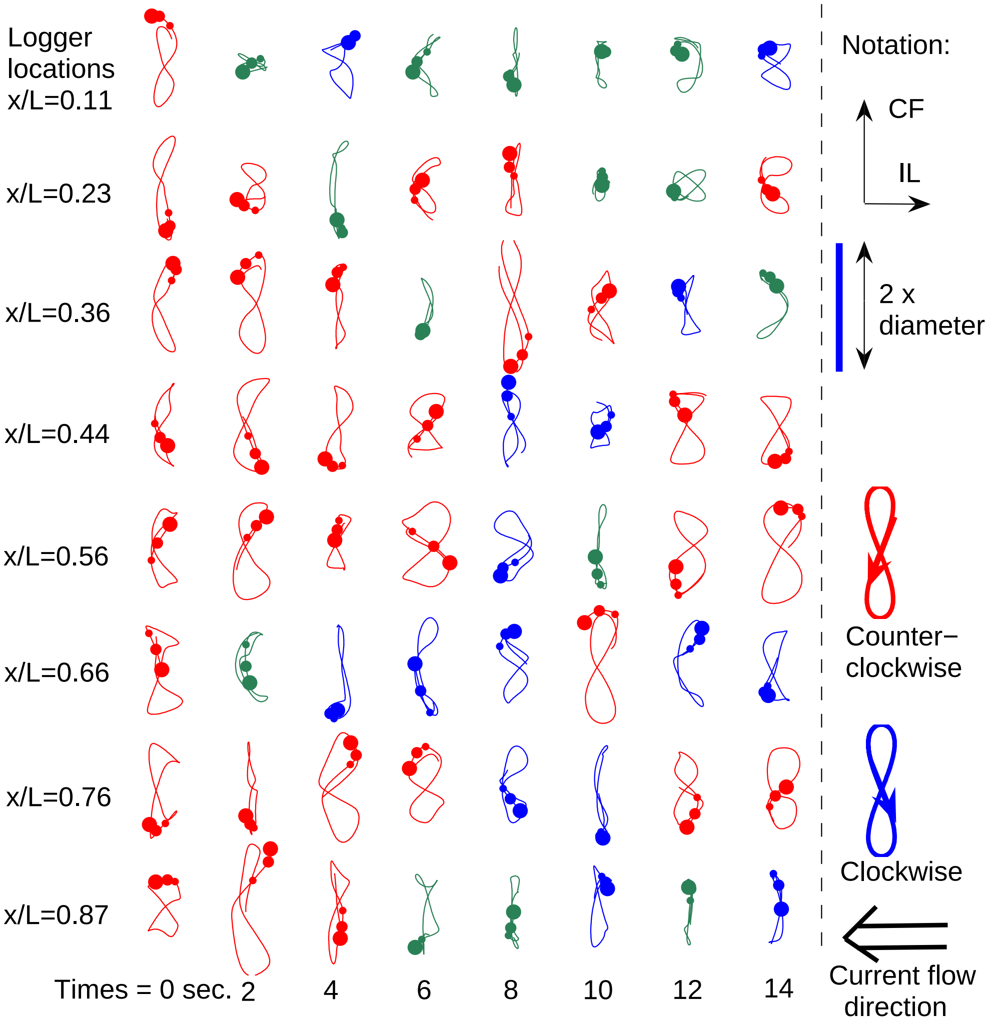

Figure 2.3: Displacement orbits at sensor locations over short time intervals for the NDP2120 (uniform current) data set.

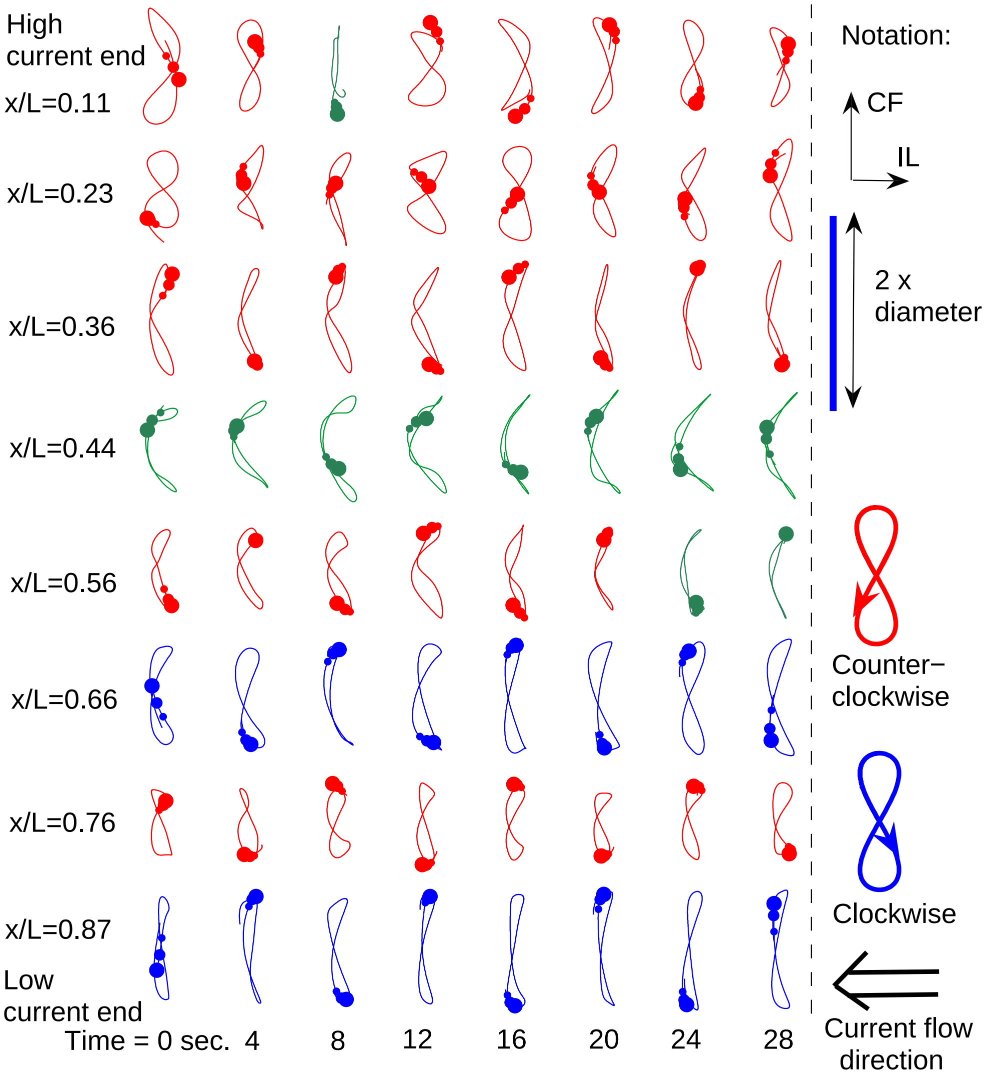

Figure 2.4: Displacement orbits at sensor locations over short time intervals for the NDP2350 (sheared current) data set.

Plots of the evolution of displacement orbits provide a qualitative description of the non-stationary characteristics of cylinder VIV response. A quantitative description of the variation of displacement amplitude and phase of orbit with respect to time may be obtained with the help of Hilbert transforms.

Although higher harmonics are commonly observed in the strain and acceleration response of a riser experiencing VIV, their contribution to the displacement response is somewhat diminished. Let us assume that the IL displacement, $x(t)$, and the CF displacement, $y(t)$, may be expressed as single-frequency trigonometric functions, such that:

$$x(t) = A_x(t) sin[\omega_x(t) \cdot t + \theta(t)]; \quad y(t) = A_y(t) sin[\omega_y(t) \cdot t] \tag{2.2}$$

where $A_x(t)$ and $A_y(t)$ are the instantaneous IL and CF displacement amplitudes, respectively; similarly, $\omega_x(t)$ and $\omega_y(t)$ are the instantaneous IL and CF displacement angular frequencies, respectively. The angle, $\theta(t)$, which separates in phase the IL displacement from the CF displacement, is of particular interest because different values of $\theta(t)$ are associated with different shapes of the riser displacement orbits [24]. To illustrate this, a schematic diagram showing displacement orbits for various values of $\theta(t)$ is presented in Fig. 2.5 where the horizontal axis represents IL displacement and the vertical axis represents CF displacement. The direction of oscillation is indicated using three dots, i.e., the motion starts at the largest dot, then proceeds to the smaller ones. Four distinct orbit types are plotted using four different colors. When $\theta = \pi$, the displacement orbit assumes a figure-eight shape and the riser IL motion is from left to right when passing the outermost CF positions. In accordance with terminology used by Modarres-Sadeghi et al. [40], this orbit shape is characterized as counter-clockwise figure-eight and is colored red. Similarly, the orbit shape associated with $\theta = 0$ is characterized as clockwise figure-eight and is colored blue. The terminology and color coding for the counter-clockwise and clockwise figure-eight shapes are consistent with those used in Figs. 2.3 and 2.3. When $\theta = -\pi/2$, the displacement orbit takes the shape of the letter "C" and is colored green and when $\theta = \pi/2$, the displacement orbit takes the shape of a mirrored letter "C" and is colored cyan. When θ takes on intermediate values different from ones explicitly noted above, e.g., when $\theta = -\pi/4$, the associated displacement orbit takes the shape of a hybrid of a clockwise figure-eight and a letter "C".

Given measured IL and CF displacement time series, $x(t)$ and $y(t)$, respectively, their instantaneous amplitudes, $A_x(t)$ and $A_y(t)$, as well as the phase angle, $\theta(t)$, may be estimated from their analytic signals constructed using the Hilbert transform. Details related to the construction of the analytic signal and a background on the Hilbert transform may be found in Appendix B and in other references (see, for example, Bendat and Piersol [6]).

Using the uniform current data set, NDP2120, for illustration, displacement orbits measured at accelerometer no. 5 ($x/L = 0.56$) are compared over a short interval of time, with ones reconstructed from estimates of $A_x(t)$, $A_y(t)$ and $\theta(t)$. In Fig. 2.6, the orbits are plotted using the same color designations that were used in Fig. 2.5. Orbit shapes constructed from theoretical considerations (i.e., on the basis of Eq. 2.2) using estimated phases and amplitudes are close to the measured orbits as seen in Fig. 2.6 where the estimated phase

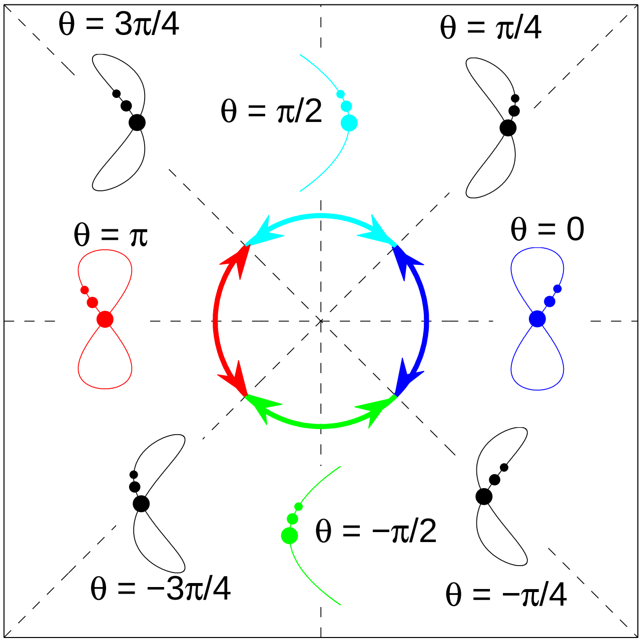

Figure 2.5: Displacement orbits associated with different values of θ as defined in Eq. 2.2.

angles are noted on each plot. That the reconstructed displacement orbits (dashed lines) match the measured orbits reasonably well is an indication that the instantaneous displacement amplitudes, $A_x(t)$ and $A_y(t)$, and the phase angles, $\theta(t)$, may be quite accurately estimated with the help of the Hilbert transform.

The time-varying phase angles, $\theta(t)$, and CF displacement amplitudes, $A_y(t)$, are estimated at the eight locations where displacement (acceleration) measurements are available. Results for the uniform current data set, NDP2120, are plotted in Fig. 2.7, while results for the sheared current data set, NDP2350,

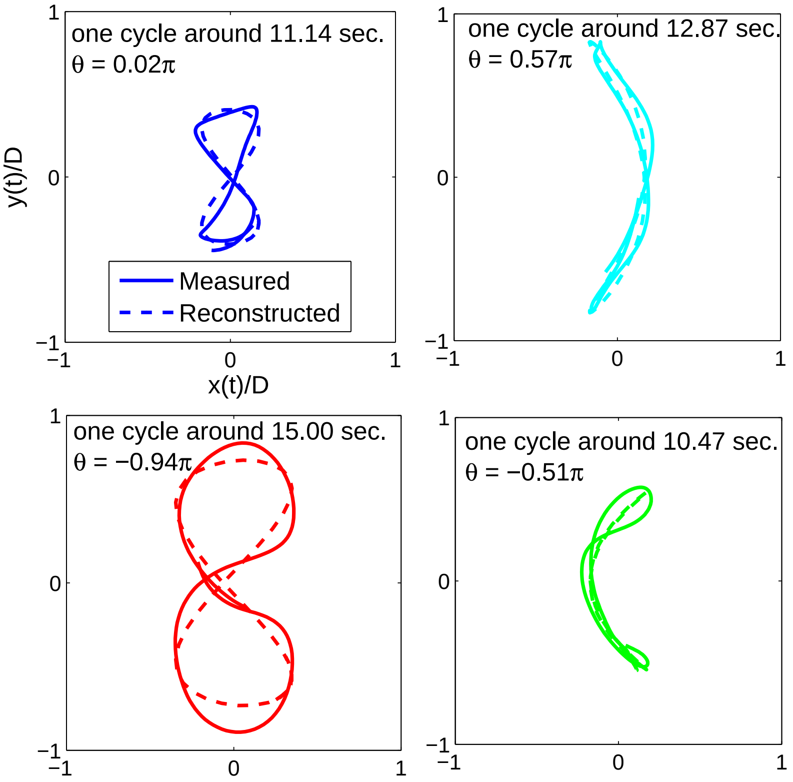

Figure 2.6: Displacement orbits: measured versus reconstructed using estimation of instantaneous amplitudes, $A_x(t)$ and $A_y(t)$, and phase angle, $\theta(t)$.

are plotted in Fig. 2.8. In these figures, the different colors indicate associated phase angles (consistent with the color coding used in Fig. 2.5); for example, the blue color indicates that the phase angle lies in the range, $-\pi/4 < \theta < \pi/4$.

Observations with the uniform current data set, NDP2120, suggest that (i) the phase angles as well as the CF displacement amplitudes vary considerably with time and spatial location (the variation with time is an indicator of obvious non-stationary character in the VIV response); and (ii) the largest CF amplitude, which is slightly in excess of $1D$ (where D is the riser diameter), occurs at the second sensor ($x/L = 0.23$) and around 24 seconds into the record.

In contrast, for the sheared current data set, NDP2350, at any specified time, the estimated phase angles and the CF displacement amplitudes take on different values at the eight different accelerometer locations, but they remain almost unchanged with respect to time. In summary, based on this analysis, it would appear that riser motions resulting from uniform current profiles exhibit stronger non-stationary characteristics than those from sheared currents.

2.4 Higher Harmonics and Varying Frequency Content

The strong non-stationary characteristics of the riser response observed for the NDP2120 data set suggests that the use of a Fourier transform alone on an entire record may not give an adequate representation of the time-varying frequency content of the riser response. Instead, using a continuous wavelet transform (CWT), the variation with time in the dominant frequencies of the signal both in the first and in higher harmonics, when present, can be easily understood by studying scalograms (which indicate the squared modulus of the wavelet transform as it varies with time and scale). Additional details related to the wavelet transform and its applications in civil engineering may be found in Appendix C and in other references (see, for example, Kijewski and Kareem [30]).

Scalograms, using the Morlet wavelet function, of acceleration measurements at the location, $x/L = 0.11$, for the uniform current and the sheared current data sets, NDP2120 and NDP2350, respectively, are presented in Fig. 2.9. The warm colors indicate concentration of energy in certain time intervals and over certain frequency bands. The scalogram for the NDP2120 (uniform cur-

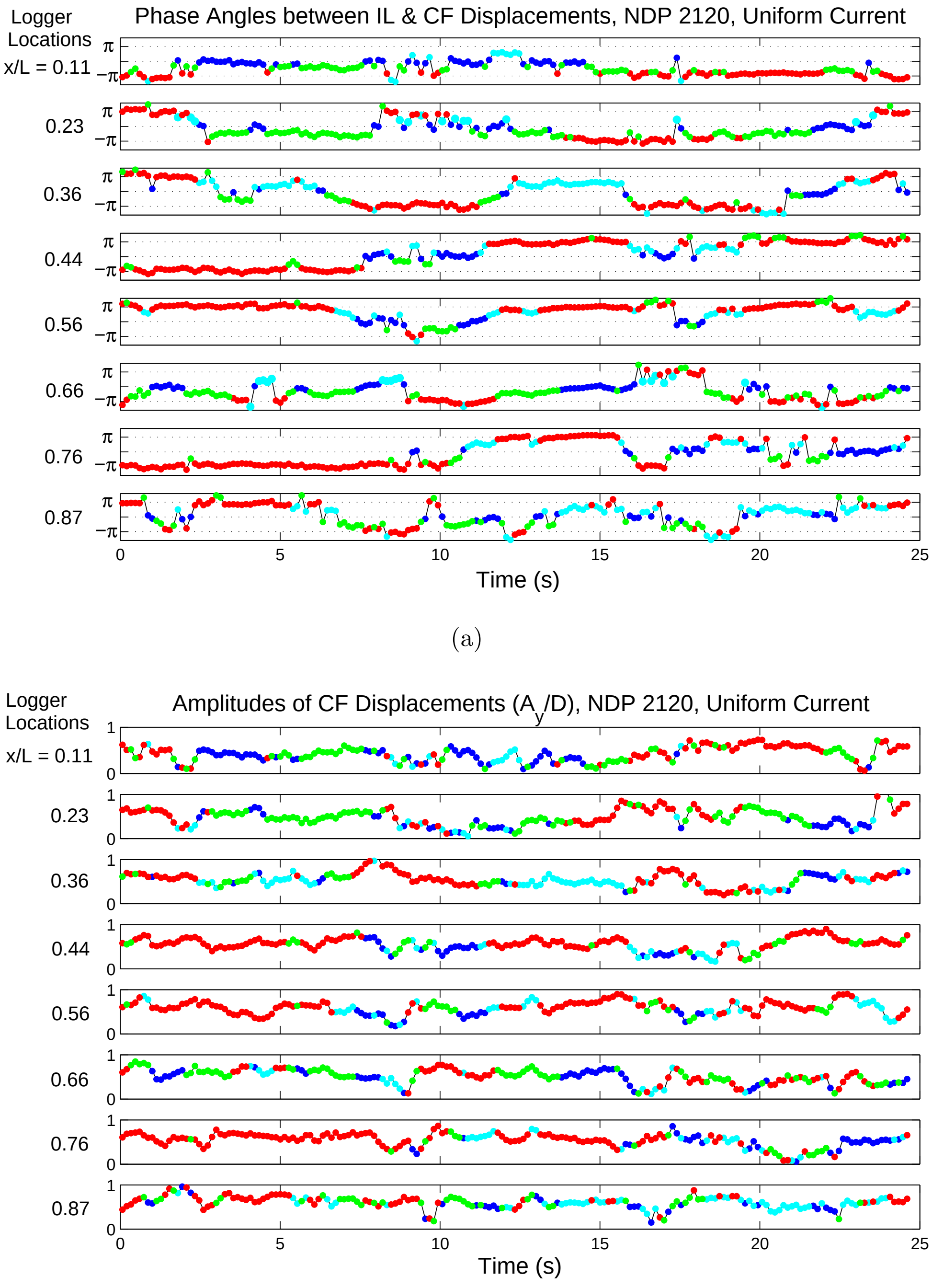

Figure 2.7: The NDP2120 (uniform current) data set: (a) phase difference between IL and CF displacements; and (b) normalized amplitude of CF displacement.

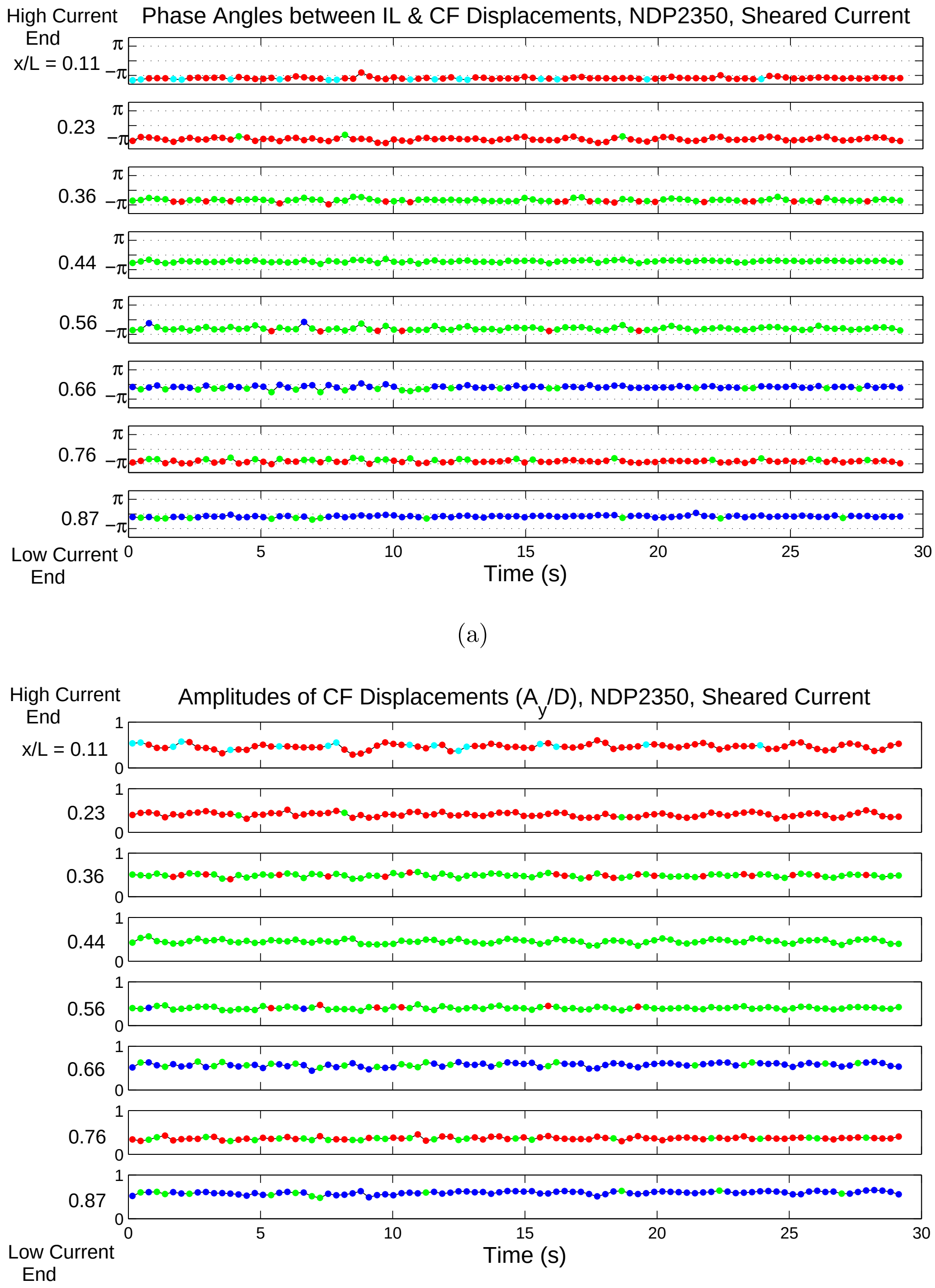

Figure 2.8: The NDP2350 (sheared current) data set: (a) phase difference between IL and CF displacements; and (b) normalized amplitude of CF displacement.

rent) data set shows the presence of a dominant first harmonic (around 7 Hz) as well as a third harmonic (around 21 Hz) in the measured accelerations. Interestingly, the first harmonic does not persist to the same degree (i.e., with the same intensity) over the entire duration; also, the frequencies associated with both the first and third harmonics show some variation with time. These observations confirm the non-stationary character of the riser response for the NDP2120 data set. In contrast, though the scalogram for the NDP2350 (sheared current) data set also shows energy distribution at the first harmonic (around 3 Hz) and at the third harmonic (around 10 Hz) in the measured acceleration signal, the first harmonic does persist for almost the entire record (it does for the first 47 seconds; unknown disturbances occurred after that as can be confirmed by studying Fig. 2.11). Moreover, this first harmonic frequency remains almost constant with time, while the third harmonic, too, only shows very slight variation with time. It is the persistence and steadiness of the dominant first harmonic that leads to relatively more stationary characteristics for the NDP2350 (sheared current) data set compared to the NDP2120 (uniform current) data set, as was noted earlier while studying the amplitudes and phases of riser displacements in Figs. 2.7 and 2.8.

The scalograms of acceleration signals measured at eight locations for the NDP2120 (uniform current) data set, and the NDP2350 (sheared current) data set are presented in Figs. 2.10 and 2.11, respectively. The frequency band used in the figures covers a range that includes only the first harmonic frequency (5 to 10 Hz for NDP2120, and 1 to 6 Hz for NDP2350). Note that the eight rows in each figure use the same color map, i.e., at all sensor locations, the signal intensity is scaled in the same way. Two observations may be made

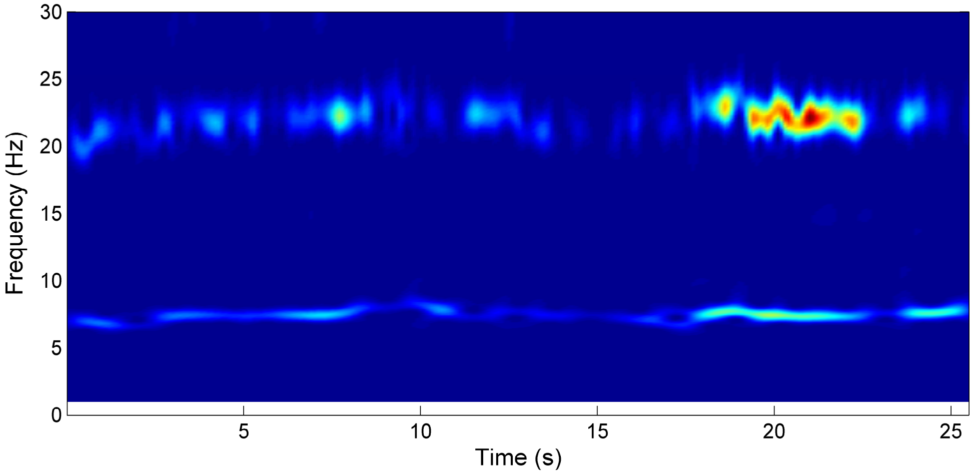

(a)

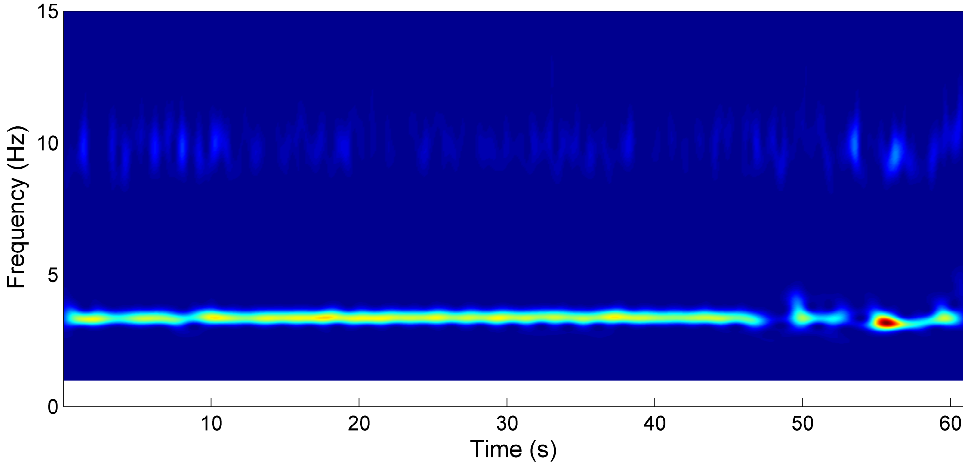

(b)

Figure 2.9: Morlet wavelet scalograms of accelerations measured at location, $x/L = 0.11$, for (a) the NDP2120 (uniform current) data set; and (b) the NDP2350 (sheared current) data set.

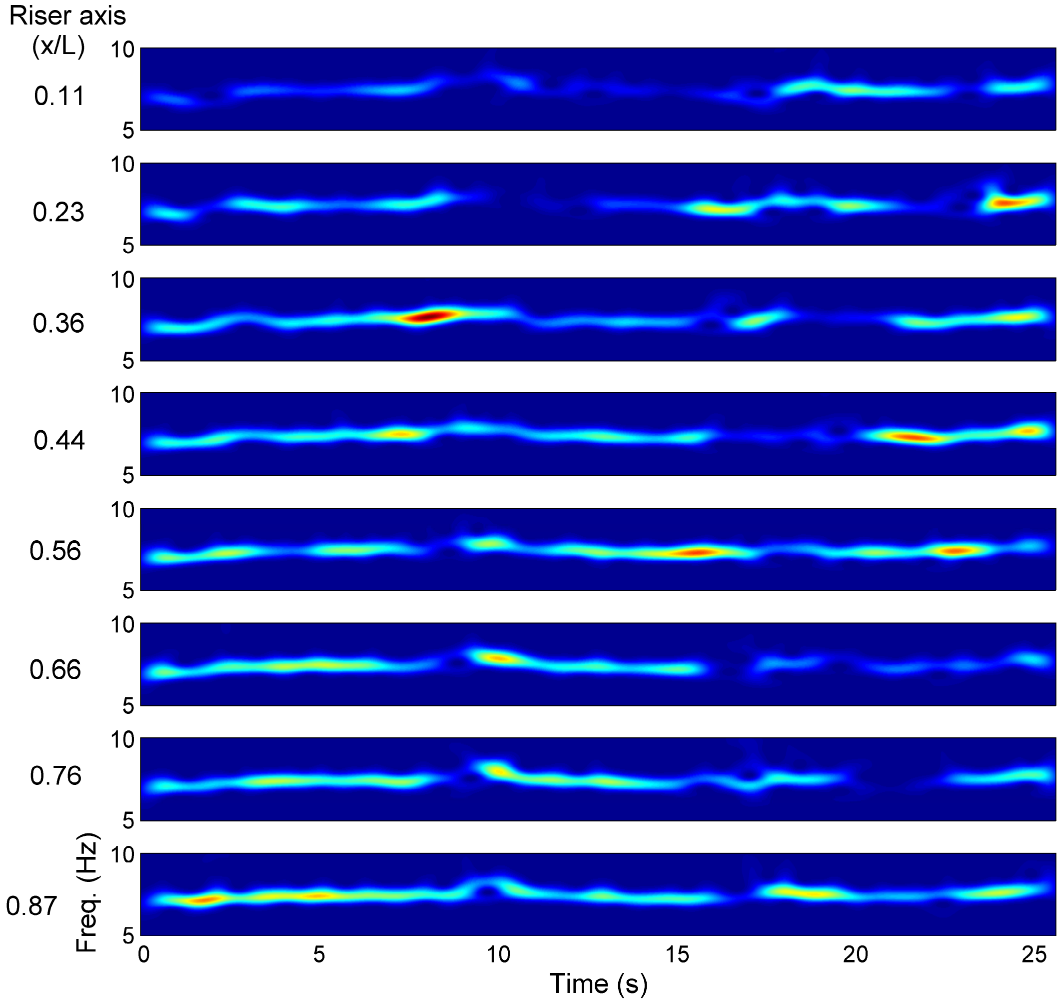

Figure 2.10: Morlet wavelet scalograms of accelerations measured at eight locations for the NDP2120 (uniform current) data set.

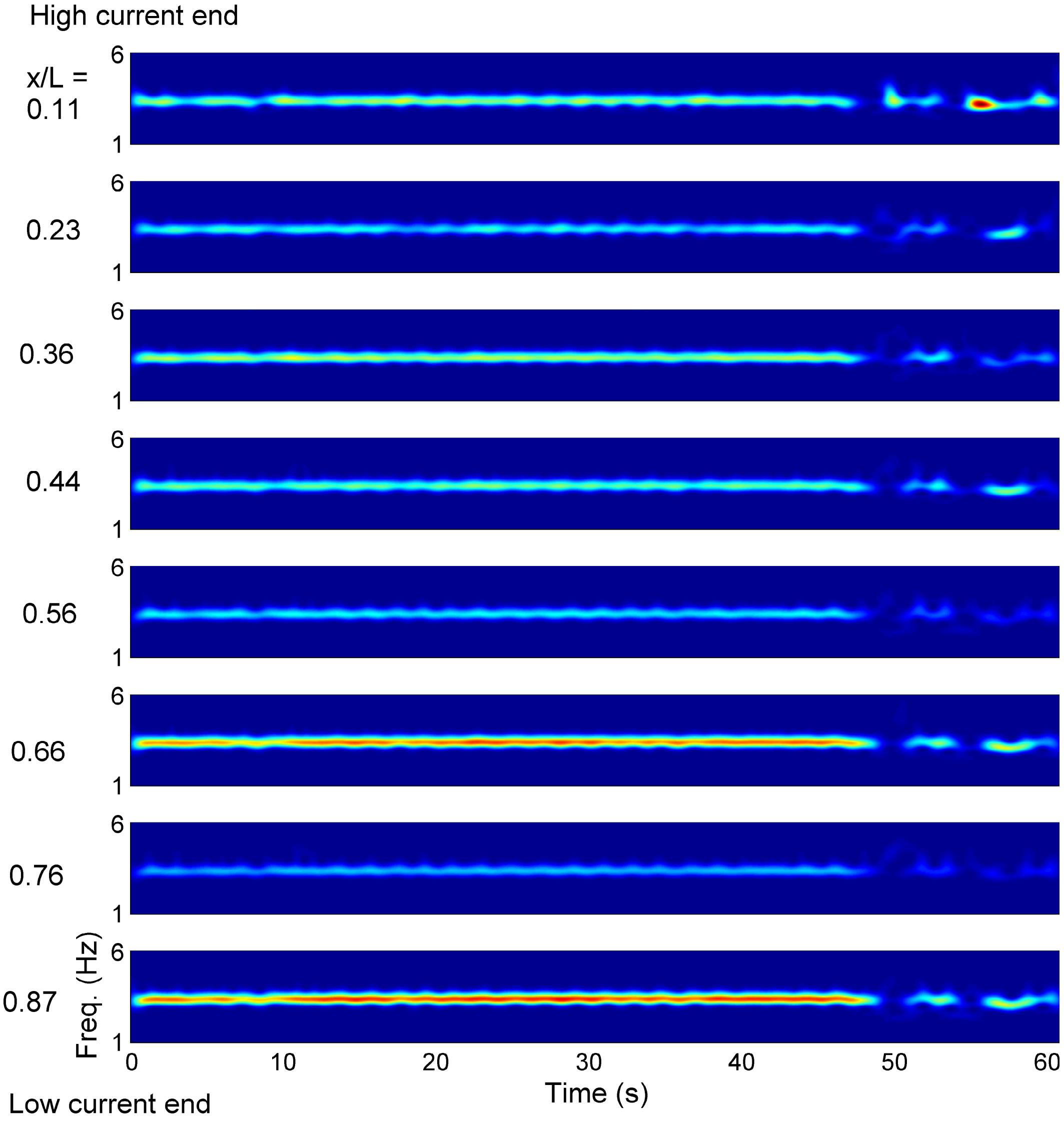

Figure 2.11: Morlet wavelet scalograms of accelerations measured at eight locations for the NDP2350 (sheared current) data set.

based on Fig. 2.10: (i) at a single location, the first harmonic does not persist with the same intensity over the entire duration and its frequency shows some variation with time; and (ii) the location where the largest response occurs changes with time. For instance, at around 2 seconds, the location, $x/L = 0.87$, experiences the largest response; at around 8 seconds, the location, $x/L = 0.36$, experiences the largest response; and at around 21 seconds, the location, $x/L = 0.44$, experiences the largest response. This suggests that different sections along the riser compete with each other to extract energy from the current field. This is because the current speed is uniform over the riser length; thus, each section of the riser has comparable propensity for excitation by the current field and for synchronization with the vortex shedding. This in turn prevents any dominant VIV response at a single location from lasting for a very long period. It may also help explain why strong non-stationary characteristics are observed in the VIV response for the NPD2120 (uniform current) data set.

In contrast, Fig. 2.11 shows different characteristics of the accelerations measured for the NDP2350 (sheared current) data set. At every location along the riser, the intensity and frequency associated with the first harmonic remain almost unchanged over the first 47 seconds. This is consistent with preceding discussions and suggests that the VIV response for the NDP2350 (sheared current) data set may be assumed stationary. The abrupt change in the scalograms that occurs at around 47 second is caused by unknown interruptions. Larger VIV response levels occur at the location, $x/L = 0.87$, near the low current end. This might be because, for the sheared current data sets, waves generated near the high-current end travel downward and are reflected back at the low-current end. The incident and reflected waves cause a standing wave pattern with large amplitudes near the low-current end. Traveling wave characteristics of the VIV response are discussed next.

2.5 Traveling Wave Patterns

In addition to non-stationary characteristics and higher harmonics, the occurrence of traveling waves is another feature often seen in the VIV response of the NDP model riser under excitation either by uniform or sheared currents, though with some differences in the two cases. For the uniform current data sets, traveling wave characteristics do not persist over the entire length of the record. Also, the traveling wave pattern is weak and occurs only over a portion of the riser, not over its entire length. The wave propagation direction is seen to vary even though the current field is uniform and unchanging. The fraction of time a traveling wave is present as well as its intensity varies among the NDP uniform current data sets and no clear trend is observed with respect to the current speed. In contrast, for the sheared current data sets, a traveling wave pattern persists over almost the entire length of the record; also, this traveling wave pattern is clearly evident over the entire length of the riser. Energy in the motion is always transferred to the riser from the high-current end and propagates downward in a traveling wave towards the low-current end. In the following, two examples–NDP2120 (uniform current) and NDP2350 (sheared current)—are employed to illustrate the traveling wave patterns commonly observed in the VIV response of the NDP model riser.

Figure 2.12 depicts waterfall plots of the CF bending strains measured at 24 sensor locations for the uniform current data set, NDP2120, where the abscissa indicates time and the ordinate indicates location along the riser. Figure 2.12(a) shows a one-second segment (from 4 to 5 sec) of the CF bending strains; it appears that a wave is generated at a location around $x/L = 0.25$ and that this wave travels downward. Figure 2.12(b) shows a different one-second segment (from 24 to 25 sec) of the CF bending strains; this time, it appears that a wave is generated at a location around $x/L = 0.8$ and that this wave travels upward. The variation in the direction of the wave propagation is likely because, with a uniform current profile, there is an equal propensity for any portion of the riser to serve as the power-in region; the resulting wave propagation direction is then determined by competition among the candidate lock-in regions.

Figure 2.13 depicts a two-second segment of the CF bending strains measured for the sheared current data set, NDP2350. The recurring diagonal stripes in the figure offer clear evidence of a strong traveling wave that is dominant over almost the entire length of the riser; it is only in a small region close to the high-current end ($x/L = 0$) that the response appears to be that of a standing wave; this presumably results from the combined effects of incident and reflecting traveling waves at a boundary and, hence, is also observed at the low-current end sometimes.

As is clear from the preceding discussion, different traveling wave patterns are observed in waterfall plots based on the strain measurements. From these waterfall plots, the propagation speed of the traveling waves and, hence, the added mass coefficient, C_a, may be estimated, based on knowledge of some physical properties of the model riser.

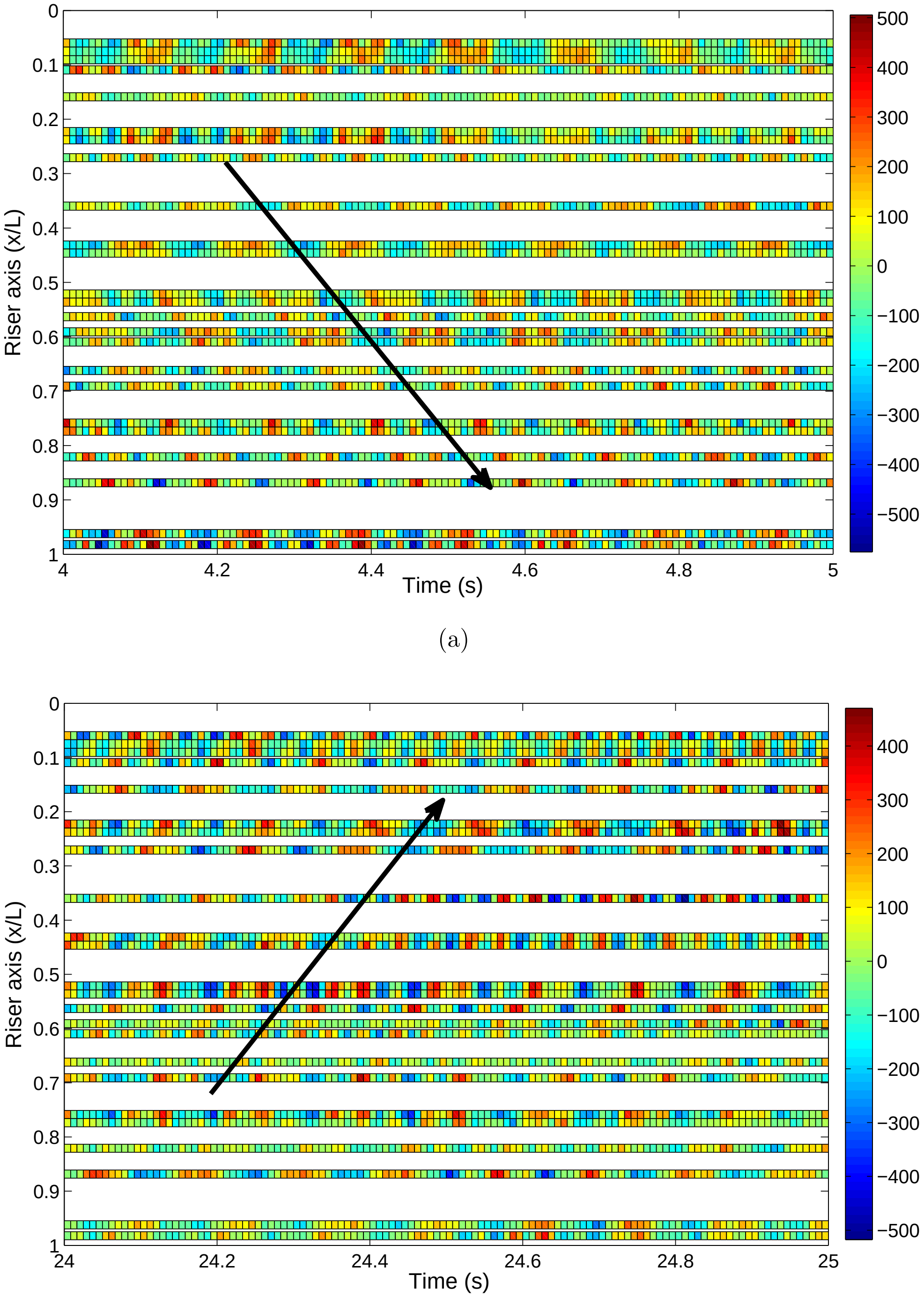

(a)

(b)

Figure 2.12: Traveling wave patterns for the NDP2120 (uniform current) data set: (a) oscillations generated at the upper portion of the riser propagate downward; and (b) oscillations generated at the lower portion of the riser propagate upward.

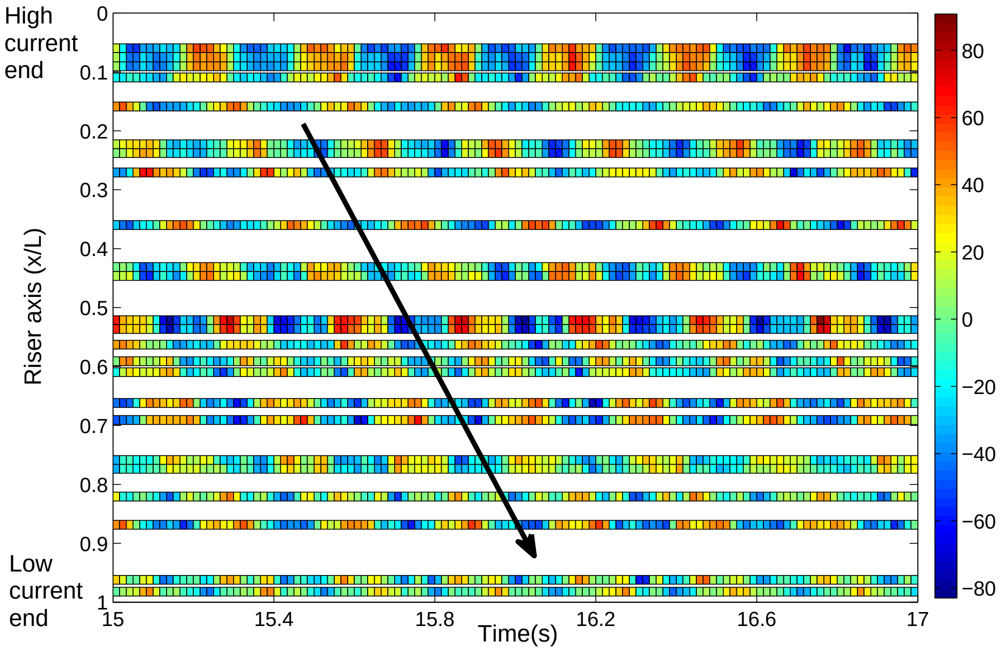

(a)

Figure 2.13: Traveling wave patterns for the NDP2350 (sheared current) data set: oscillations generated at the high-current end propagate downward to the low-current end.

At low mode number, the NDP model riser can be represented as a tensioned string because the effect of the bending stiffness is relatively small compared to the effect of the axial stiffness (or string tension) and, hence, may be neglected. For a tensioned string, the propagation speed of a transverse wave is given by:

$$V = \sqrt{\frac{T}{m + C_a m_w}} \tag{2.3}$$

where V is the propagation speed of the traveling waves, T is the tension force, m is the mass of the cylinder (including the filled fluid) per unit length, m_w is the mass of the displaced water per unit length, and C_a is the added mass coefficient.

The physical properties of the cylinder (i.e., the model riser) are listed in Appendix A. The tension force, T, is assumed to be constant along the length and equal to 4000 N; the mass of the cylinder, m, is 0.933 kg/m; and the mass of the displaced water, m_w, is 0.576 kg/m. The propagation speeds of the traveling waves for the NDP2120 and NDP2350 data sets are estimated from the waterfall plots of the strain signals. First, we divide the entire record of strains into short segments and prepare waterfall plots for each segment. Next, we compute the slopes of observable diagonal stripes from the waterfall plots. Finally, we use the averaged value (over all segments) of the computed slopes as an estimate of the speed of the traveling waves. The added mass coefficient may now be estimated using Eq. 2.3 with the estimated speed of the traveling waves and known physical properties of the cylinder. Values of the estimated wave propagation speed and added mass coefficient, C_a, for the four NDP data sets are presented in Table 2.1. We see that the added mass coefficient, C_a, has values of approximately zero and unity, respectively, for the two uniform current data sets and the two sheared current data sets—i.e., if C_a is assumed to be 0 and 1, respectively, for the uniform and sheared current data sets, the computed propagation speed of the waves based on Eq. 2.3 and listed in the last column of Table 2.1 closely matches the estimated wave propagation speed from the strain waterfall plots.

The assumption that $C_a = 0$ for the uniform current data sets and that $C_a = 1$ for the sheared current data sets will be used in Chapter 3 where the VIV response over the entire span of a riser will be reconstructed using

Table 2.1: Estimates of the added mass coefficient (C_a) based on empirically estimated values of the wave propagation speed.

Event no.	Current profile	Estimated speed (m/s)	Estimated C_a	Computed wave speed (m/s)
2120	Uniform	65.0	0.02	65.6
2150	Uniform	63.5	0.10	assuming $C_a = 0.0$
2350	Sheared	48.9	1.28	51.5
2420	Sheared	52.3	0.92	assuming $C_a = 1.0$

empirical methods and measurements taken at a limited number of locations.

2.6 Concluding Remarks

In this chapter, displacement, acceleration, and strain signals obtained from the NDP bare model riser experiments, were examined to study various complex characteristics of the vortex-induced vibration (VIV) response of long flexible cylinders. Higher harmonics, non-stationary characteristics, the variation in frequency content, and traveling wave patterns, which are often observed in measurements on long flexible cylinders or full-scale drilling risers experiencing VIV, were also observed in the NDP model riser data sets.

The presence of higher harmonics in acceleration or strain signals can be examined by using spectral analysis techniques, assuming the VIV response is stationary. The frequencies of each harmonic mode can be identified from PSD plots. The relationship between the harmonic mode frequencies and the current speed was found to be linear for the NDP data sets; the proportional constant was estimated using least-squares fitting. Results showed that the

Strouhal number associated with long flexible cylinders are smaller than that estimated from stationary cylinder experiments.

The temporal evolution and spatial variation of riser displacement orbits showed that the VIV response of long flexible cylinders (such as in the NDP model riser data sets) can be non-stationary and quite complex. Mathematical tools, such as the Hilbert transform and the wavelet transform, are useful to study complex characteristics of such VIV response. Using the Hilbert transform, instantaneous amplitudes and phase angles (associated with displacement orbits) can be estimated from measured cross-flow and in-line displacements; these can then be used to examine non-stationary characteristics of the riser response. Scalograms (describing squared coefficients of wavelet transforms) of measured acceleration or strain signals help to reveal the presence and variation of different harmonics in the riser response.

Traveling wave patterns were observed in the VIV response of the NDP model riser, albeit with different characteristics for uniform versus sheared currents. In addition, the added mass coefficient was estimated based on estimation of the wave propagation speed from strain measurements.

All of the complex characteristics described above and observed in the NDP model riser measurements should be taken into account, if possible, when reconstructing/predicting the riser response and when estimating fatigue damage rates associated with VIV.

Chapter 3

Empirical Procedures for Fatigue Damage Rate Estimation

3.1 Introduction

Vortex-induced vibration (VIV) is a major contribution to fatigue damage of marine risers. Accumulated fatigue damage can cause riser failure, a shortened service life, and even ocean pollution. To prevent such catastrophic consequences, it is useful to be able to accurately estimate the rate of fatigue damage accumulation and the expected service life of a marine riser at the design stage, and to monitor the accumulated fatigue damage and predict the remaining life for an installed riser. In an effort to achieve this ambitious goal, several marine riser monitoring campaigns have been undertaken over the past decade [52]. Riser response (in the form of strains and/or accelerations) is usually measured at discrete locations along the riser. Often, ocean currents are also measured at a nearby location over the period of the riser monitoring campaign. Such in-situ full-scale measurements are extremely valuable in the study of riser VIV response and the estimation of fatigue damage.

In contrast to the use of riser response measurement campaigns, given a current profile and the physical properties of a riser, the response and fatigue damage rate of a riser may be estimated using available analytical and/or semi-empirical software tools. The estimated riser response, though, with many of these tools, usually only accounts for energy at the Strouhal frequency (the first harmonic) and neglects higher harmonics (frequencies that are multiples of the Strouhal frequency); as a result, fatigue damage rates may be underestimated by a factor as large as 40 [58]. Some recent studies have presented approaches to incorporate higher harmonics in fatigue damage estimation (see, for example, Jhingran and Vandiver [26] and Modarres-Sadeghi et al. [40]). The general idea is to estimate the ratio of the response contribution from higher harmonics to that from the first harmonic using recorded measurements and, then, to use that ratio to modify the fatigue damage rate estimated based on the first harmonic alone.

In the present study, several empirical methods are employed to estimate the VIV response and fatigue damage rates over the entire length of a riser from measurements at a limited number of discrete locations. Unlike VIV analysis software, empirical methods only rely on data (i.e., the measured riser response); no physical properties of the riser are required (or, in some cases, very limited such information is needed); and no information on the current profile is needed at all. Five empirical methods, referred to as WWA (Weighted Waveform Analysis), modified WWA, POD (Proper Orthogonal Decomposition), MPR (Modal Phase Reconstruction), and a hybrid method that combines MPR and modified WWA, are presented. Four NDP data sets (available in the public domain) are employed to test and compare the different methods. The riser response and fatigue damage rates over the entire riser length are estimated using strain measurements from a limited number of sensors. The mathematical formulation and basis for each method is briefly presented in the following; underlying assumptions, advantages, and disadvantages of each method are discussed with examples. By comparing the estimated riser response and fatigue damage rates at selected locations with those obtained directly from the measurements, it is found that all the empirical methods discussed, despite the different underlying assumptions in each of them, may be employed to estimate fatigue damage rates quite well from limited measurements.

3.2 Data Sets Used and Fatigue Damage Calculation

In this chapter, four NDP bare riser data sets (available in the public domain at the VIV data repository [11]) are used to illustrate and test the empirical response reconstruction methods. As presented in Appendix A, the RMS (root-mean-square) values of the CF displacements measured for these four data sets are relatively large; hence, the riser is thought to be experiencing VIV and these four data sets are well suited for this study.

Given cross-flow (CF) and in-line (IL) measurements at the same cross-section of a riser, Baarholm et al. [3] computed the fatigue damage at several points along the outer circumference and noted that the maximum fatigue damage for that cross-section was usually equal to the larger of the CF fatigue damage and the IL fatigue damage. For the four NDP data sets, estimates of fatigue damage rates at the locations of the 24 CF strain sensors and the 40 IL strain sensors are illustrated in Fig. 3.1. It is seen that the CF fatigue damage is almost always larger than the IL fatigue damage; this suggests that the fatigue life is largely controlled by the CF fatigue damage for these NDP data sets. Hence, in this study, only the CF response and fatigue damage are

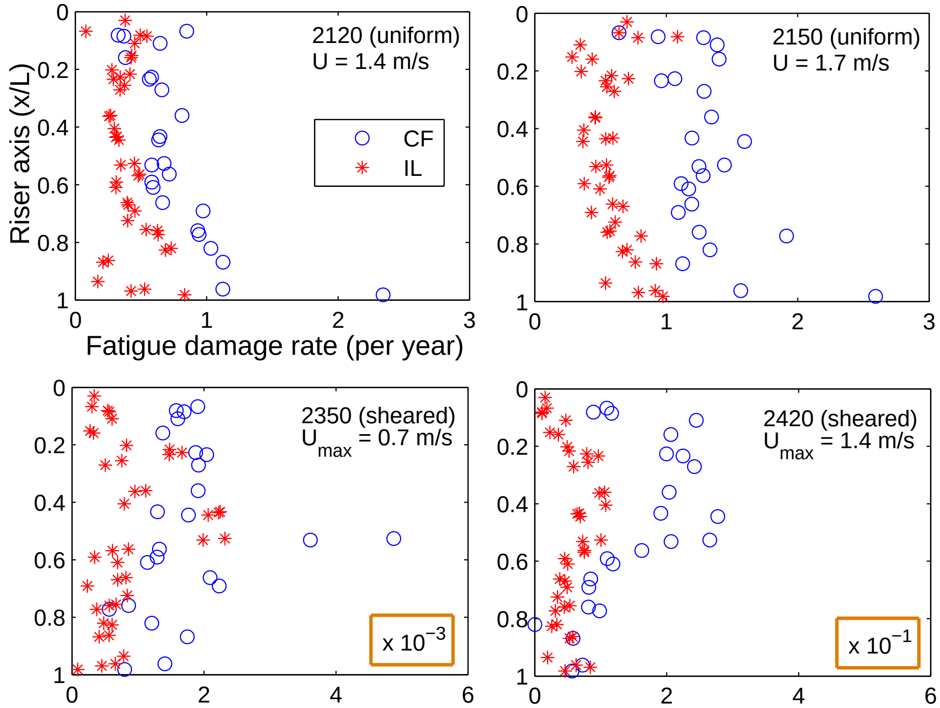

Figure 3.1: Measured CF and IL fatigue damage rates associated with the four NDP data sets.

considered. However, the empirical methods can also be applied to estimate the fatigue damage in the IL direction if that is of interest.

The fatigue damage rate can be estimated based on Miner's rule, a selected S-N curve, and an empirically derived probability distribution of stress ranges at the critical fatigue location of interest. By neglecting or purposely filtering out higher harmonic components, the VIV response of risers may be assumed to only contain energy around the Strouhal frequency, and the stress time history may be assumed to be a narrow-band Gaussian process; then stress ranges will follow a Rayleigh distribution whose single parameter depends only on the variance (i.e., the zeroth spectral moment) of the stress process at the critical location. However, as discussed in Chapter 2, higher harmonics are often significant in the VIV response of risers. The presence of higher harmonics means that the VIV-related stress may not be approximated as a narrow-band Gaussian process and, hence, stress range in turn will not follow a Rayleigh probability distribution. Instead, the stress time series is broad-banded and the stress range probability distribution may be formulated, for example, using Dirlik's method [15], which employs the zeroth, first, second, and fourth spectral moments of the stress time series. As an alternative to such spectral fatigue techniques, the stress range distribution and fatigue damage rate may also be estimated in the time domain, such as by using the rainflow cycle-counting technique ([38], [17]). Fatigue damage rates estimated based on rainflow cycle-counting technique are, in general, more accurate than those based on spectral approaches when stress time series are available because they do not rely on simplifying assumptions on the random stress process (as spectral approaches do).

In this study, given stress (obtained from strain) time series measured or reconstructed, the fatigue damage rate is computed using Miner's rule, the rainflow cycle-counting algorithm, and the F-2 S-N curve for the NDP model riser. The F-2 S-N curve is expressed as follows:

$$N = aS^{-b} \tag{3.1}$$

where N is the number of cycles to failure at stress range, S; also, $a = 4.266 \times 10^{11}$ and $b = 3.0$ are parameters of the F-2 S-N curve [4].

The NDP model riser experiments provided measured CF strains at 24 locations and CF accelerations at 8 locations (the 8 acceleration loggers were at the same locations as 8 of the 24 strain loggers). However, in this study, only the strain data are used as inputs to the empirical methods in order to reconstruct the riser response. Two scenarios are considered: (i) where a large number (here, 23) of strain loggers are available; and (ii) where a small number (here, 8) of strain loggers are available. Accelerations are not used as inputs; however, displacements (obtained by double-integration of available acceleration data) sometimes serve as a check of the accuracy of the response reconstruction by the empirical methods.

3.3 Empirical Fatigue Damage Rate Estimation

The densely instrumented NDP model riser (with twenty-four strain sensors in the CF direction) allows us to test different empirical methods by use of cross-validation where estimations can be compared to measurements as follows. First, we select any one sensor as the "target" sensor and use the remaining twenty-three sensors as "input" sensors; we use the empirical method under consideration along with measurements from the input sensors to estimate strain time series at the location of the target sensor. Next, we assess the fatigue damage rate at the location of the target sensor from the estimated strain and compare it with the "measured" value—i.e., that value of the fatigue damage rate that is computed directly from the strain measured by the target sensor (but never used in estimation by the empirical method). Note that the fatigue damage rates, both the estimated and measured values, are estimated from the strain time series by using the rainflow cycle-counting algorithm, Miner's rule, and the selected F-2 S-N curve. We iterate by selecting a different target sensor each time until all the twenty-four sensors have been selected. These iterative steps are followed for each empirical method. A single parameter, the Damage Ratio (DR), defined as the ratio of the estimated fatigue damage to the true fatigue damage at the target sensor, is used as an indicator of the "quality" of the empirical method.

In the following, the theoretical formulation for each empirical method is presented very briefly. Then, using a sheared current data set, NDP 2350, for illustration and making use of strain sensor no. 4 (where $x/L = 0.11$; L is the riser length) as the target sensor, key points including advantages and disadvantages of each method are highlighted. Note that in the various numerical studies presented in the following, we have used other target sensors as well, as we demonstrate the application of the empirical methods presented.

3.3.1 Weighted Waveform Analysis (WWA)

Weighted Waveform Analysis (WWA) is a computational procedure that is widely used to analyze and reconstruct the response over the entire length of a riser from measurements at a limited number of sensors [54], [33].

Assume that the riser displacement, x, at location, z, and at time, t, may be expressed approximately as a weighted sum of N modes. Thus, we have:

$$x(z,t) = \sum_{i=1}^{N} w_i(t)\varphi_i(z) \tag{3.2}$$

where it is assumed that by selecting N (not necessarily consecutive) modes, one can represent the riser displacement at any location, z. Also, $\varphi_i(z)$ represents the ${n_i}^{\text{th}}$ mode shape of the displacement, while $w_i(t)$ represents the time-varying modal weight to be applied to the ${n_i}^{\text{th}}$ mode shape. Note that, by "mode" in the empirical methods discussed here, we mean a deformed shape of the riser associated with dominant energy in the PSD of the CF strain at the loggers.

Assume that the mode shapes are represented as sinusoidal functions:

$$\varphi_i(z) = \sin\left(\frac{n_i \pi z}{L}\right) \tag{3.3}$$

where L is the riser length. Then, the bending strain, which equals the product of the riser outer radius, R, and the local curvature, x'', may be expressed as follows:

$$\varepsilon(z,t) = Rx''(z,t) = \sum_{i=1}^{N} Rw_i(t)\varphi_i''(z) \tag{3.4}$$

where $\varphi_i''(z) = -\left(n_i\pi/L\right)^2 \varphi_i(z)$ is the curvature of the n_ith mode shape.

Given strain measurements or, equivalently, curvature measurements at M logger locations, z_j (where $j = 1$ to M), WWA requires solution of a system of equations in matrix form:

$$\mathbf{A}\mathbf{w} = \mathbf{d} \tag{3.5}$$

where the $M \times N$ matrix, $\mathbf{A}$, comprises curvatures of the assumed mode shapes at all the logger locations and the vector, $\mathbf{d}$, represents riser curvatures and is formed from the measured strains at all loggers, i.e.:

$$\mathbf{A} = \begin{bmatrix} {\varphi''}_1^1 & {\varphi''}_2^1 & \cdots & {\varphi''}_N^1 \\ {\varphi''}_1^2 & {\varphi''}_2^2 & \cdots & {\varphi''}_N^2 \\ \vdots & \vdots & \vdots & \vdots \\ {\varphi''}_1^M & {\varphi''}_2^M & \cdots & {\varphi''}_N^M \end{bmatrix}; \quad \mathbf{w} = \begin{bmatrix} w_1 \\ w_2 \\ \vdots \\ w_N \end{bmatrix}; \quad \mathbf{d} = \begin{bmatrix} \varepsilon_1/R \\ \varepsilon_2/R \\ \vdots \\ \varepsilon_M/R \end{bmatrix} \tag{3.6}$$

where ${\varphi''}_i^j = -\left(n_i\pi/L\right)^2 \sin\left(n_i\pi z_j/L\right)$ is the curvature of the n_ith mode shape at logger location, z_j. Equation 3.5 is a linear system of M equations from which N weights need to be estimated. At any instant of time, t, as long as $N \leq M$, the modal weights vector, $\mathbf{w}$, may be solved for in a least-squares sense. Thus, we have:

$$\mathbf{w}(t) = \left(\mathbf{A}^T\mathbf{A}\right)^{-1}\mathbf{A}^T\mathbf{d}(t) \tag{3.7}$$

In the present study, where twenty-three strain sensors are available, we find that careful selection of the modes based on frequencies corresponding to peaks in the CF strain power spectra, generally, provides good WWA-based reconstructed strain time series at target sensors. In our studies, the use of twelve modes (i.e., $N = 12$) was generally a good choice compared to alternatives. The procedure for the selection of the N modes is important and this is briefly described next.

Given the CF strain time series, $\varepsilon(z_j, t)$, measured at each of the twenty-three locations, z_j (where $j = 1, 2, 3, 5, \ldots, 24$; i.e., assume that the target sensor no. 4 does not exist), its power spectral density (PSD), $PSD_j(f)$, describes the energy distribution by frequency of the riser response at that location. As illustrated in Fig. 3.2(a), the twenty-three input strain power spectra indicate very similar frequency content; all these spectra show the presence of the first and third harmonics in the response (the fifth harmonic is also visible if the PSDs were plotted on log scale). The summation of the PSDs for all the twenty-three sensors, i.e., $\sum_j PSD_j(f)$ (see Fig. 3.2(b)) is assumed to account for the energy distribution by frequency over the entire riser and is, therefore, used for the WWA mode selection. First, the twelve separate peaks which have highest spectral values are identified. As illustrated in Fig. 3.2(b), the selected peaks cover the first, third and fifth harmonics as well as the second and fourth harmonics of the input signals. Second, the associated mode numbers are determined by comparing these peak frequencies with the estimated natural frequencies of the riser. The riser is assumed to be dominated by tensioned-string behavior and its bending stiffness is assumed to be negligible. Note that the riser's natural frequencies are theoretically calculated using the physical properties of the riser and an assumed added mass coefficient. Thus, we have:

$$f_n = \frac{n}{2L}\sqrt{\frac{T}{m + C_a m_w}} \tag{3.8}$$

where f_n is the n^{th} natural frequency of the riser, L is the riser length, T is the tension in the riser, m is the mass of the riser per unit length, and m_w is the mass of the displaced water per unit length. These various physical properties of the riser are listed in Appendix A. The added mass coefficient, C_a, is related to the propagation speed of traveling waves in the riser, which is estimated from a limited set of measurements (see Chapter 2); for the NDP model riser, we assume $C_a = 0$ for uniform current profiles, and $C_a = 1.0$ for sheared current profiles.

After selection of the assumed modes for the WWA procedure, the response (displacement) over the entire length of the riser may be reconstructed using Eqs. 3.2, 3.3 and 3.7. Strain time series at locations over the entire length of the riser, including at the location of the target sensor, may also be reconstructed using Eq. 3.4. Figure 3.2(c) compares the energy distribution by frequency in the reconstructed CF strain PSD (dashed red line) with the CF strain PSD obtained directly from measurements (solid blue line) at the location of the target sensor (sensor no. 4); the comparison suggests that the first and higher harmonics are reasonably well represented by application of the WWA procedure. Figure 3.2(d) presents RMS curvature values at the locations of the twenty-four sensors based on measurements; the blue circles indicate these values at the twenty-three input sensors, and the red cross indicates the value at the target sensor. The solid line indicates the corresponding RMS curvature estimated by the WWA procedure. The results suggest that the reconstructed curvatures reflect the presence of the first and higher harmonics and that these reconstructed curvatures match measured values reasonably well at all the sensor locations.

The fatigue damage ratio, representing the ratio of the estimated damage to that based directly on measurements at the target sensor (i.e., sensor no. 4), is 1.47, which suggests that the fatigue damage is overestimated by a factor of 1.47 by the WWA method. Similar results for other choices of the target sensor are discussed later.

3.3.2 Modified Weighted Waveform Analysis (Modified WWA)

By introducing cosine terms to complement the sine terms for each frequency component in the WWA method, a modified WWA procedure results that can better account for the influence of traveling waves in the riser response as well as for local curvature changes at boundaries and other discontinuities. In lieu of Eq. 3.2, we now have:

$$\begin{aligned} x(z,t) &= \sum_{i=1}^{N} \left[a_i(t)\varphi_i(z) + b_i(t)\psi_i(z) \right] \\ \varphi_i(z) &= \sin\left(\frac{n_i \pi z}{L}\right); \psi_i(z) = \cos\left(\frac{n_i \pi z}{L}\right) \end{aligned} \tag{3.9}$$

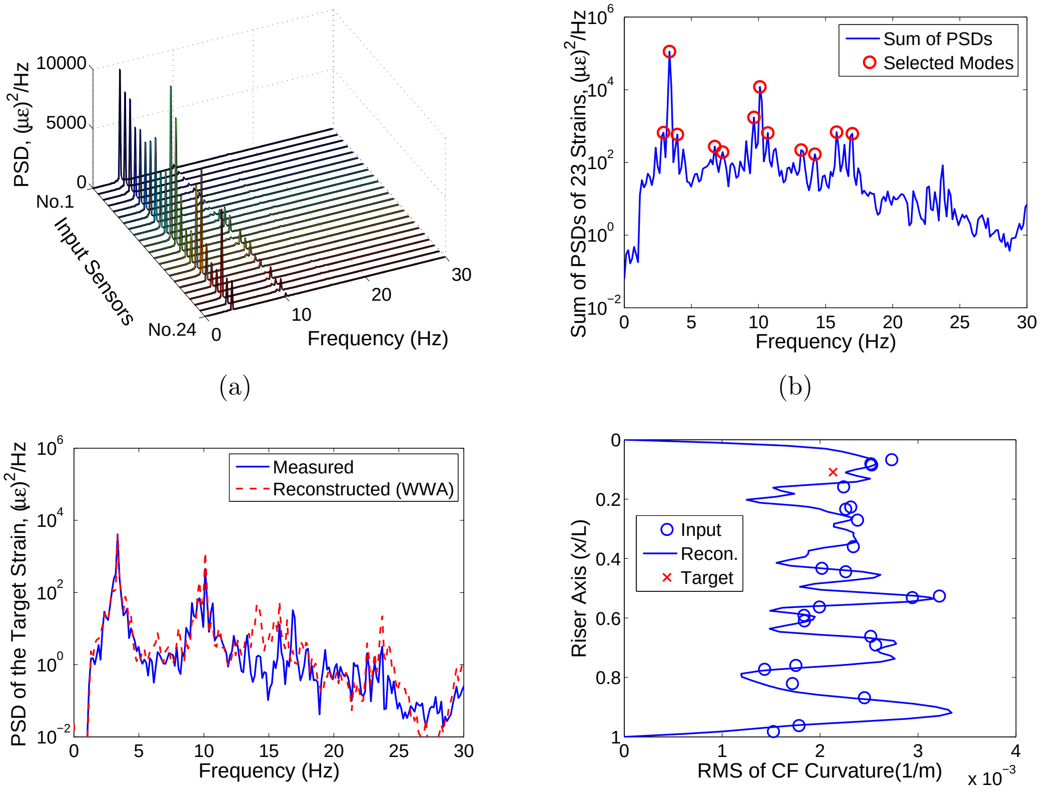

(a) (b)

(c) (d)

Figure 3.2: The WWA procedure applied with twenty-three input sensors (sensor no. 4 is the target) for the NDP2350 (sheared current) data set: (a) PSDs of the strains measured at the twenty-three sensors; (b) summation of the strain PSDs and identification of the selected modes; (c) strain PSD at the target sensor: reconstructed vs. measured; and (d) RMS curvatures: reconstructed vs. measured.

where $a_i(t)$ and $b_i(t)$ are modal weights associated with assumed sine and cosine mode shapes, $\varphi_i(z)$ and $\psi_i(z)$, respectively. Strains are computed in a similar manner as with the WWA method. Thus, we have:

$$\varepsilon(z,t) = Rx''(z,t) = \sum_{i=1}^{N} R\left[a_i(t)\varphi_i''(z) + b_i(t)\psi_i''(z)\right] \qquad (3.10)$$

where $\varphi_i''(z) = -\left(n_i\pi/L\right)^2 \varphi_i(z)$ and $\psi_i''(z) = -\left(n_i\pi/L\right)^2 \psi_i(z)$ are the curvatures of the ${n_i}^{\text{th}}$ sine and cosine mode shapes, respectively.

As with the WWA procedure, given curvature measurements at M logger locations, a system of equations in matrix form results (as in Eq. 3.5), but with modified terms:

$$\mathbf{A} = \begin{bmatrix} \varphi''^1_1 & \psi''^1_1 & \varphi''^1_2 & \psi''^1_2 & \cdots & \varphi''^1_N & \psi''^1_N \\ \varphi''^2_1 & \psi''^2_1 & \varphi''^2_2 & \psi''^2_2 & \cdots & \varphi''^2_N & \psi''^2_N \\ \vdots & \vdots & \vdots & \vdots & \vdots & \vdots & \vdots \\ \varphi''^M_1 & \psi''^M_1 & \varphi''^M_2 & \psi''^M_2 & \cdots & \varphi''^M_N & \psi''^M_N \end{bmatrix}; \mathbf{w} = \begin{bmatrix} a_1 \\ b_1 \\ a_2 \\ b_2 \\ \vdots \\ a_N \\ b_N \end{bmatrix}; \mathbf{d} = \begin{bmatrix} \varepsilon_1/R \\ \varepsilon_2/R \\ \vdots \\ \varepsilon_M/R \end{bmatrix} \tag{3.11}$$

where $\varphi''^j_i = -\left(n_i\pi/L\right)^2 \sin\left(n_i\pi z_j/L\right)$ and $\psi''^j_i = -\left(n_i\pi/L\right)^2 \cos\left(n_i\pi z_j/L\right)$ are curvatures of the ${n_i}^{\text{th}}$ mode sine and cosine shapes at location, z_j, corresponding to sensor no. j. Equation 3.11 is a linear system of M equations with $2N$ weights to be estimated. At any instant of time, t, as long as $2N \leq M$, the modal weights vector, $\mathbf{w}$, may be solved for in a least-squares sense using Eq. 3.7. The riser response such as the CF bending strain, at any location, z, may be reconstructed using Eq. 3.10. Though the modified WWA procedure can better describe traveling waves in the riser response as well as local curvatures (than is possible with the WWA method), the smaller number of modes that may be assumed given the same suite of measurements represents a tradeoff.

We should note that the modified WWA procedure presented here is similar to the spatial Fourier decomposition with the “full reconstruction criterion” that is employed by Mukundan [41], [42]; however, one key difference is that their studies used sequentially ordered modes, while the modified WWA method presented here is based on the selection of important physically excited (energetic) modes that are not, in general, sequential.

With the modified WWA method, where twenty-three input strain sensors are available (i.e., M=23), careful selection of six modes (i.e., N=6) based on generally non-consecutive frequencies corresponding to peaks in the CF strain power spectra provide reconstructed strain time series with reasonable accuracy. Figure 3.3 presents results for the modified WWA method in a similar way to those presented for the WWA method in Fig. 3.2. The PSD for the CF strain at each input logger and the summation of all these PSDs at each frequency are plotted in Figs. 3.3(a) and 3.3(b), respectively. The six modes selected in a similar manner to the procedure used with the WWA method include the first, second, third, fourth, and fifth harmonics of the input signals. Results summarizing the reconstructed CF strain PSD and the reconstructed RMS curvature at the locations of the various sensors are presented in Figs. 3.3(c) and 3.3(d), respectively. The results suggest that at the target sensor, the PSD of the reconstructed CF strain matches the corresponding PSD based on actual strain measurements quite well; also, the RMS values of the reconstructed curvatures match measured values reasonably well at all the sensor locations.

The fatigue damage ratio, representing the ratio of the estimated damage to that based directly on measurements at the target sensor (i.e., sensor no. 4), is 1.62, which suggests that the fatigue damage is overestimated by 62% by the modified WWA method. Similar results for other choices of the

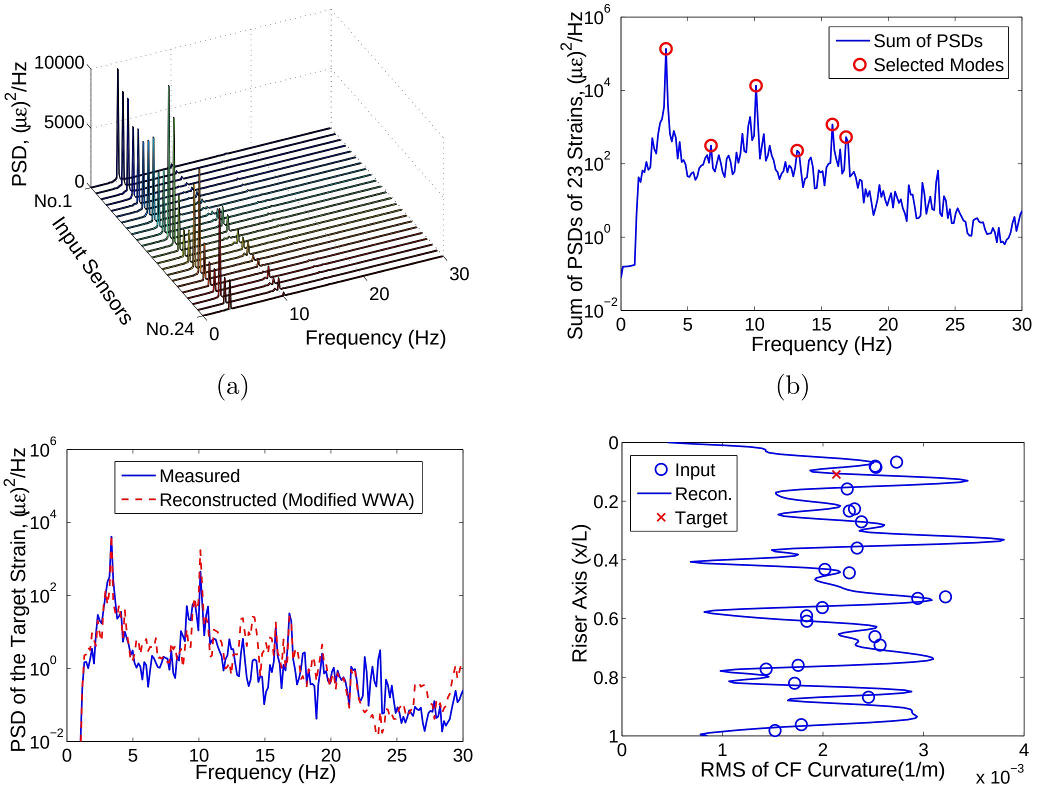

(a) (b)

(c) (d)

Figure 3.3: The modified WWA procedure applied with twenty-three input sensors (sensor no. 4 is the target) for the NDP2350 (sheared current) data set: (a) PSDs of the strains measured at the twenty-three sensors; (b) summation of the strain PSDs and identification of the selected modes; (c) strain PSD at the target sensor: reconstructed vs. measured; and (d) RMS curvatures: reconstructed vs. measured.

target sensor are discussed later.

3.3.3 Proper Orthogonal Decomposition (POD)

The WWA approach presented requires a priori assumed mode shapes based on knowledge of the physical properties of the riser; the modified WWA approach is directly related to these modes by introducing cosine function counterparts to each sine function. For the NDP model riser, the mass and tension force are almost constant along its length; hence, it might be reasonable to assume sinusoidal functions for the mode shapes as was done with the WWA method used in this study. In full-scale prototype risers, the mass and the tension force often vary spatially over the riser length due to, for example, the presence of buoyancy modules and distributed mass. In such cases, riser mode shapes will usually deviate to varying extents from simple sinusoidal functions and they can be difficult to estimate accurately. The error in assumed mode shapes directly affects the accuracy of approaches such as the WWA method and in resulting estimations of response and fatigue damage.

In the following, Proper Orthogonal Decomposition (POD) is proposed as an alternative empirical procedure for riser VIV response and fatigue analysis. With POD, empirical mode shapes are estimated from the data alone and do not rely on assumed mode shapes nor on knowledge of the physical properties of the riser. POD is useful for extracting energetic spatial "modes" or patterns of variation of any physical phenomenon that is represented by a high-dimensional spatio-temporal stochastic field (such as the suite of riser strain time series from multiple sensors that we have here). The application of POD for the analysis of riser VIV response has been described by others (see, for example, Kleiven [31] or Srivilairit and Manuel [48]).

Given a suite of strain time series measured at M locations, $\mathbf{V}(t) = \{v_1(t), v_2(t), \ldots, v_M(t)\}^T$, one can establish an $M \times M$ covariance matrix, $\mathbf{C}_v$, from the strain time series, $\mathbf{V}(t)$. By solving an eigenvalue problem, one can diagonalize $\mathbf{C}_v$ so as to obtain the matrix, Λ, as follows:

$$\Phi^T \mathbf{C}_v \Phi = \Lambda; \quad \mathbf{C}_v \Phi = \Phi \Lambda \tag{3.12}$$

Solution of the eigenvalue problem yields eigenvalues, $\Lambda = diag\{\lambda_1, \lambda_2, \ldots, \lambda_M\}$ (where $\lambda_1 > \lambda_2 > \ldots > \lambda_M$), and associated eigenvectors, $\Phi = \{\phi_1, \phi_2, \ldots, \phi_M\}$.

It is possible to rewrite the original M correlated time series, $\mathbf{V}(t)$, in terms of uncorrelated scalar subprocesses, $\mathbf{U}(t) = \{u_1(t), u_2(t), \ldots, u_M(t)\}^T$, such that

$$\mathbf{V}(t) = \Phi \mathbf{U}(t) = \sum_{j=1}^{M} \phi_j u_j(t) \tag{3.13}$$

where ϕ_j represents the j^{th} POD mode shape corresponding to the j^{th} scalar subprocess, $u_j(t)$. The energy associated with $u_j(t)$ is described in terms of its variance, λ_j. A reduced-order representation of the strain time series, $\hat{\mathbf{V}}(t)$, may be obtained by including only the first N POD modes and associated generalized coordinates:

$$\hat{\mathbf{V}}(t) = \sum_{j=1}^{N} \phi_j u_j(t), \qquad N < M \tag{3.14}$$

In the present study, we employ strains measured at twenty-three locations, i.e., $M = 23$. Following the procedure as outlined above, we can thus obtain twenty-three POD mode shapes, ϕ_j, and then decompose the original twenty-three strain time series into twenty-three uncorrelated POD scalar subprocesses, $u_j(t)$, which when scaled by the POD mode shapes reconstruct all the measurements in space and time. The PSDs of the scalar subprocesses, illustrated in Fig. 3.4(a), show that a large portion (about 90%) of the energy in the strain field is carried by the first three POD modes. The first three POD

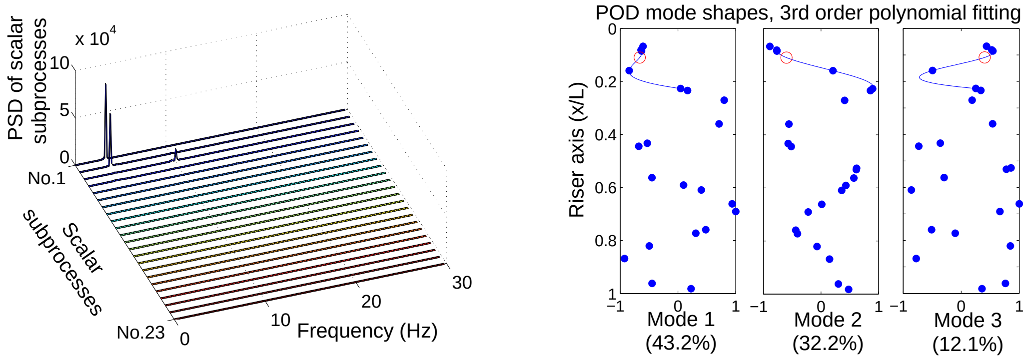

(a) (b)

Figure 3.4: The POD procedure applied with twenty-three input sensors (sensor no. 4 is the target) for the NDP2350 (sheared current) data set: (a) PSDs of the twenty-three POD scalar subprocesses; and (b) the first three POD mode shapes that carry the highest energy and a third-order interpolating polynomial to these POD modes.

mode shapes are plotted in Fig. 3.4(b), where the percentage of energy carried by each mode is also indicated. It is worth noting that for data set NDP 2350, the first several POD-based scalar subprocesses are fairly narrow-banded—i.e., they have single spectral peaks as can be seen in Fig. 3.4(a); also, the first two POD mode shapes closely resemble discrete portions of sinusoidal functions (see Fig. 3.4(b)). These observations may not hold for other data sets; POD-based scalar subprocesses are not always monochromatic time series.

As shown in Fig. 3.4(b), the POD mode shapes are only defined at the discrete points corresponding to locations of the input sensors (blue dots). If the location of interest is one where no sensor is available, such as at the location of the target sensor (red circle), POD modal coordinates for each mode must be obtained by interpolation using, for example, a third-order polynomial (blue line) fit to nearby POD modal coordinates.

Using the first thirteen POD modes which preserve 99% of the total field energy, the strain time series can be reconstructed at the location of the target sensor (strain sensor no. 4). Based on the first thirteen POD modes, the PSD for CF strain at each input logger and the summation of all these PSDs at each frequency are plotted in Figs. 3.5(a) and 3.5(b), respectively. Figure 3.5(c) shows that the reconstructed CF strain PSD (red dashed line) at the target sensor includes contributions from the first, third, and fifth harmonics, and matches the PSD based on measurements (blue solid line) reasonably well. In Fig. 3.5(d), RMS values of CF curvatures at the twenty-three input sensor locations based directly on measurements are indicated by the blue circles; at the location of the target sensor, the POD-based interpolation (indicated by the blue line which also shows estimated RMS values at other locations nearby) is very close to the RMS value (red cross) obtained from the measurements. Note that, in this case, the target sensor lies between sensor nos. 3 and 5, and strains at the target may be interpolated quite effectively with a third-order polynomial fit using strains from four nearby sensors, i.e., sensor nos. 2, 3, 5, and 6. (Other options for interpolation using more than four sensors may as well be employed; also, fits other than with a third-order polynomial may be made—our choice relies on the sensors in closest proximity to the target and makes use of collocation rather than regression.) As a result, riser response statistics, such as the RMS CF curvature, at any location within the spread of the sensors, may be estimated by such piecewise interpolation and by employing a subset of POD modes.

The fatigue damage ratio, representing the ratio of the estimated damage to that based directly on measurements at the target sensor (i.e., sensor no. 4), is 1.05, which suggests that the fatigue damage is overestimated by 5% when the POD method is employed with thirteen POD modes. Similar results for other choices of the target sensor are discussed later.

3.3.4 Modal Phase Reconstruction (MPR)

As is the case with Proper Orthogonal Decomposition, the Modal Phase Reconstruction (MPR) method has the advantage in that mode shapes need not be assumed; they can be estimated empirically from the data. Lucor et al. [36] employed MPR to analyze riser response data from CFD simulations. Mukundan [41] applied MPR to the NDP data sets to analyze the influence of traveling waves on riser response. In this study, the MPR method is employed to analyze the NDP model riser response and to estimate fatigue damage at arbitrary locations along the length of the riser. The general framework for the MPR procedure is briefly presented here.

Assume that at location, z_j, and at time instant, t_k, the riser response of interest (such as strain), i.e., $y(z_j, t_k)$, may be expressed as follows:

$$y(z_j, t_k) = Re\left\{\sum_{n=1}^{N} e^{i\omega_n t_k}\phi_n(z_j)\right\} = Re\left\{\sum_{n=1}^{N} e^{i2\pi nk/P}\left[\phi_{n,Re}(z_j) + i\phi_{n,Im}(z_j)\right]\right\} \tag{3.15}$$

where $\omega_n = 2\pi n/(P\Delta t)$ is the n^{th} circular frequency; $t_k = k\Delta t$ is the k^{th} time sample; P is the number of discrete time samples available in the record; Δt is the sampling rate; and N is the number of frequency components included in the MPR procedure. Also, $Re\{\}$ represents the real part of the indicated (complex) function. Note that $\phi_n(z_j)$ is the n^{th} complex mode shape—with real part, $\phi_{n,Re}(z_j)$, and imaginary part, $\phi_{n,Im}(z_j)$—at location, z_j, which needs

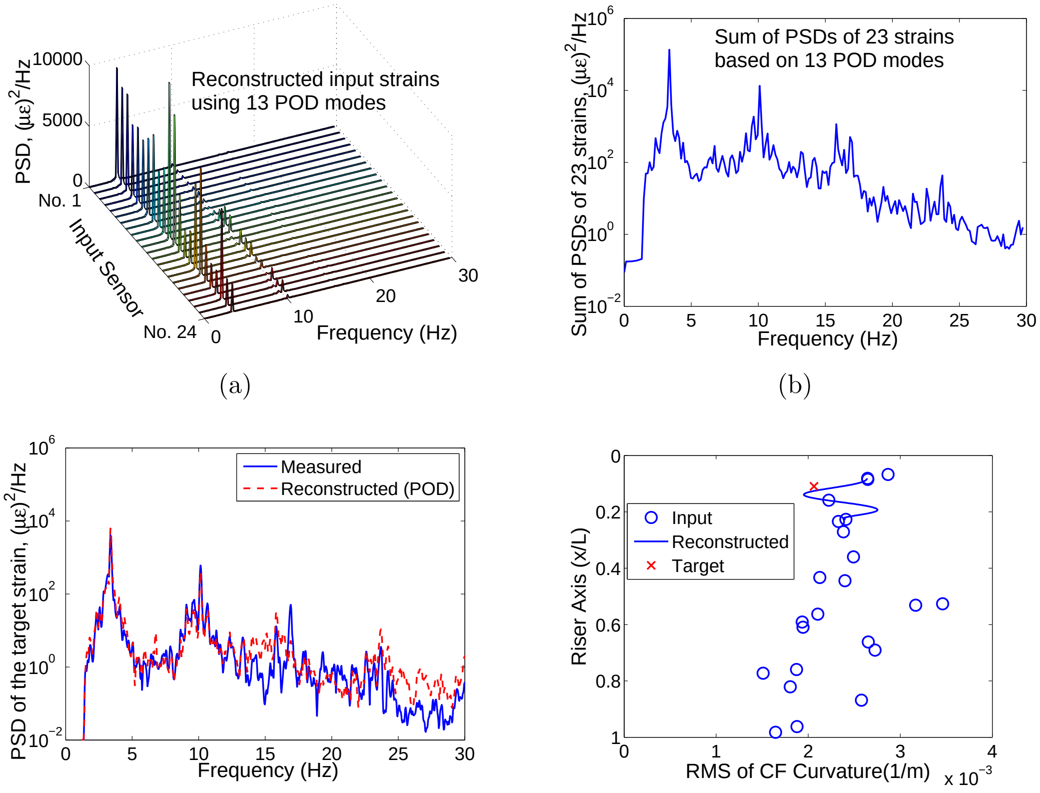

(a) (b)

(c) (d)

Figure 3.5: The POD procedure applied with twenty-three input sensors (sensor no. 4 is the target) for the NDP2350 (sheared current) data set: (a) PSDs of the strains at the twenty-three sensors reconstructed using the first thirteen POD modes; (b) summation of the strain PSDs using the first thirteen POD modes; (c) strain PSD at the target sensor: reconstructed using thirteen POD modes vs. measured; and (d) RMS curvatures: reconstructed using thirteen POD modes vs. measured.

to be empirically estimated from the data.

Equation 3.15 may be written in compact form as follows:

$$y(z_j, t_k) = Re\left\{\Delta_k \Phi_j\right\} \tag{3.16}$$

where $\Delta_k = [e^{i\omega_1 t_k}, e^{i\omega_2 t_k}, \ldots, e^{i\omega_N t_k}]$, and $\Phi_j = [\phi_1(z_j), \phi_2(z_j), \ldots, \phi_N(z_j)]^T$, where the superscript, T, refers to the transpose of a matrix.

Then at location, z_j, the riser response recorded at all P discrete time instants may be expressed as follows:

$$y(z_j) = \begin{bmatrix} y(z_j, t_1) \\ \vdots \\ y(z_j, t_k) \\ \vdots \\ y(z_j, t_P) \end{bmatrix} = Re \left\{ \begin{array}{c} \Delta_1 \Phi_j \\ \vdots \\ \Delta_k \Phi_j \\ \vdots \\ \Delta_P \Phi_j \end{array} \right\} = Re\left\{\hat{\Delta}\Phi_j\right\} \tag{3.17}$$

where $y(z_j)$ represents the entire recorded response time series at location, z_j; and $\hat{\Delta} = [\Delta_1, \ldots, \Delta_k, \ldots, \Delta_P]^T$ is easily defined, given information only on the length and the sampling rate of the record. In Eq. 3.17, it is the mode shape matrix, Φ_j, that needs to be estimated; the MPR method, thus, defines this system of P equations and $2N$ unknowns (since each $\phi_n(z_j)$ contained in Φ_j has real and imaginary parts). As long as $2N \leq P$, this system of equations can be used to solve for Φ_j in a least-squares sense. After the real part, $\phi_{n,Re}(z_j)$, and the imaginary part, $\phi_{n,Im}(z_j)$, of $\phi_n(z_j)$ are obtained, the amplitude, $|\phi_n(z_j)|$, and the phase angle, $\theta_n(z_j)$, of the measured riser response for the frequency component, ω_n, at the location, z_j, may be determined as follows:

$$|\phi_n(z_j)| = \sqrt{\phi_{n,Re}^2(z_j) + \phi_{n,Im}^2(z_j)}; \quad \theta_n(z_j) = \arctan\left(\frac{\phi_{n,Im}(z_j)}{\phi_{n,Re}(z_j)}\right) \tag{3.18}$$

The riser response at location, z_j, and at time, t_k, is readily reconstructed using a summation of N complex modes (where $N \leq P/2$) as follows:

$$y(z_j, t_k) = Re\left\{\sum_{n=1}^{N} |\phi_n(z_j)|\, e^{i(\omega_n t_k + \theta_n(z_j))}\right\} \tag{3.19}$$

From Eq. 3.19, it is clear that the phase angle, $\theta_n(z_j)$, may be used as an indicator of the wave pattern in the riser; i.e., if $\theta_n(z_j)$ varies considerably and systematically with change in the spatial coordinate, z_j, a traveling wave is likely defined by the n^{th} MPR mode; on the other hand, if $\theta_n(z_j)$ is almost unchanging with z_j, a standing wave is indicated by the n^{th} MPR mode.

As is the case with the POD method, the MPR method only yields empirically estimated mode shape coordinates at those discrete locations where the riser response is measured. If the riser response is to be predicted at a location where no sensor is present, it is necessary to interpolate the N mode shapes to the desired location and to, then, reconstruct the response there by accounting for all these N modes or frequency components. Equation 3.19, used for the reconstruction, may be rewritten as follows:

$$y(z_j, t_k) = \sum_{n=1}^{N} \left[\phi_{n,Re}(z_j)\cos(\omega_n t_k) - \phi_{n,Im}(z_j)\sin(\omega_n t_k)\right] \tag{3.20}$$

Thus, the real part, $\phi_{n,Re}$, and the imaginary part, $\phi_{n,Im}$, of the n^{th} complex mode shape, ϕ_n, may be interpolated (e.g., using a cubic polynomial along the spatial coordinate) at each time instant, t_k. Figure 3.6 shows the first two MPR mode shapes that carry the highest energy. The two horizontal axes show the real part and the imaginary part of the mode shapes; the vertical axis describes position along the riser. The discrete MPR modal coordinates

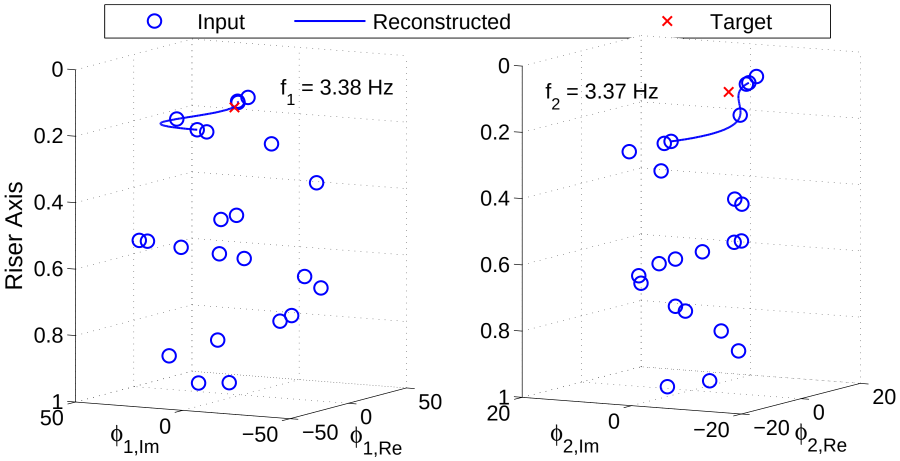

Figure 3.6: The MPR procedure applied with twenty-three input sensors (sensor no. 4 is the target) for the NDP2350 (sheared current) data set: the first two MPR mode shapes that carry the highest energy and a third-order polynomial interpolating to these MPR modes are shown.

(blue circles) appear to form a helix, which suggests that the first two modes are likely driven by traveling waves. The blue curve describes the third-order polynomial interpolated from four nearby coordinates to the target sensor. At the location of the target sensor, the interpolation yields a value for the MPR modes that is close to the value indicated by the red cross that would have been obtained using MPR directly with the measurements at the target sensor for the same frequency components. For each of the selected N MPR modes, modal coordinates at the target sensor are estimated, and strains there may be reconstructed by using Eq. 3.20.

Using the MPR procedure outlined above, the measured riser response for each separate sensor location can be decomposed into several modal components or reconstructed, mode by mode, at each time instant. This is referred to as single-location MPR. The riser response measured by a suite of sensors at several locations can also be decomposed simultaneously if we expand Eq. 3.17 by combining the measurements of all the sensors [36]. This is referred to as multi-location MPR. Given a suite of riser response measurements at M locations, where each measurement record containing P time samples is decomposed into N modes, the single-location MPR approach requires solution of the linear system of equations (Eq. 3.17) M times and, each solution requires estimation of $2N \times P$ coefficients. Multi-location MPR, on the other hand, only requires solution of one linear system of equations but the number of coefficients to be estimated is $2N \times P \times M^2$. If M is large, multi-location MPR will require far greater computational effort; here, we employ the less computationally intensive single-location MPR approach for the NDP model riser response and fatigue damage analyses.

To further speed up the computation, the measured riser strains are downsampled by a factor of 5, effectively reducing the data sampling frequency from 1,200 Hz to 240 Hz, which shrinks the number of time samples, P, in each record, to one-fifth of its original value. Additionally, instead of decomposing the measurements so as to represent all the complex modes or frequency components (from 0 Hz to the Nyquist frequency, $N = P/2$), the number of modes, N, is selected such that the frequency band from ω_1 to ω_N preserves 99% of the total energy (defined as the sum of the variance of the strains at all the loggers). Figure 3.7(a) shows CF strain PSDs for all the input sensors (except sensor no. 4) that cover the frequency band and N frequency components included in the MPR procedure. In Fig. 3.7(b), the sum of PSDs of the twenty-three input CF strains (excluding the strain at the target sensor, i.e., logger no. 4) is represented by the blue line; the selected frequency band that preserves 99% of the total energy is indicated by the red dots. By decomposing the riser strain measurements into modes only over the 99%-energy frequency band, the number of frequency components, N, is reduced to one-seventh of its original value. This greatly reduces the number of coefficients to be determined in the MPR linear system solution and, hence, dramatically saves computational time. Figure 3.7(c) shows that the energy distribution by frequency of the reconstructed CF strains at the target sensor (red dashed line) matches that based on the measured strains there (blue solid line) reasonably well over the 99%-energy frequency band. In Fig. 3.7(d), RMS values of CF curvature at the twenty-three input sensor locations based directly on measurements are indicated by the blue circles; at the location of the target sensor, the MPR-based interpolation (indicated by the blue line, which also shows estimated RMS values at other locations nearby) is very close to the RMS value (red cross) obtained from the measurements. The strains at the target sensor (sensor no. 4) are interpolated quite effectively with a third-order polynomial fit using strains from four nearby sensors, i.e., sensor nos. 2, 3, 5, and 6 (again, other fits are also possible). As is the case with the POD procedure, riser response statistics, such as the RMS CF curvature, at any location within the spread of the sensors, may be estimated by such piecewise interpolation following application of the MPR procedure.

The fatigue damage ratio, representing the ratio of the estimated damage to that based directly on measurements at the target sensor (i.e., sensor no. 4), is 1.25, which suggests that the fatigue damage is overestimated by 25% when the MPR method is employed with the selected frequency components. Similar results for other choices of the target sensor are discussed later.

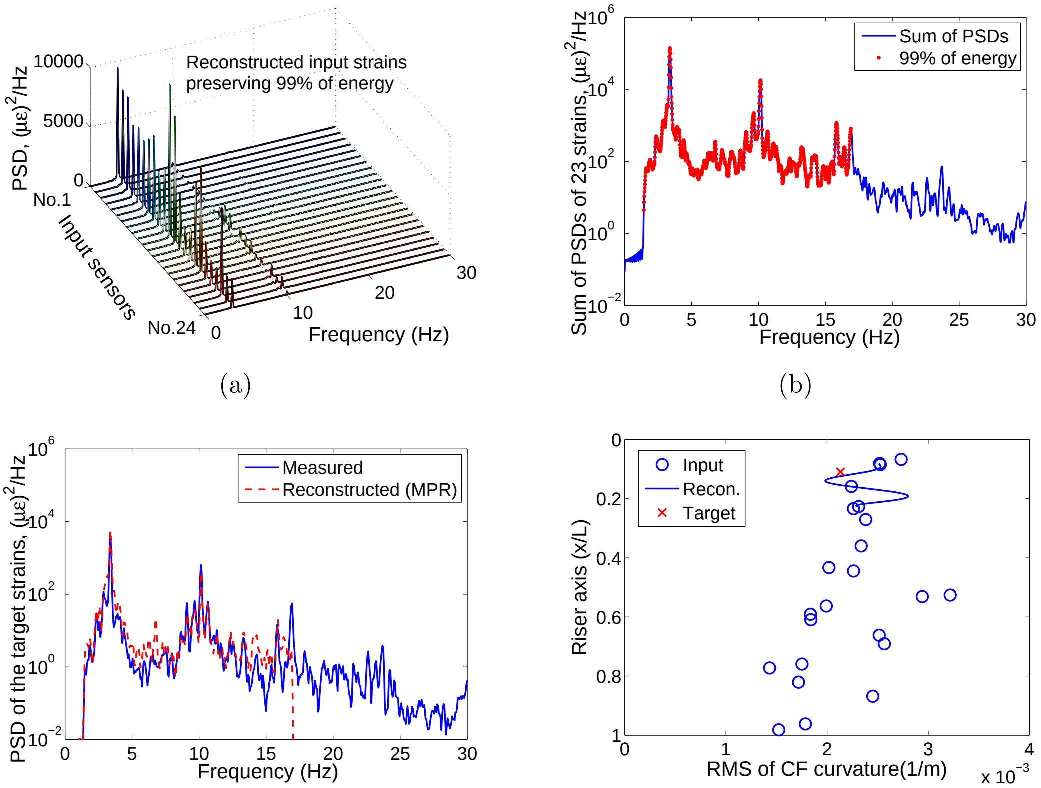

(a) (b) (c) (d)

Figure 3.7: The MPR procedure applied with twenty-three input sensors (sensor no. 4 is the target) for the NDP2350 (sheared current) data set: (a) PSDs of the strains at the twenty-three sensors reconstructed using modes in a frequency band that preserves 99% of the energy; (b) summation of the strain PSDs using modes that preserve 99% energy; (c) strain PSD at the target sensor: reconstructed (using modes that preserve 99% energy) vs. measured; and (d) RMS curvatures: reconstructed (using modes that preserve 99% energy) vs. measured.

3.3.5 Hybrid Method: MPR + Modified WWA

By studying Eq. 3.20, it may be noted that the MPR method decomposes the measured riser response into N components and, importantly, each component is a single-frequency time series. This suggests that the each single-frequency component may be decomposed further by using the previously discussed modified WWA method. We will refer to this approach as the "hybrid" method since it combines the MPR and the modified WWA methods. The hybrid method has advantages when compared with either the MPR or the modified WWA methods. First, unlike the MPR method, the hybrid method does not require interpolation from discrete complex modes to estimate or reconstruct the response at any arbitrary location; it has the ability to reconstruct the riser response over the entire length of the riser (as a continuous function) despite starting from only a discrete set of measurements. Second, the modified WWA method seeks to represent several frequency components of a wide banded (multi-frequency) response time series with the help of measurements from available sensors; on the other hand, the hybrid method seeks to decompose each MPR mode (associated with a single-frequency time series) based on the same number of sensors.

The procedure for application of the hybrid method is presented here. First, the MPR approach is followed and the various input strains are represented as in Eq. 3.20. Then, at the location of each input sensor, z_j, the real part of the n^{th} MPR mode, $\phi_{n,Re}(z_j)$, may be decomposed using the modified WWA procedure as follows:

$$\begin{aligned} \phi_{n,Re}(z_j) &= \sum_{k=1}^{s} \left[a_k \varphi_k(z_j) + b_k \psi_k(z_j) \right] \\ \varphi_k(z_j) &= \sin\left(\frac{n_k \pi z_j}{L}\right); \quad \psi_k(z_j) = \cos\left(\frac{n_k \pi z_j}{L}\right) \end{aligned} \tag{3.21}$$

The real part of the n^{th} MPR mode at locations of all M sensors may be expressed in a matrix form (as in Eq. 3.5), i.e., $\mathbf{Aw} = \mathbf{d}$. Thus, we have:

$$\mathbf{A} = \begin{bmatrix} \varphi_1^1 & \psi_1^1 & \varphi_2^1 & \psi_2^1 & \cdots & \varphi_s^1 & \psi_s^1 \\ \varphi_1^2 & \psi_1^2 & \varphi_2^2 & \psi_2^2 & \cdots & \varphi_s^2 & \psi_s^2 \\ \vdots & \vdots & \vdots & \vdots & \vdots & \vdots & \vdots \\ \varphi_1^M & \psi_1^M & \varphi_2^M & \psi_2^M & \cdots & \varphi_s^M & \psi_s^M \end{bmatrix}; \mathbf{w} = \begin{bmatrix} a_1 \\ b_1 \\ a_2 \\ b_2 \\ \vdots \\ a_s \\ b_s \end{bmatrix}; \mathbf{d} = \begin{bmatrix} \phi_{n,Re}(z_1) \\ \phi_{n,Re}(z_2) \\ \vdots \\ \phi_{n,Re}(z_M) \end{bmatrix} \tag{3.22}$$

As long as $2s \leq M$, the modal weights, $\mathbf{w}$, may be estimated in a least-squares sense, and a spatially continuous function, $\phi_{n,Re}(z)$, can be derived. Note that exactly the same procedure may be repeated to decompose the imaginary part of the n^{th} MPR mode, i.e., for $\phi_{n,Im}$. By repeating this procedure for all the real and imaginary MPR modes, the riser response over the entire riser can be reconstructed as a continuous function by this hybrid method. In the present study, where $M = 23$, we use s equal to 6; the modes in the modified WWA portion of the hybrid method are selected to correspond to frequencies closest to the MPR mode that is being reconstructed according to Eq. 3.21.

Analogous to Fig. 3.6 for the MPR procedure, Fig. 3.8 shows the first two MPR mode shapes that carry the highest energy reconstructed using the modified WWA method.

An example using the hybrid method with strain sensor no. 4 as the target sensor is presented in Fig. 3.9, which may be compared directly with Fig. 3.7 based on the MPR procedure.

The fatigue damage ratio, representing the ratio of the estimated damage to that based directly on measurements at the target sensor (i.e., sensor no. 4), is 1.84, which suggests that the fatigue damage is overestimated by

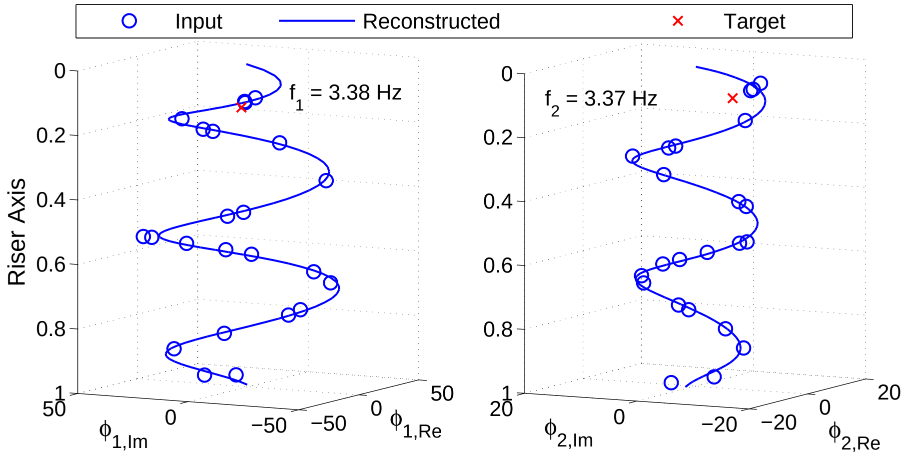

Figure 3.8: The hybrid (MPR + modified WWA) procedure applied with twenty-three input sensors (sensor no. 4 is the target) for the NDP2350 (sheared current) data set: the first two MPR mode shapes that carry the highest energy and modified WWA based continuous functions fit to these MPR modes are shown.

84% when the hybrid (MPR + modified WWA) method is employed with the selected frequency components. Similar results for other choices of the target sensor are discussed later.

3.4 Fatigue Damage Estimation Based on A Large Number of Sensors

The CF strains on the NDP model riser were measured using twenty-four sensors (only twenty-three sensors were available for the data set, NDP 2420, since strain sensor no. 21 had failed). In the results described here, we select one sensor at a time as the target sensor, and use measurements from the remaining twenty-three sensors (or twenty-two for NDP 2420) to reconstruct strains at the location of the target sensor by employing the various

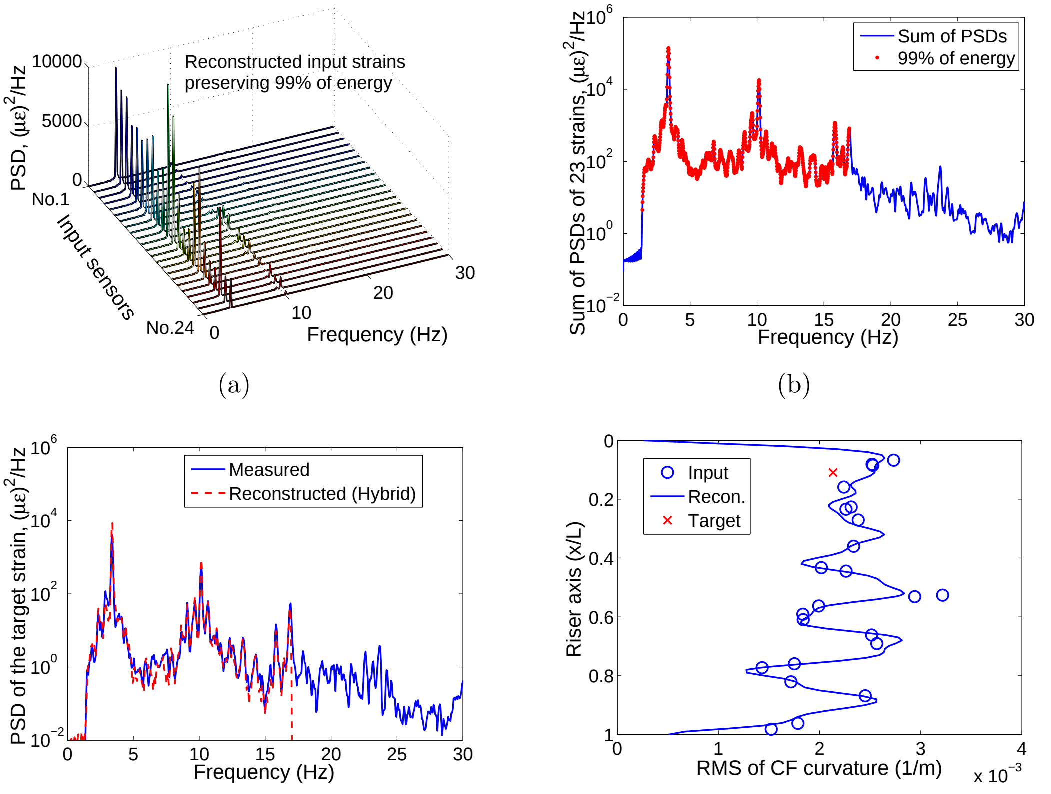

(a)

(b)

(c)

(d)

Figure 3.9: The hybrid (MPR + modified WWA) procedure applied with twenty-three input sensors (sensor no. 4 is the target) for the NDP2350 (sheared current) data set: (a) PSDs of the strains at the twenty-three sensors reconstructed using modes in a frequency band that preserves 99% of the energy; (b) summation of the strain PSDs using modes that preserve 99% energy; (c) strain PSD at the target sensor: reconstructed (using modes that preserve 99% energy) vs. measured; and (d) RMS curvatures: reconstructed (using modes that preserve 99% energy) vs. measured.

empirical methods described above. We presented such analyses where each empirical method was applied with sensor no. 4 as the target sensor. The damage ratio, which represents the ratio of the fatigue damage rate based on the reconstructed strain (at the target sensor) to that based directly on the measured strain there, is used as a criterion to compare the empirical methods. Figure 3.10 presents damage ratios estimated at the twenty-four locations for the two uniform current data sets (red color) and the two sheared current data sets (blue color), by employing each of the five empirical methods. The lowest and the highest values of the damage ratios estimated for each data set, and for each empirical method, are also indicated in the figure legends—for example, Fig. 3.10(a) states that the twenty-four damage ratios estimated by the WWA method for the uniform current data set, NDP 2120, ranged from 0.25 to 6.58.

Some general conclusions, that may be drawn by studying Fig. 3.10, are summarized here.

(i) With the WWA method, a large number of modes can be interpreted from a suite of measurements. The modified WWA method can better account for the effects of traveling waves and localized curvature changes but fewer modes can be interpreted or used in reconstruction of strains at any target location. As a consequence, in the present study where a large number of sensors (twenty-three) are available, fatigue damage rates estimated over the entire riser length by the WWA and the modified WWA methods are generally of comparable accuracy (see Figs. 3.10(a) and 3.10(b)).

(ii) Fatigue damage rates estimated by the POD and MPR methods are quite similar since both methods are affected by the quality of the unavoidable interpolation—it may be noted that the presence of a sensor close to the target location leads to good estimation of damage; however, when a nearby sensor is not present, as is the case for sensor nos. 9 and 22 indicated by the red ellipses in Figs. 3.10(c) and 3.10(d), fatigue damage rate estimates are less accurate.

(iii) The fatigue damage rates for the two uniform current data sets estimated by either the POD or the MPR methods are less accurate than those estimated by the WWA or the modified WWA methods; one likely reason for this is due to the strong non-stationary response characteristics indicated particularly in the two uniform current data sets (see Chapter 2) that more directly affect the accuracy of the POD and the MPR methods. With the WWA and the modified WWA methods, the modal weights are solved for at each time instant (see Eq. 3.7); the POD and the MPR methods, on the other hand, assume that the riser response is described by a stationary process and decomposition of the measured response is based on the entire record (see Eqs. 3.12 and 3.17). To reduce the influence of the non-stationary characteristics of the measured response on fatigue damage estimations, one possible approach is to divide the recorded response time series into shorter segments and then to employ the POD or MPR methods on the shorter segments.

(iv) Generally, when a large number of sensors are available, as is the case with the NDP model riser, all the five empirical methods estimate fatigue damage rates over the entire riser length quite well—damage ratios are typically in the range, 0.3 to 3.0, with lowest and highest estimations of 0.16 and 14.54, respectively. Among the five methods, the hybrid method (Fig. 3.10(e)) which combines the MPR and the modified WWA procedures, appears to be the most accurate for fatigue damage estimation with the four selected NDP riser data sets.

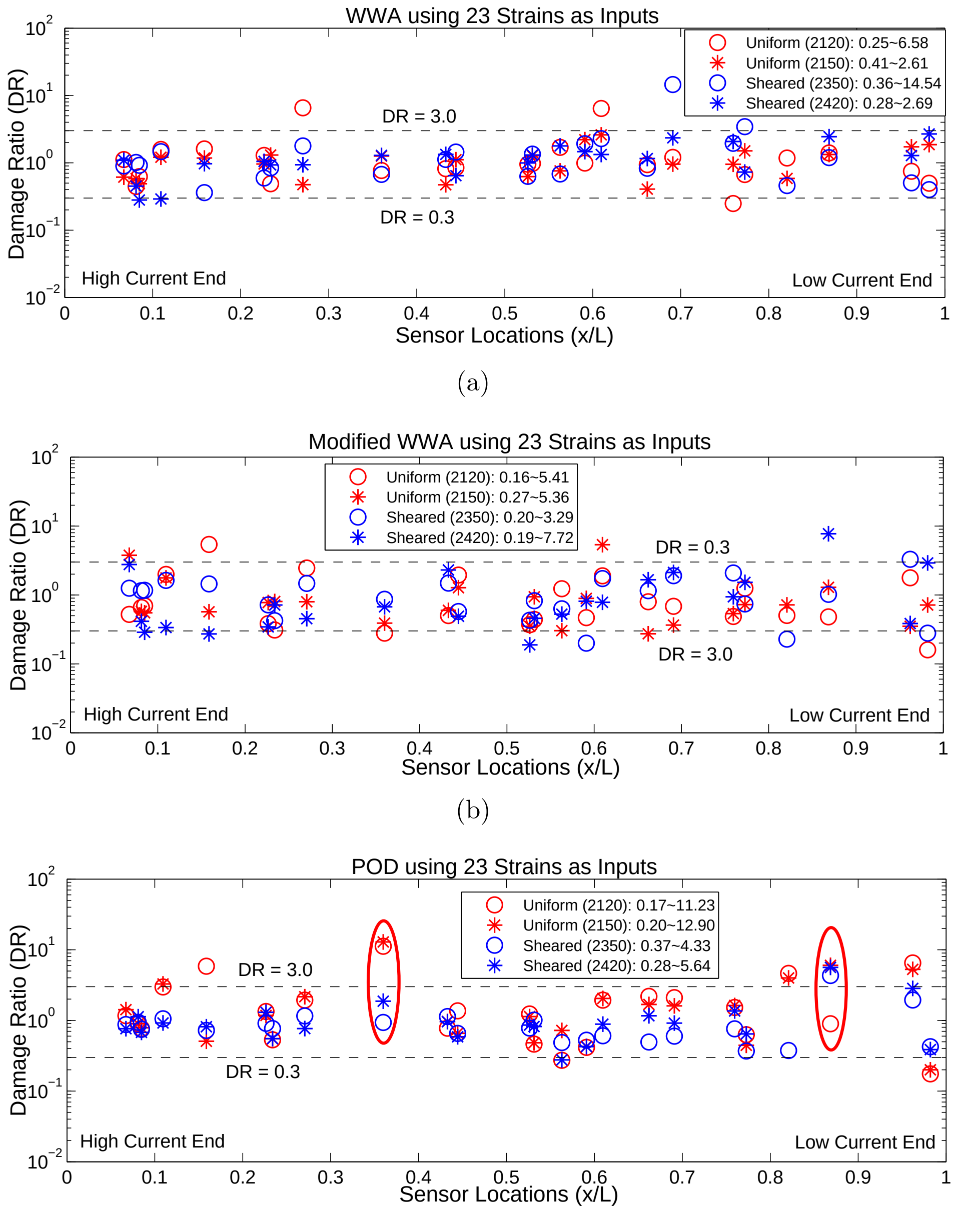
WWA using 23 Strains as Inputs
Uniform (2120): 0.25~6.58
Uniform (2150): 0.41~2.61
Sheared (2350): 0.36~14.54
Sheared (2420): 0.28~2.69
DR = 3.0
DR = 0.3
High Current End
Low Current End
Damage Ratio (DR)
10^2
10^1
10^0
10^{-1}
10^{-2}
0
0.1
0.2
0.3
0.4
0.5
0.6
0.7
0.8
0.9
1
Sensor Locations (x/L)
Modified WWA using 23 Strains as Inputs
Uniform (2120): 0.16~5.41
Uniform (2150): 0.27~5.36
Sheared (2350): 0.20~3.29
Sheared (2420): 0.19~7.72
DR = 0.3
DR = 3.0
High Current End
Low Current End
Damage Ratio (DR)
Sensor Locations (x/L)
POD using 23 Strains as Inputs
Uniform (2120): 0.17~11.23
Uniform (2150): 0.20~12.90
Sheared (2350): 0.37~4.33
Sheared (2420): 0.28~5.64
DR = 3.0
DR = 0.3
High Current End
Low Current End
Damage Ratio (DR)
Sensor Locations (x/L)

(a)

(b)

(c)

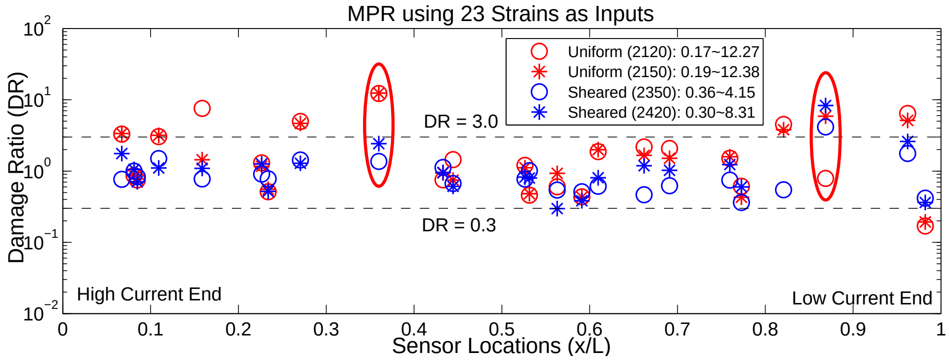

(d)

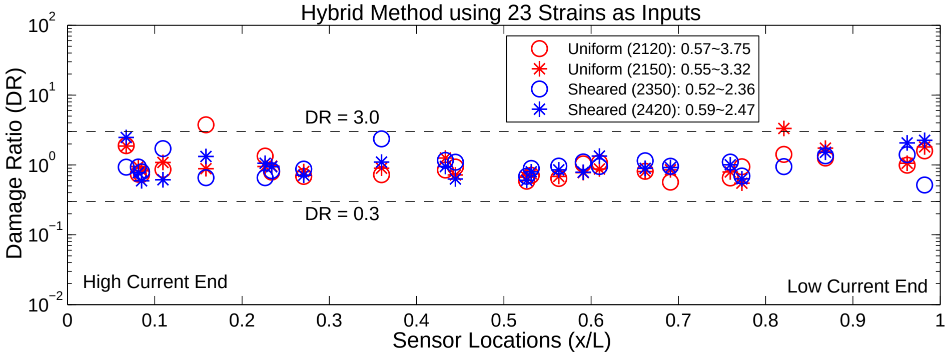

(e)

Figure 3.10: Fatigue damage ratios estimated by different empirical procedures at various locations along the span of the NDP model riser based on strains measured by twenty-three sensors: (a) WWA; (b) modified WWA; (c) POD; (d) MPR; and (e) Hybrid: MPR + modified WWA.

3.5 Fatigue Damage Estimation Based on A Small Number of Sensors

We have discussed estimation of fatigue damage rates over the entire length of the NDP model riser based on measurements from a large number of sensors. However, actual deepwater drilling risers are seldom instrumented as densely as the NDP model riser due to the high cost of sensor deployment, maintenance, data retrieval, etc. Accordingly, we now discuss estimation of fatigue damage rates over the riser length based on measurements from a much smaller number of sensors than before. Using strain measurements from eight sensors as inputs, the riser response is reconstructed at the locations of all of the twenty-four sensors (including the eight input sensors). By iterating over numerous different combinations of eight strain sensors as inputs (from among all the twenty-four available sensors on the riser), optimal locations for the eight sensors along the riser are identified by cross-validation, whereby estimated strains and fatigue damage rates at the twenty-four locations are compared with strains and fatigue damage rates based on the actual recorded measurements there.

In principle, we could select all the possible combinations of eight sensors chosen from among twenty-four available; however, this results in an exceedingly large number of combinations to be evaluated. We choose to evaluate only thirty-four arrangements or combinations of eight sensors. Figure 3.11 shows the locations of the eight sensors for the thirty-four selected combinations. The first group (identified as G1) comprises sixteen combinations, each of which includes eight contiguous sensors; the second group (G2) has six combinations wherein six sensors are located near the top end (i.e., the higher current end in the case of the sheared current data sets) and the remaining two sensors are near the middle, at a location around one-fourth of the riser's length from the bottom (low current) end, or at the bottom end. Other groups representing different sensor arrangements are also indicated in Fig. 3.11. Note that a malfunctioning strain sensor (no. 21) is not selected as an input sensor in these studies.

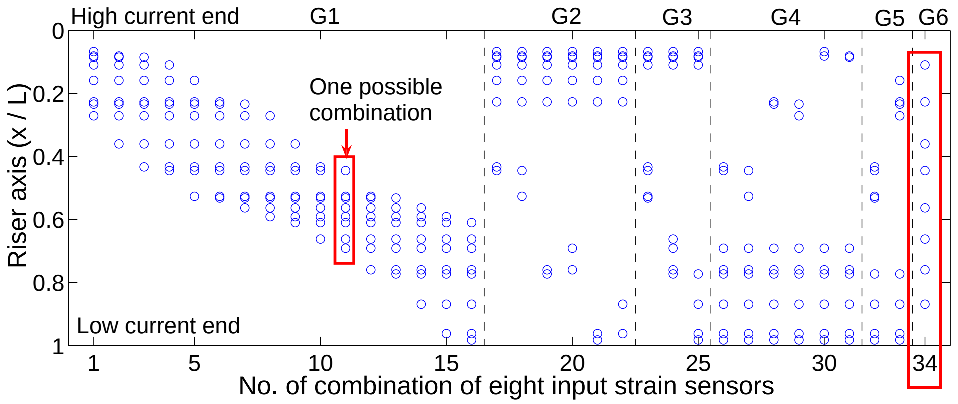

Figure 3.11: Thirty-four combinations of eight input strain sensors chosen for fatigue damage analysis studies using cross-validation against measurements.

Not all of the five empirical methods discussed earlier are employed in the study that uses eight strain sensors to estimate fatigue damages; there are reasons for this. First, for the modified WWA method, only two or three modes could be represented if eight sensors are available; this would make it difficult to account for all the important frequencies (the first and higher harmonics) of the riser response. Second, for the POD and MPR methods, the accuracy of the interpolation (from information at the discrete locations of the input sensors to all other locations) controls the accuracy of the reconstructed riser response at target locations without sensors. If the target location has no available loggers nearby or if it is spatially outside the range of the suite of input sensors, the reconstructed riser response will be inaccurate. Given these limitations, the modified WWA, POD, and MPR methods are not employed in this study with eight input sensors; only the WWA and the hybrid methods are employed to estimate fatigue damage rates at the twenty-four locations along the NDP model risers using measurements from eight sensors.

For illustration purposes, the NDP2350 (sheared current) data set, with sensors arranged in combination No. 34 (see Fig. 3.11) is chosen to discuss the estimation of the fatigue damage rate using the WWA method and measurements from the eight strain sensors. The reason for choosing combination No. 34 is because it is proved to be one of the best combinations for accurate fatigue predictions with all the four NDP data sets. Fatigue damage rates estimated from eight strain measures for all the 34 considered combinations using the WWA and the hybrid methods are presented later.

Analogous to the figures used to illustrate the application of the five empirical methods with 23 input sensors, Fig. 3.12 shows results of the WWA application with 8 input strain senors. The PSD for CF strains at the eight input loggers and the summation of all these PSDs at each frequency are plotted in Figs. 3.12(a) and 3.12(b), respectively. The six modes, selected in a similar manner to the procedure used for the WWA method with 23 sensors, include the first, second, third, fourth, and fifth harmonics of the input signals. In Fig. 3.12(c), the reconstructed RMS values of the CF curvature are compared with the measured values at the twenty-four sensor locations indicated by red asterisks; among them, the locations of the eight input sensors are indicated by blue circles. In Fig. 3.12(d), the reconstructed RMS values of the CF displacement (normalized by the cylinder diameter, D) are compared with the measured values at the eight locations where accelerations are measured (these are the same eight locations of the eight input strain sensors). Results show that the RMS values of both the reconstructed curvatures and the reconstructed displacements match the measured values at the discrete locations quite well.

Damage ratio (DR) estimates at the 24 strain sensor locations using the WWA method with the eight strain input sensors in combination No. 34 for the NDP2350 (sheared current) data set are shown in Fig. 3.13; these DR estimates are seen to vary from 0.22 to 3.41. Comparing Figs. 3.13 and 3.10(a), it is interesting to note that the accuracy of the fatigue damage rates estimated using 8 sensors is not worse than that estimated using 23 sensors for this data set (NDP2350).

The base-10 logarithms of the 24 DR estimates from the WWA method based on eight sensors in each of the thirty-four combinations are presented as box-and-whisker plots in Figs. 3.14(a) and 3.14(b), which summarize results for the two uniform current data sets and the two sheared current data sets, respectively. In each box-and-whisker plot, the central mark and the edges of the box represent the median, the 25th percentile, and the 75th percentile of the data; the upper and lower whiskers extend out to the minimum and the maximum values. A shorter box indicates low variability or greater precision in the estimation of the damage ratio; vertically, the closer a bar is to unity, the more accurate is the associated estimation. Preferred combinations that ensure precise and accurate estimation of the fatigue damage rate for all the four data sets are indicated by green arrows. When employing the WWA method, the use of eight sensors distributed over a greater portion of the riser, e.g., placing four sensors near one end and four sensors near the other end, such as in Combinations nos. 25 and 33, generally results in more accurate and precise fatigue damage estimation than does the use of eight clustered sensors such as in Combination nos. 1 to 16.

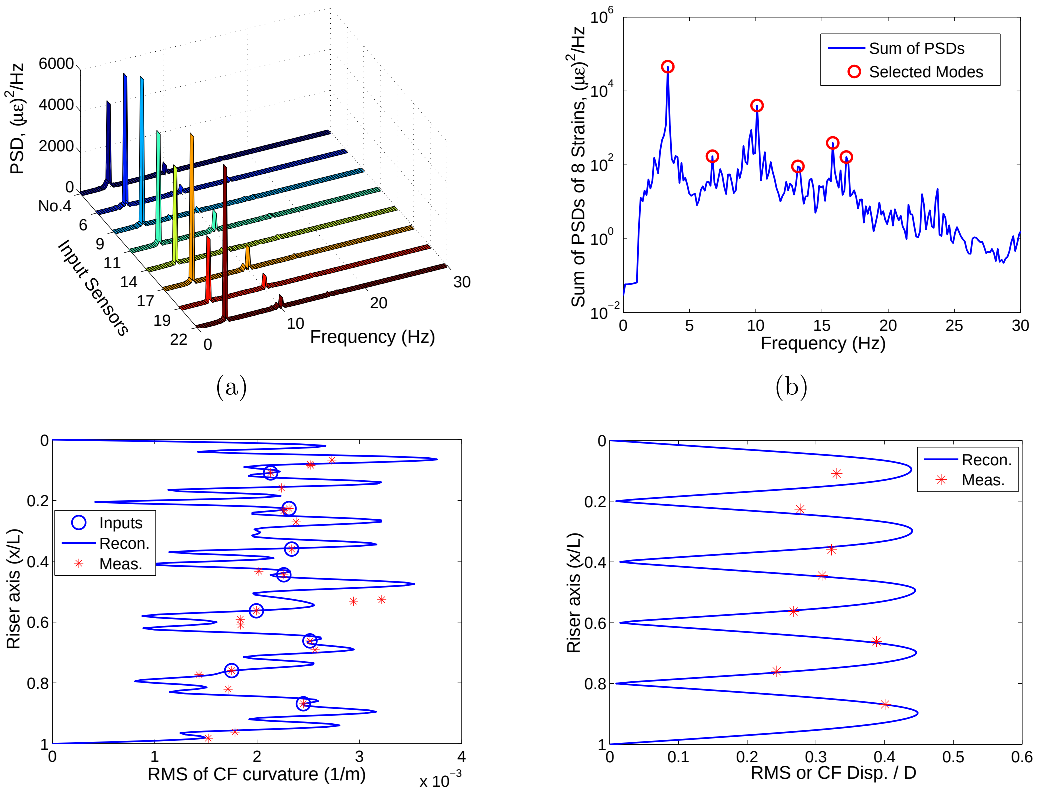

(a) (b)

(c) (d)

Figure 3.12: The WWA procedure applied with the eight strain sensors of Combination No. 34 for the NDP2350 (sheared current) data set: (a) PSDs of the strains measured at the eight sensors; (b) summation of the PSDs and identification of the selected modes; (c) RMS curvatures: reconstructed vs. measured; and (d) RMS displacements: reconstructed vs. measured.

Fatigue damage ratios estimated by the hybrid method based on eight sensors (using four modes) in each of the thirty-four combinations are illustrated by box-and-whisker plots in Figs. 3.15(a) and 3.15(b), which summarize results for the two uniform current data sets and the two sheared current data sets, respectively. Direct comparison with the results based on the WWA method (see Fig. 3.14) suggest that among the thirty-four combinations, those

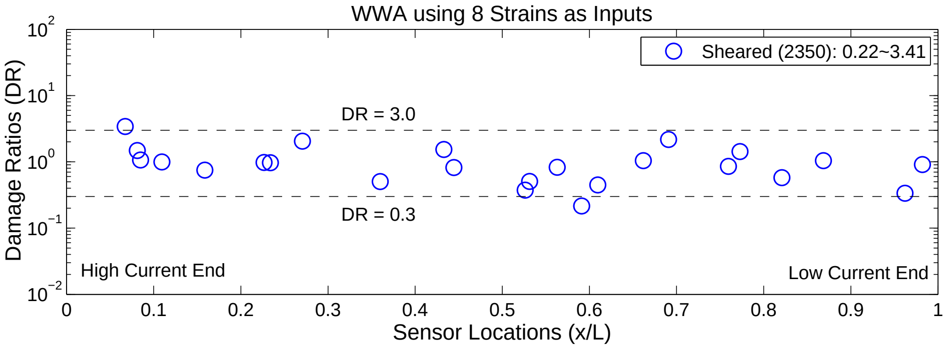

Figure 3.13: Damage ratios estimated at various locations using the WWA procedure with the eight sensors of Combination No. 34 for the NDP2350 (sheared current) data set.

that were identified as more precise and accurate based on the WWA method are also found to be so with the hybrid method. For all the thirty-four combinations, the hybrid method appears to provide more accurate and precise estimation of fatigue damage rates than the WWA method.

3.6 Sensor Location and Spatial Aliasing

Efficient sensor location and possible spatial aliasing errors associated with riser sensor arrays are conveniently studied by examining the $N \times N$ orthogonality matrix, $\mathbf{R}$, defined in terms of N riser modes of interest [10]—i.e., $\mathbf{R}_{i,j} = |\varphi_i^T \varphi_j|$ $(i, j = 1, \ldots, N)$ where, for example, if sinusoidal mode shapes are assumed, $\varphi_i = [sin(n_i \pi z_1/L), sin(n_i \pi z_2/L), \ldots sin(n_i \pi z_M/L)]$ when M loggers are employed on a riser of length, L. For an array of sensors that avoids aliasing errors, off-diagonal terms of $\mathbf{R}$ are relatively small (the diagonal terms are less important but are generally close to unity). Figure 3.16(a) shows off-diagonal terms of the orthogonality matrix computed for the twelve

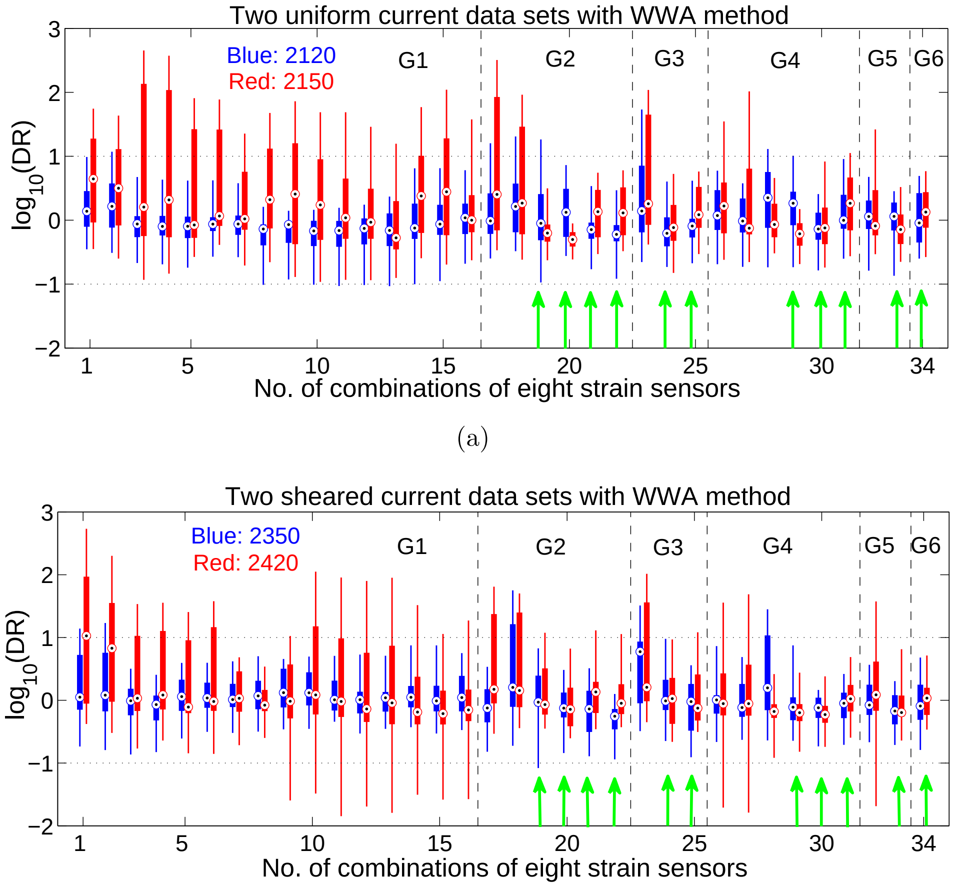

(a)

(b)

Figure 3.14: Fatigue damage ratios estimated by use of the WWA method with measurements based on thirty-four combinations involving eight strain sensors (combinations that provide relatively better fatigue estimations are indicated by green arrows): (a) two uniform current data sets; and (b) two sheared current data sets.

modes used with the WWA method with twenty-three sensors (where sensor no. 4 is the target) for the sheared current data set, NDP2350. Figure 3.16(b) is a similar plot where eight sensors (associated with Combination no. 34) are used and only six modes are employed with the WWA method and the same data set. The relatively low values of the off-diagonal elements of **R** in

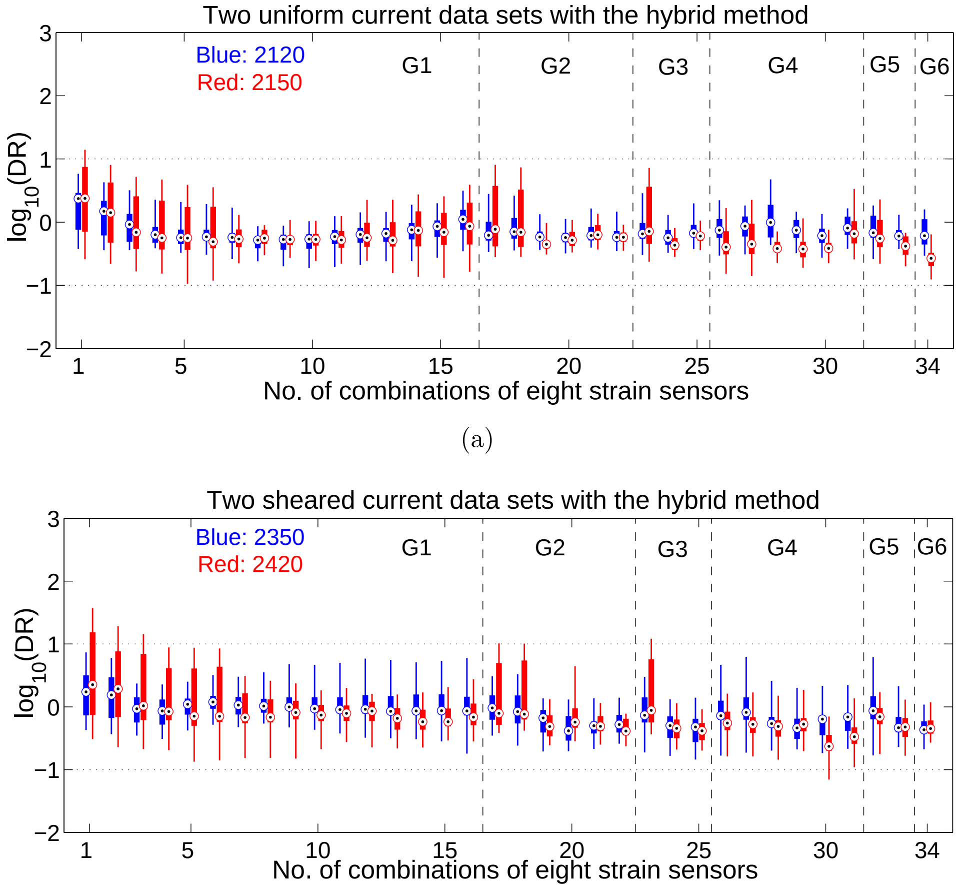

(a)

(b)

Figure 3.15: Fatigue damage ratios estimated by use of the hybrid method with measurements based on thirty-four combinations involving eight strain sensors: (a) two uniform current data sets; and (b) two sheared current data sets.

the figures confirms that spatial aliasing is not of great concern in the choice of sensor locations employed in the various WWA method results presented. Note that the orthogonality matrix, $\mathbf{R}$, for the modified WWA method can be constructed in a similar manner as for the WWA method.

The spatial distribution of the loggers may, in general, also be of con-

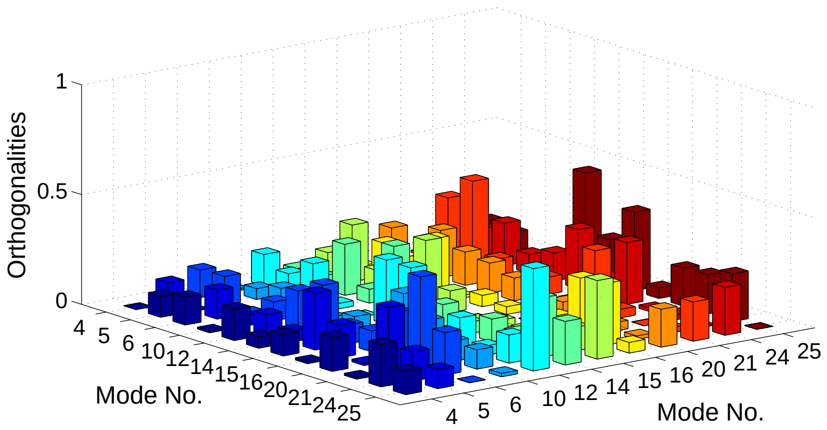

(a)

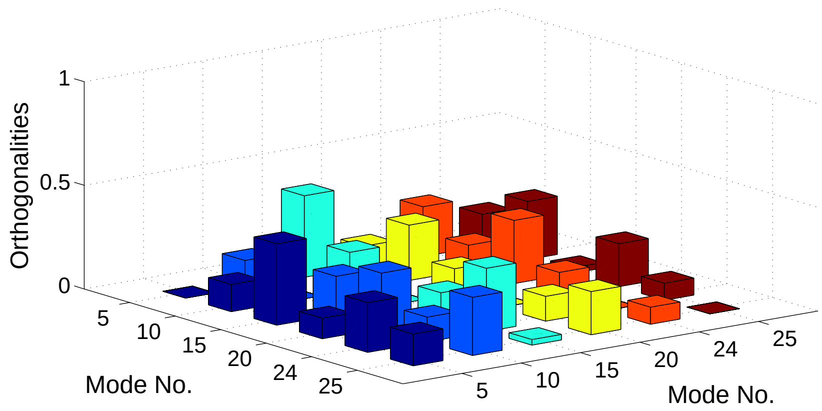

(b)

Figure 3.16: Values of the off-diagonal elements of orthogonality matrices, **R**, computed with assumed sinusoidal mode shapes for the sheared current (NDP2350) data set: (a) twenty-three sensors and twelve WWA modes used (sensor no. 4 is the target); and (b) eight sensors of Combination no. 34 and six WWA modes used.

cern when the POD or MPR methods are employed. This is not so much a spatial aliasing issue; rather, these two methods rely on interpolation from discrete sensor locations (based on relevant POD or MPR modes) to any target location while reconstructing strains there. If the target location is spaced very far from the closest sensors used in the interpolation, reconstructed strains can be quite inaccurate. Even if higher modes are well represented in the POD or MPR modes derived, because these modes are discrete, poor interpolation will lead to spurious understanding of the higher harmonics at the target location since these are necessarily associated with smaller wave lengths; thus, interpolation ad response reconstruction will be inaccurate when sensor distribution is sparse.

3.7 Discussion and Conclusions

In this study, four data sets comprising strains measured on the NDP model riser subjected to uniform and sheared currents were employed to test empirical fatigue damage estimation methods. Five empirical methods were studied—they include Weighted Waveform Analysis (WWA), modified WWA, Proper Orthogonal Decomposition (POD), Modal Phase Decomposition (MPR), and a hybrid method that combines MPR and modified WWA. For each method, the theoretical formulation was first presented and, then, its application was illustrated by an example wherein a single sensor was selected as the target sensor and by using measurements from the remaining twenty-three sensors as inputs, the riser response was reconstructed at the location of the target sensor. The fatigue damage rate estimated using the reconstructed riser response was compared with that based directly on measurements at that target sensor location. The ratio between the estimated fatigue damage rate and that based on measurements there was used as an indicator of the accuracy of the empirical method. Two separate summary studies—one involving a larger number of available sensors on the riser (twenty-three) and another involving a small number (eight)—were carried out and estimated fatigue damage rates over the entire length of the NDP model riser were computed and the results discussed.

Based on the numerical studies presented, a few concluding remarks follow:

(i) With careful selection of the riser modes for inclusion, the WWA method has the ability to preserve higher harmonics in the reconstructed riser response since the selected modes in the method are non-sequential. Because the modal weights are solved for at each time instant, non-stationary characteristics, if present, are inherently preserved in response reconstruction with this method. The WWA method works particularly well if only a small number of sensors are available; the method relies on assumed mode shapes that are based on knowledge of the physical properties of the riser. Computation with the WWA method is fast.

(ii) The modified WWA method can account for the influence of higher harmonics as long as a large number of sensors is available. This method is more versatile in accounting for the effect of traveling waves than the WWA method. As with the WWA method, the modified WWA method also directly accounts for non-stationary characteristics; however, it is not well-suited for cases where only a small number of sensors is available since a greater number of modal weights need to be estimated than with WWA. The modified WWA method relies on assumed mode shapes and the computation is fast.

(iii) The POD method preserves frequency components and higher harmonics in the reconstructed riser response by empirical decomposition of the spatio-temporal data. This is evident from the power spectra as well as curvature plots that reveal high-frequency energy and large curvatures (or small wavelengths), respectively. POD relies only on data; the method identifies empirical mode shapes directly from the data, without the need for any physical properties of the riser. The POD scheme is the fastest among the five methods; however, it does not account for non-stationary response characteristics. The method is not well-suited to situations where only a small number of sensors is available because of inaccuracies in the reconstructed response that arise due to the need for interpolation or extrapolation.

(iv) As is the case for the POD method, the MPR method accounts for higher harmonics in the response and only relies on data, not on physical properties of the riser to estimate complex riser modes. MPR, however, is not well-suited for situations where the riser response exhibits strong non-stationary characteristics or when only a small number of sensors are available. Computation with the MPR method is slow. Importantly, MPR explicitly accounts for traveling waves in decomposing the measured response.

(v) The hybrid method (which combines the MPR and modified WWA methods) has the ability to account for higher harmonics and the effect of traveling waves; it also works well even if only a small number of sensors is available. The hybrid method does not explicitly take into consideration non-stationary characteristics, but the reconstruction even with fairly strong non-stationary response is superior to that with the POD and MPR methods. The hybrid method needs to assume modes in the second step of estimating modal weights for the derived complex MPR modes. Although the hybrid method is the slowest due to the greater computational effort relative to the other methods, it is the most accurate both for a large as well as a small number of input sensors.

It is important to briefly discuss the limitations of the present study. First, the results presented are based on only four data sets obtained from a model riser. Uncertainty in fatigue damage estimates from each empirical method is not directly discussed. Second, issues related to what constitutes an adequate sample in terms of length (duration) of the measured signal and sampling rate when employing each empirical method for reconstruction of strain and estimation of fatigue damage rates have not been directly addressed. Third, only strain measurements are used in the fatigue damage rate estimation; no acceleration measurements have been used. Fourth, the WWA method and the modified WWA method need information on riser physical properties and on the added mass coefficient for computing natural frequencies of the riser; this may hinder application of these methods because such information is not always available. Some of these limitations are addressed in the following chapters.

In closing, we have shown that the various empirical methods presented can all be used to estimate fatigue damage rates for a riser, given response measurements obtained from a limited number of sensors. After "short-term" fatigue damage distributions conditional on specific current profiles are obtained using such empirical methods, it is possible next to estimate the "long-term" fatigue damage of risers by integrating the short-term fatigue damage distributions with the likelihood of different current profiles. This is the focus of Chapter 5 where we discuss the use of field measurements on deepwater drilling risers to complement analytical tools to estimate fatigue damage and lifetime of risers.

Chapter 4

A Data-Driven Mode Identification Algorithm for Fatigue Damage Assessment

4.1 Introduction

Fatigue damage associated with sustained VIV poses significant challenges in the design of marine risers especially in deep waters. To improve understanding of the VIV phenomenon and associated fatigue damage, it is becoming increasingly common to measure riser response, in the form of strains or accelerations, at discrete points along the riser length in full-scale field monitoring campaigns or in experiments. Accurate response reconstruction over the entire riser length using measurements at those discrete locations is needed to allow fatigue damage prediction of the riser. Such accurate riser response reconstruction can also serve as a benchmark for validating analytical riser fatigue damage prediction software. This motivates our need to seek empirical methods for riser response reconstruction.

In Chapter 3, several empirical methods were demonstrated to have the ability to reconstruct riser response quite effectively from a limited array of strain measurements. Methods such as Proper Orthogonal Decomposition (POD) do not require any assumptions or information of the riser's physical properties; Weighted Waveform Analysis (WWA), on the other hand, relies on estimation of the natural frequencies of the riser. This estimation is possible if the physical properties of the riser, such as its mass and bending stiffness, as well as hydrodynamic parameters, such as the added mass coefficient, are known. Among these, the added mass coefficient is one of the most complex and least understood hydrodynamic parameters that influence the VIV response of a riser. The requirement of knowledge of the riser physical and hydrodynamic properties limits the attractiveness of the empirical WWA method to some degree.

In order to address this issue, a technique (that employs spatial and temporal analysis of the riser response signal) is developed to empirically identify the natural frequency of a riser directly from data (response measurements) and to automatically select a set of modes for use with the WWA method. Fatigue damage rates, estimated based on the riser response reconstructed using the WWA method with the proposed automated mode selection technique (we refer to this as "improved" WWA) are cross-validated against fatigue damage rates based directly on measurements at the same discrete locations. Results show that the improved WWA method may be employed quite effectively to estimate fatigue damage rates from limited strain measurements.

It is worth noting that if some physical properties (such as the mass, length, and tension) of a riser are known, by using the empirically estimated riser fundamental frequency that did not use such properties, it is then possible to estimate a spatio-temporal averaged value of the added mass coefficient. It is also possible to investigate the relationship between this averaged added mass coefficient and the current type (speed and profile), given a large number of data sets that include measurements of the riser response.

4.2 Applications of Weighted Waveform Analysis

Weighted Waveform Analysis (WWA) is a computational procedure that is used to analyze and reconstruct the response over the entire length of a riser from measurements at a limited number of sensors [54], [33]. The method represents the riser response as the sum of a set of weighted waveforms or modes (more precisely, the summation is over estimated time-varying weights applied to selected riser spatial mode shapes). These modes need to be selected using knowledge of the VIV phenomenon and/or based on available data. The extent to which the selected modes can realistically describe the riser response affects the quality of response reconstructions using the WWA method. Thus, mode selection is vital in the WWA application. Different mode selection procedures distinguish the different applications of WWA in riser response reconstruction. Some studies (see, Lie and Kaasen [33], for example) have used a set of consecutive modes distributed in a band around the dominant frequency and, thus, the riser response for frequencies only around the Strouhal frequency was effectively considered since only a limited number of modes can be included due to usually a small number of available sensors. In contrast, with the WWA method and while still using a limited number of sensors, we have proposed a procedure to select a set of non-consecutive modes, which thus allow directly for consideration of higher harmonics (responses at frequencies that are multiples of the Strouhal frequency) in the riser response representation (see Chapter 3).

The WWA mode set should best capture response characteristics in the measured data and its selection may be obtained using the following general guidelines: (i) Given a suite of riser response records, each measured at a discrete spatial location, first, conduct a spectral analysis of all these time series. Then, obtain a composite representation of all the sensors—such as the sum of the power spectra at all these spatially distributed sensors; and (ii) From the composite spectrum, select a set of spectral peaks and convert the associated peak frequencies into riser mode numbers by dividing these frequencies by an estimate of the fundamental natural frequency of the riser (if string-like behavior of the riser can be assumed).

The riser's fundamental natural frequency may be estimated (by modeling the riser as a tensioned string or beam), if the physical and hydrodynamic properties of the riser, such as the mass, bending stiffness, and added mass coefficient, are known. Among them, the added mass coefficient is one of the most complex and least understood hydrodynamic parameters that influences riser VIV response. Its value is not a constant; it is affected by many parameters such as the vibration amplitude and the current velocity [46]. In previous applications (as were shown in Chapter 3), the added mass coefficient was assumed to take values of 0 and 1, respectively, for uniform and sheared current flows on the NDP model riser. These assumed values were based on observations of the propagation speed of traveling waves from a separate analysis with the available NDP data sets. This assumption on added mass, though it was shown to lead to accurate riser response reconstruction (at least for the analyzed data sets) lacks generality since it only applies to the riser analyzed; more importantly, the requirement of knowledge/assumptions about the riser physical and hydrodynamic properties limits the attractiveness of the empirical WWA method to some degree.

In light of the preceding discussion, we seek an approach that will lead to an estimation of the natural frequencies of the riser directly from the data (i.e., the riser response measurements) and will rely neither on assumptions of the added mass coefficient nor on any physical properties of the riser. Our approach relies on estimating the riser's dominant mode number by first performing a "spatial" spectral analysis on the response measurements; this is then followed by estimation of the riser's dominant mode frequency by "temporal" spectral analysis on the measurements. The fundamental natural frequency of the riser may then be estimated as the dominant mode frequency divided by the dominant mode number. Then, the set of peak spectral frequencies selected from the composite power spectrum (obtained from all the sensors) are all assigned appropriate mode numbers by dividing these frequencies each by the empirically estimated fundamental natural frequency. The assumption of string-like behavior is implicit in such assigning of mode numbers. Once the index numbers of all the modes in this mode set have been determined in this manner, the WWA method is employed (in a similar manner to that presented in Chapter 3) to reconstruct the response over the entire length of the riser from the limited number of strain measurements.

At selected target locations, we compare fatigue damage rates, estimated based on the riser response reconstructed using the WWA method with the proposed automated mode selection technique (we refer to this as "improved" WWA), with those based on the "original" WWA method (that relies on a theoretically computed fundamental natural frequency of the riser, as presented in Chapter 3). In both cases, predicted fatigue damage rates based on the empirical methods and data at various locations (other than the target) are cross-validated against damage rates based directly on measurements at the target location. Results show that the improved WWA method, which empirically estimates the riser's fundamental natural frequency and automatically selects significant modes of vibration, may be employed quite effectively to estimate fatigue damage rates from limited strain measurements.

4.3 Identification of the Dominant Wavenumber

Whenever riser response is recorded in measurements, it is done at uniform and short time intervals—i.e., temporal resolution is usually very fine. If the spatial location of sensors along a riser's length were similarly well resolved, it would be straightforward to carry out a full two-dimensional Fourier transform of these two-dimensional data. A temporal Fourier transform allows one to go from the time domain to the frequency domain; similarly, a spatial Fourier transform would allow one to go from the space domain to the wavenumber domain. Hence, the riser response could be represented by a frequency-wavenumber diagram [1]. The frequencies and wavenumbers of the dominant riser mode(s) could then be identified from the locations of spectral peaks. Since sensors are not densely placed along the riser, spatial resolution is not fine; also the sensors are generally non-uniformly distributed along the riser length—hence, a two-dimensional Fourier transform cannot be readily obtained using available data. Although non-uniform spatial data may be interpolated into suites of uniformly spaced data sets prior to analysis, interpolation imposes assumed patterns between available samples that can introduce artificial harmonics in any computed spatial spectra.

There are a range of methods available for estimating the wavenumber of an oscillating beam (or structure, in general) from spatially distributed samples; however, most of these methods have specific requirements for their application. For example, Prony-based methods require that the sensors must be evenly spaced spatially [20], while the method employed by McDaniel and Shepard [39] requires that no excitation is applied within the spatial spread of the sensors. These methods proposed for oscillating beams are not well suited for estimating the wavenumber of VIV-excited modes of risers.

In this study, we propose a method for identifying the wavenumber of the dominant riser mode by computing the Lomb-Scargle periodogram from the spatial covariance function of riser response measurements. The Lomb-Scargle periodogram is a widely used spectral analysis technique for unevenly spaced data; for additional details on its implementation and use, the reader is referred to the original studies of Lomb [35] and Scargle [47]. The theoretical basis and formulation as well as some discussion on the selected approach for our proposed wavenumber identification procedure is presented in some detail next.

4.3.1 Riser Response and the Spatial Covariance Function

Assume that at location, z, and at time, t, the riser response (such as strain), i.e., $x(z,t)$, can be expressed in general as the sum of the contribution from N modes:

$$\begin{aligned} x(z,t) = \sum_{n=1}^{N} \{ & a_{n1}\cos(k_n z)\cos(\omega_n t) + a_{n2}\sin(k_n z)\cos(\omega_n t) \\ & + a_{n3}\cos(k_n z)\sin(\omega_n t) + a_{n4}\sin(k_n z)\sin(\omega_n t)\} \end{aligned} \tag{4.1}$$

in which the n^{th} mode, with wavenumber, k_n, and frequency, ω_n, consists of four parts: the term, $a_{n1}\cos(k_n z)\cos(\omega_n t)$, represents a standing wave that permits oscillation of the riser boundaries; the term, $a_{n2}\sin(k_n z)\cos(\omega_n t) + a_{n3}\cos(k_n z)\sin(\omega_n t)$, represents a traveling wave along the riser axis; and the term, $a_{n4}\sin(k_n z)\sin(\omega_n t)$, represents a standing wave with unmoving boundaries.

Given riser responses measured at M locations, $x_1, x_2, \ldots, x_M$, where $x_i \equiv x(z_i, t)$, the spatial covariance between riser response values at two locations, z_i and z_j $(1 \le i, j \le M)$, is defined as follows:

$$\begin{aligned}
\mathrm{Cov}[x_i, x_j] =& \mathrm{E}\left[(x_i - \mathrm{E}[x_i])(x_j - \mathrm{E}[x_j])\right] \\
=& \sum_{n=1}^{N} \{F_n[k_n(z_i - z_j)] + G_n[k_n(z_i + z_j)]\} \\
F_n[k_n(z_i - z_j)] \equiv& \frac{a_{n1}^2 + a_{n2}^2 + a_{n3}^2 + a_{n4}^2}{4}\cos(k_n(z_i - z_j)) \\
G_n[k_n(z_i + z_j)] \equiv& \frac{a_{n1}^2 - a_{n2}^2 + a_{n3}^2 - a_{n4}^2}{4}\cos(k_n(z_i + z_j)) \\
&+ \frac{a_{n1}a_{n2} + a_{n3}a_{n4}}{2}\sin(k_n(z_i + z_j))
\end{aligned} \tag{4.2}$$

Equation 4.2 shows that, as is the case with $x(z, t)$, the covariance function, $\mathrm{Cov}[x_i, x_j]$, between $x(z_i, t)$ and $x(z_j, t)$ can also be expressed as a sum of N mode components, and its n^{th} mode is comprised of two trigonometric functions, $F_n[k_n(z_i - z_j)]$ and $G_n[k_n(z_i + z_j)]$. This suggests the possibility of identifying wavenumbers based on the spatial covariance function.

4.3.2 Identification of Wavenumber using Spectral Analysis on Spatial Covariance Function

A suite of riser response measurements at M locations, $x_1, x_2, \ldots, x_M$, allows one to construct an $M \times M$ covariance matrix using all pairs of measurements, and resulting in $M(M-1)/2$ off-diagonal entries. A study of Eq. 4.2 suggests a possible way to identify the wavenumber, k_n, using spectral analysis on the covariance function: assume that covariance is a function of Δz ($\Delta z \equiv |z_i - z_j|, 1 \leq i, j \leq M$) and that the part associated with $z_i + z_j$, i.e., $G_n[k_n(z_i + z_j)]$, is noise. If we conduct a spectral analysis on the covariance function with respect to Δz, it is then theoretically possible to identify the wavenumber, k_n, of the n^{th} mode, based on locations of the spectral peaks.

It would seem that it should also be possible to identify the wavenumber, k_n, of the n^{th} mode by conducting a spectral analysis on the covariance function with respect to $z_i + z_j$—i.e., by assuming that covariance is a function of $z_i + z_j$. However, the former option (assuming covariance is a function of Δz) is preferred since it has physical meaning in that it assumes that the covariance of the riser response measured at two spatially separated locations is a function of the relative distance between those two locations. More importantly, the function, $F_n[k_n(z_i - z_j)]$, offers higher spatial resolution than the function, $G_n[k_n(z_i + z_j)]$—this makes it especially useful in identifying the dominant wavenumber especially when sensors are sparsely spaced.

Two important points are discussed here—first, usually only wavenumbers of the lower modes (which preserve larger portions of the total energy) can be accurately and reliably identified using this method due to the sparsely spaced sensors; and, second, the proposed wavenumber identification method is especially well suited for use with unevenly spaced sensors, which is one of appealing features of this procedure for riser response reconstruction. In the following, we treat the covariance as a function of Δz, and estimate the wavenumber, k_n, from the Lomb-Scargle periodogram of the spatial covariance function. Note that the wavenumber, k_n, can be immediately related to the riser response wavelength, $\lambda_n = 2\pi/k_n$ and, hence, with a riser mode number, n, where $k_n = n\pi/L$ where L is the length of the riser.

4.4 WWA Procedure with Automated Mode Selection—Single Target Sensor

In the following, we use a sheared current data set, NDP 2350, with strain sensor no. 4 (located at $z/L = 0.11$; where L is the riser length) selected as the target, to illustrate application of the empirical procedure involving WWA with temporal and spatial spectral analysis. Note that results using each of the twenty-four sensors as target are presented in the next section.

In order to accurately analyze and reconstruct the riser response using the WWA procedure, an optimal number and choice of modes that can describe the riser response needs to be selected. In the present study, where twenty-three strain sensors are available, we find that a set of twelve carefully selected modes can be used to describe the riser response with reasonable accuracy (i.e., we use $N = 12$ with Eq. 3.2). The procedure employed for selecting the specific twelve modes is briefly described here.

The CF strain time series, $\varepsilon(z_j, t)$, measured at each of the twenty-three locations, z_j (where $j = 1, 2, 3, 5, \ldots, 24$; i.e., assuming that target sensor no. 4 does not exist), allow us to construct a 23 × 23 spatial covariance matrix, $\mathbf{Cov}[\varepsilon(z_i, t), \varepsilon(z_j, t)]$. Due to symmetry, we may keep only the lower or upper half of the covariance matrix. If we plot the covariance as a function of

$\Delta z \equiv |z_i - z_j|$, a periodic pattern is observed as illustrated in Fig. 4.1(a). As we saw in Eq. 4.2, the wavenumber of the covariance function with respect to Δz is identical to the wavenumber of the strain response, and this wavenumber may be identified using spectral analysis. Due to the non-uniform spacing of the data/sensors, we use the Lomb-Scargle algorithm to identify the periodic pattern [35], [47]. Figure 4.1(b) shows the Lomb-Scargle spectrum of the spatial covariance—the x-axis denotes the mode number, n (related to the wavenumber, k_n; $k_n = n\pi/L$) while the y-axis denotes the Lomb-Scargle spectrum with units of micro-strain raised to a power of 4, i.e., $(\mu\varepsilon)^4$. This spectrum is computed using an over-sampling parameter equal to 6; the highest mode number equals 30. The significance level of 0.001 is indicated with a dashed line. The meaning of these various parameters employed for the Lomb-Scargle spectrum is discussed elsewhere [44]. From the location of the dominant spectral peak as illustrated in Fig. 4.1(b), the dominant riser mode is identified as the 5^{th} mode. In this example, only the 5^{th} mode is unambiguously identified; this is likely because this 5^{th} mode carries a much larger portion of the total energy compared with other higher riser modes.

After identifying the dominant riser mode number, the next step is to identify the frequency associated with this dominant mode; this is the dominant riser frequency. This frequency can be directly estimated by carrying out a Fourier spectral analysis using the time series data since these data are uniformly sampled and well resolved in time. For the CF strain measured at location z_j, i.e., $\varepsilon_j(t)$, the power spectral density (PSD), $PSD_j(f)$, describes the energy distribution by frequency at that location. As illustrated in Fig. 4.2(a), the twenty-three input strain power spectra exhibit very simi-

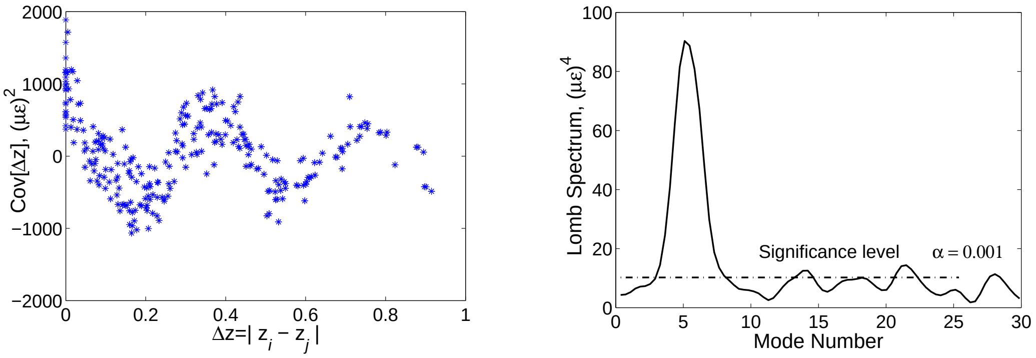

(a) (b)

Figure 4.1: Identification of the dominant riser mode number when sensor no. 4 is the target: (a) spatial covariance vs. spatial separation between sensors; and (b) Lomb-Scargle periodogram of the covariance.

lar frequency content; all these spectra indicate the presence of the first and third harmonics in the response. The composite sum of the PSDs from all the twenty-three sensors, i.e., $\sum_j PSD_j(f)$ (see Fig. 4.2(b)), accounts for the energy distribution by frequency over the entire riser and is, therefore, used for identifying first the dominant riser frequency and then the fundamental riser natural frequency. It also leads to selection of the optimal mode set for the WWA scheme. This is discussed next.

From Fig. 4.2(b), the dominant spectral frequency is found to be 3.37Hz. The fundamental natural frequency of the riser is estimated as the dominant spectral frequency divided by the dominant mode number, i.e. $3.37/5 = 0.67$Hz. If one assumes that the riser can be modeled as a tensioned string and its bending stiffness is negligible (this assumption holds for a large proportion of deepwater risers as well as for the NDP model riser analyzed here), the natural frequencies of higher modes are approximated as integer multiples of

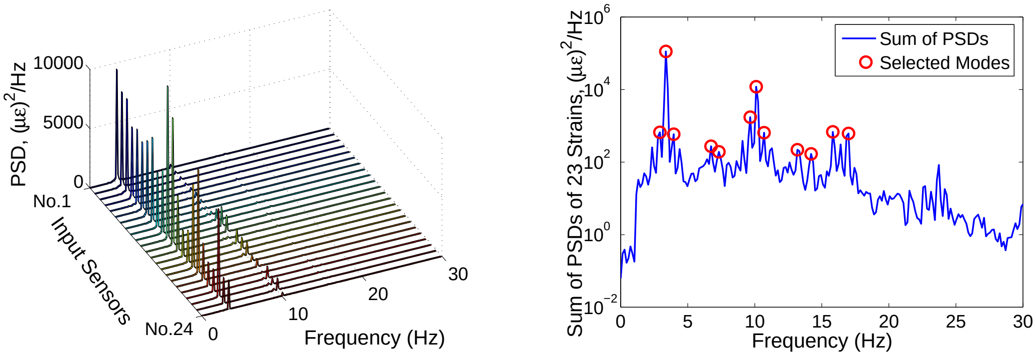

(a) (b)

Figure 4.2: Selection of an optimal set of frequencies for the WWA scheme when sensor no. 4 is the target: (a) PSDs of the strains measured at the twenty-three sensors; and (b) summation of the strain PSDs from all 23 sensors and identification of the important frequencies.

the fundamental natural frequency.

The twelve highest PSD peaks in Fig. 4.2(b) are selected and the associated riser mode numbers are determined by comparing these peak frequencies with the estimated natural frequencies of the riser. As illustrated in Fig. 4.2(b), these selected twelve modes range from the first to the fifth harmonic of the riser (note that the first harmonic is the riser's fifth natural mode of vibration).

After selecting the "optimal" mode set for the WWA scheme, strain time series at any location over the entire riser length, including at the location of the target sensor, can be reconstructed. Figure 4.3(a) compares the energy distribution by frequency of the reconstructed strain (dashed line) with that of the measured strain (solid line) at the location of the target sensor (sensor no. 4); the comparison suggests that the first and higher riser harmonics are reasonably well represented by the reconstructed response based on application of the WWA method. Figure 4.3(b) compares the reconstructed RMS curvature values with the measured values at various locations: the circles indicate the values at the twenty-three input sensors and the cross indicates the value at the target sensor. The solid line indicates reconstructed RMS curvatures obtained using the WWA procedure. These results suggest that the RMS values of the reconstructed curvature reflect the presence of the first and higher harmonics and that the reconstructions match the measurements reasonably well, at least at all of the sensor locations. RMS values of the displacement (normalized with respect to the outer diameter of the riser, D) are also reconstructed over the entire length of the riser, as shown in Fig. 4.3(c), and compared with corresponding values based on double-integrated accelerations measured at eight available locations where accelerometers are available. Based on Figs. 4.3(b) and 4.3(c), one can say that the WWA-based response reconstructions match the measurements reasonably well; the relatively larger deviations between estimated and measured values towards the top and bottom ends of the riser may be explained by the assumption of the sine mode shapes which have fixed ends. Finally, Fig. 4.3(d) shows the off-diagonal elements of the orthogonality matrix computed for the twelve modes selected in this example. The relatively low values of the off-diagonal elements of the orthogonality matrix seen in the figure confirm that spatial aliasing is not of concern and that higher modes can be reconstructed with the WWA method.

At target sensor no. 4, the fatigue damage ratio (DR), representing the ratio of the estimated fatigue damage based on WWA-based riser reconstruction to the fatigue damage based on measurements at that same sensor is 1.66, which suggests that, at least for this target sensor, the fatigue damage is overestimated by a factor of 1.66 by the WWA method. Results for other

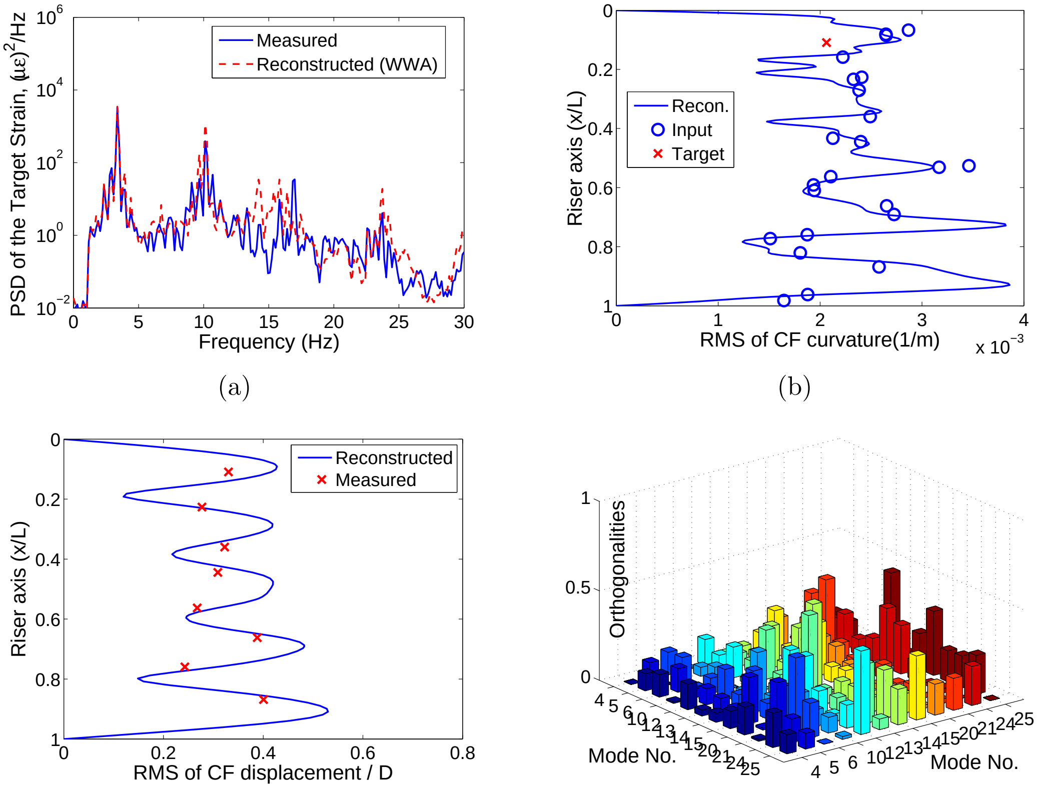

(a) (b) (c) (d)

Figure 4.3: Response reconstruction based on the improved WWA method when sensor no. 4 is the target: (a) PSD of the strain at the target sensor location: reconstructed vs. measured; (b) RMS of curvature: reconstructed vs. measured; (c) RMS of displacement: reconstructed vs. measured; and (d) off-diagonal terms of the orthogonality matrix for the selected modes.

choices as target sensor are discussed in the next section.

4.5 WWA Procedure with Automated Mode Selection—All Target Sensors

The procedures for employing the WWA method together with the temporal and spatial data analyses needed to reconstruct the riser response from a limited number of measurements have been illustrated on one example data set, NDP2350, and for one target sensor (sensor no. 4). By selecting each of the twenty-four strain sensors as target, one at a time, the same procedures are repeated on all the four NDP data sets available in the public domain (see Appendix A). Results from these analyses are presented in Fig. 4.4. Damage ratio (DR) estimates using the improved WWA method shown by circles are compared with similar estimates using the original WWA method shown by asterisks. We again note the differences between the two different WWA methods are: (i) with the improved WWA method, one does not require physical properties of the riser, and the fundamental natural frequency of the riser is empirically estimated from the data; and (ii) the original WWA method requires physical properties of the riser as well as assumptions about the added mass coefficient, and the riser's natural frequencies are computed theoretically based on the tensioned string equation. The lowest and highest damage ratios, representing estimations with the least accuracy, that resulted from the two WWA-based methods for each of the four data sets are also presented in the figure legends—for example, in Fig. 4.4(a) where results for the NDP2120 data set are presented, damage ratios estimated using the improved WWA method range from 0.41 to 4.69 while these estimates using the original WWA method range from 0.25 to 6.58.

The following observations are made by studying Fig. 4.4.

(i) Even though the proposed improved WWA method does not require or use any physical properties of the riser, it still provides reasonably accurate estimates of fatigue damage rates over the entire riser length—damage ratios are typically range from 0.3 to 3.0, with smallest and largest estimations of

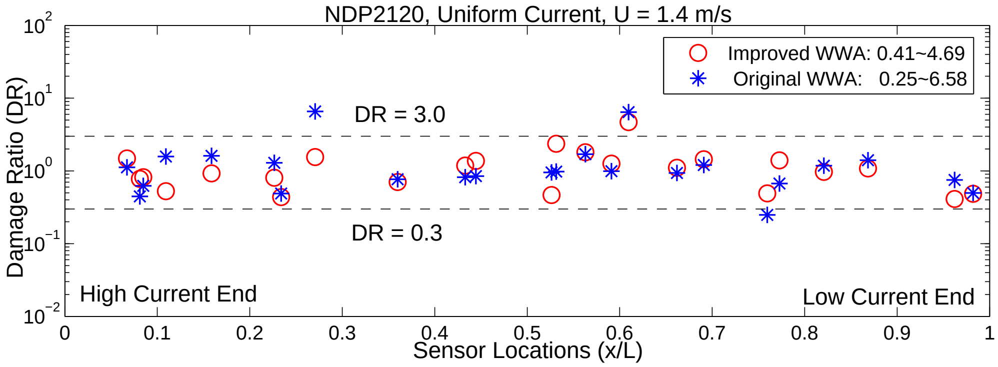
NDP2120, Uniform Current, U = 1.4 m/s
Improved WWA: 0.41~4.69
Original WWA: 0.25~6.58
DR = 3.0
DR = 0.3
High Current End
Low Current End
Damage Ratio (DR)
10^{2}
10^{1}
10^{0}
10^{-1}
10^{-2}
0
0.1
0.2
0.3
0.4
0.5
0.6
0.7
0.8
0.9
1
Sensor Locations (x/L)

(a)

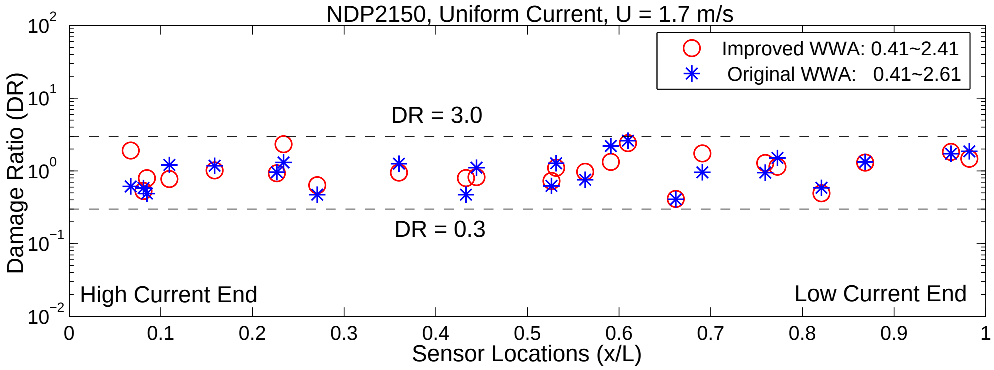
NDP2150, Uniform Current, U = 1.7 m/s
Improved WWA: 0.41~2.41
Original WWA: 0.41~2.61
DR = 3.0
DR = 0.3
High Current End
Low Current End
Damage Ratio (DR)
10^{2}
10^{1}
10^{0}
10^{-1}
10^{-2}
0
0.1
0.2
0.3
0.4
0.5
0.6
0.7
0.8
0.9
1
Sensor Locations (x/L)

(b)

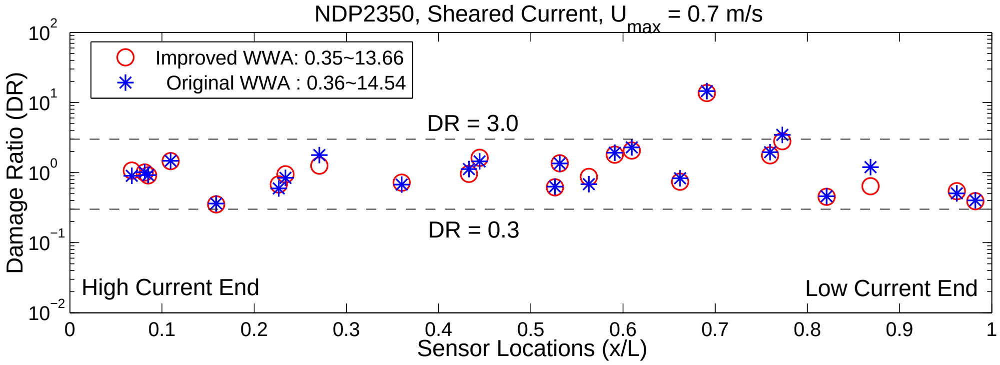
NDP2350, Sheared Current, U_{max} = 0.7 m/s
Improved WWA: 0.35~13.66
Original WWA : 0.36~14.54
DR = 3.0
DR = 0.3
High Current End
Low Current End
Damage Ratio (DR)
10^{2}
10^{1}
10^{0}
10^{-1}
10^{-2}
0
0.1
0.2
0.3
0.4
0.5
0.6
0.7
0.8
0.9
1
Sensor Locations (x/L)

(c)

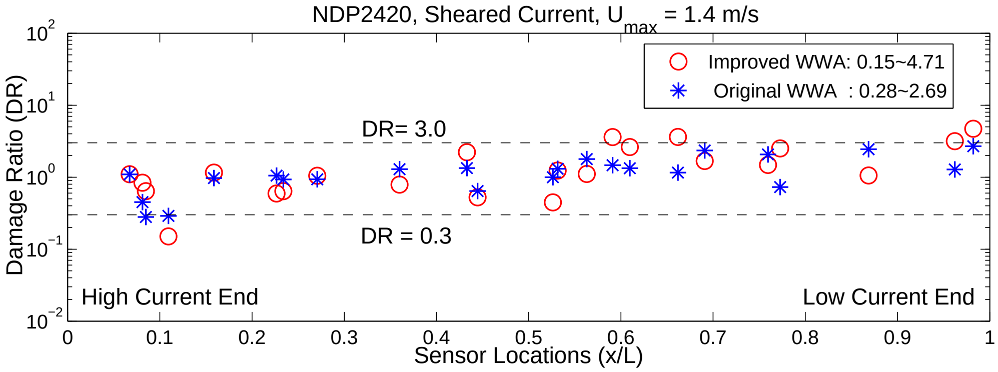

(d)

Figure 4.4: Damage ratios estimated using the WWA procedure: (a) NDP2120, uniform current with speed of 1.4 m/s; (b) NDP2150, uniform current with speed of 1.7 m/s; (c) NDP2350, sheared current with maximum speed of 0.7 m/s; and (d) NDP2420, sheared current with maximum speed of 1.4 m/s.

0.15 and 13.66, respectively.

(ii) Both WWA methods, although they require different amounts of a priori knowledge about the riser, generally lead to estimated fatigue damage rates of similar accuracy levels, at least with these NDP data sets and with the arrangement of sensors for this model riser.

(iii) If physical properties of a riser are available as is the case for the NDP model riser (see Appendix A), estimates of the added mass coefficient may be computed using the empirically estimated natural frequency of the riser and based on the tensioned string equation. Table 4.1 compares such empirically estimated added mass coefficients (inferred from the riser fundamental natural frequency estimated with the improved WWA method) with coefficients that were assumed when the original WWA method was employed for these NDP data sets. The estimated values are found to be in close agreement with the

Table 4.1: Comparison of the empirically estimated and assumed values of the added mass coefficient (C_a).

Event no.	Current profile	Empirically estimated value	Assumed value
2120	Uniform	0.04	0.00
2150	Uniform	0.04	0.00
2350	Sheared	0.94	1.00
2420	Sheared	0.70	1.00

assumed values used with the original WWA approach; this explains why DR estimates calculated by the two WWA schemes are also in close agreement with each other for all target sensor locations and for all four data sets.

In addition to the four NDP data sets discussed here, the improved WWA method was also applied to many other NDP bare riser data sets that included uniform and linearly sheared current profiles where the maximum current speed ranged from 0.3 to 2.4 m/s. Results from those analyses showed that, over a wide range of flow conditions, the improved WWA method can provide reasonably accurate response reconstruction over the entire riser length even when based on measurements at only a limited number of locations.

Note that, as part of the improved WWA method, given response measurements, one can estimate the fundamental natural frequency of the riser, select the important riser modes, and reconstruct the riser response over the entire length. This whole process can be done in an almost automated fashion with limited manual input/interference. However, it is recommended that the reconstructed riser response should be checked a posteriori for consistency with expectations of proper VIV behavior given the actual physical properties of the riser and current flow characteristics.

4.6 Conclusions

In this study, the empirical riser response reconstruction procedure referred to as weighted waveform analysis (WWA), was improved relative to previous studies using this method in that the mode or waveform selection procedure was changed to require no assumptions on added mass coefficient and no information on riser physical properties. The fundamental natural frequency of the riser is estimated through separate estimation of (i) the dominant riser response frequency through temporal data analysis—specifically, Fourier spectral analysis of the riser response; and (ii) the dominant wavenumber through spatial data analysis—specifically, Lomb-Scargle spectral analysis of the spatial covariance variation with sensor spacing. Then, mode selection for WWA follows by identifying riser mode numbers that line up with peaks in response power spectra. The relevant mathematical background for this less commonly used wavenumber identification procedure and its application were discussed briefly. By employing the improved WWA method on four NDP data sets, fatigue damage rates at various locations along the riser length were estimated using measurements from twenty-three sensors as inputs. These estimates were cross-validated against fatigue damage rates computed directly from measurements at the same (target) locations. The fatigue damage rates estimated from the improved WWA method were compared with those from the original WWA method. Results showed that, even without employing any information on the physical properties of the riser or any assumptions on added mass coefficients, the improved WWA method can estimate fatigue damage rates quite accurately from a limited number of strain measurements. The proposed wavenumber identification procedure may also be used to estimate the spatio-temporal averaged values of the added mass coefficient directly from the data and, thus, the method offers a possible approach for detailed studies of the relationship between the added mass coefficient and current velocity profiles, especially for long flexible risers.

Chapter 5

Empirical Long-Term Prediction of Fatigue Damage Rate

5.1 Introduction

Risers are often instrumented in field monitoring campaigns wherein the dynamic response in the form of strains and/or accelerations is recorded at several discrete locations along the length of the riser. Often, simultaneously, current velocity profiles at a nearby location are also recorded. The development of robust methods to interpret the data from these costly measurements and use them to estimate the cumulative fatigue damage and the remaining fatigue life at locations of interest on the riser is of great practical importance to ensure its integrity. The oil and gas industry has generally relied on analytical tools for VIV-related fatigue damage prediction for a riser given a specific current profile. These analytical tools model a riser using the finite element method, which requires information on riser physical properties. Such approaches also often rely on simplifying assumptions on both the flow conditions and the response characteristics. As an alternative, when field monitoring is undertaken, empirical procedures may be used to estimate the fatigue damage rate at locations of interest on the instrumented riser from a limited number of measurements, even in the absence of information on the physical and hydrodynamic properties of the riser (such as the added mass coefficient—see Chapters 3 and 4). If a significant amount of data is available, it is possible to establish "short-term" fatigue damage rate distributions conditional on current type. If the relative frequency of different current types is known from metocean studies, the short-term fatigue distributions can be combined with current distributions to yield integrated "long-term" fatigue damage rate distributions.

In this chapter, we use an empirical procedure, referred to as Weighted Waveform Analysis (WWA), and seek to demonstrate the methodology for empirical long-term fatigue damage assessment and life prediction for an instrumented marine riser. (Note, for the WWA procedure, we use the version of it that employs automated mode selection as presented in Chapter 4.) There are clear advantages of such empirical approaches to fatigue damage and life estimation over analytical approaches. First, only measured strain and/or acceleration data are required; neither physical properties of the riser nor simplifying assumptions on the current profiles are needed. The data explicitly account for the different response characteristics and for the different current profiles experienced by the riser. Second, estimates of fatigue damage rates and remaining life are easily updated as new data become available from any ongoing field monitoring campaign.

5.2 Empirical Long-Term Fatigue Damage Estimation Based on Limited Measurements

During a riser monitoring campaign, the response (e.g., strain and/or acceleration) is recorded by an array of data sensors placed at discrete locations along the length of the riser; often current velocity profiles are also recorded simultaneously at a nearby location. We assume that the campaign produces a total of N_T events. An "event" refers to a suite of recorded riser response time series (from all spatially distributed sensors) and an associated current profile. Practically, it is impossible to measure the riser response at all locations of interest (or fatigue-sensitive details) because the riser may be very long and instrumentation costs might only allow a limited number of sensors. The objective of this study is to present a methodology to empirically predict the fatigue damage and life at the location of any fatigue detail of interest along the length of the riser, using measurements from a limited number of sensors. The steps in the proposed methodology are schematically described in the flowchart shown in Fig. 5.1. These steps include: (i) classification of events based on current profile; (ii) variability analysis of empirical short-term fatigue damage estimates; and (iii) prediction of long-term fatigue damage and life. Relevant important equations related to the various steps in the process are presented in the flowchart and will be explained in detail in the following. Note that the predicted long-term fatigue damage and the probability of failure can be updated as additional data are recorded in continuing or new monitoring campaigns.

The three main steps in the flowchart of Fig. 5.1 are briefly described as follows:

(1) *Classification of events based on current profile.* All of the N_T recorded events are divided into N_G groups based on contrasting metocean current classes. The distinct current profiles define the groups; while not assured, the dynamic response to events within a single group should have more similarities than might be expected across groups. The relative likelihood of occurrence

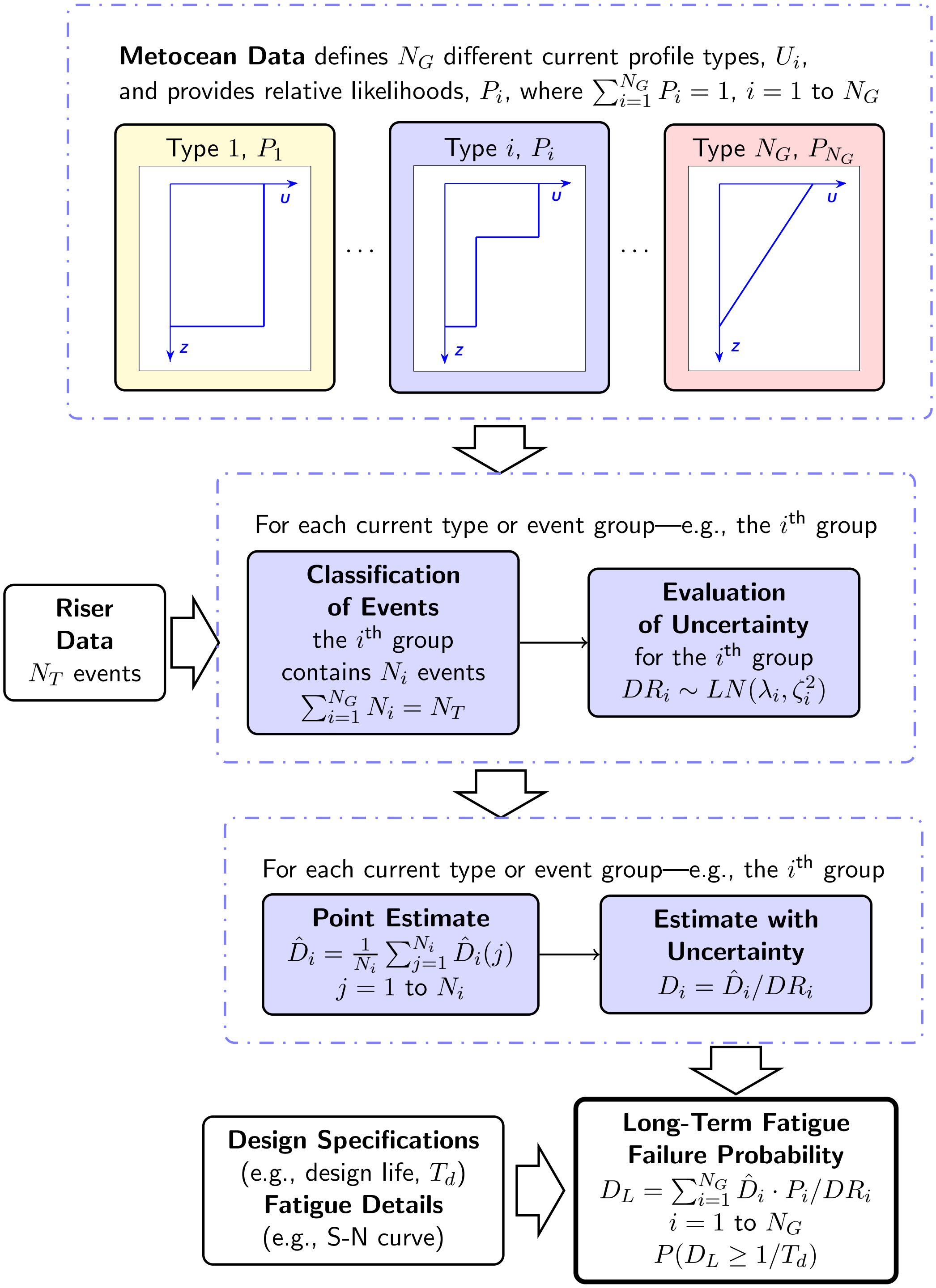

Figure 5.1: Flowchart showing algorithm for empirical prediction of long-term fatigue damage and failure probability for an instrumented riser.

of each group (or current profile type) is expected to be available from metocean studies. The probability of occurrence of the i^{th} group (where $i = 1$ to N_G), which contains N_i events, is denoted as P_i, where $\sum_{i=1}^{N_G} N_i = N_T$ and $\sum_{i=1}^{N_G} P_i = 1$.

(2) *Variability analysis of short-term fatigue damage estimates.* Given an event that belongs to the i^{th} group, we select one sensor as the "target" sensor. Then, we attempt to reconstruct the riser response at the location of the target sensor by WWA using measurements from all the remaining sensors (except the target sensor). We define a parameter, Damage Ratio (DR), which represents the ratio of the fatigue damage rate computed based on the WWA-based reconstructed riser response to that based on direct measurements at the target sensor. We refer to this as a cross-validation check. We repeat this cross-validation exercise by selecting each sensor as the target sensor, one at a time, and computing DR for that sensor. We iterate over all the events in the i^{th} group. In this manner, we obtain numerous estimates of DR for all the sensors and for all the events in the i^{th} group. Next, we establish a probability distribution for DR for each group; this distribution describes the variability in the empirical fatigue damage estimation associated with all events that belong to the i^{th} group. This variability analysis is carried out for all the current profile groups.

(3) *Prediction of long-term fatigue damage and life.* Given an event, we attempt to reconstruct the riser response and estimate the fatigue damage rate at any location of interest (or critical fatigue detail on the riser) by using the empirical method (e.g., WWA, here, although other methods discussed in Chapter 3 may be used instead) with the help of a limited number of measure-

ments. This leads to a "point estimate" of the fatigue damage rate caused by that event. Recognition of the uncertainty in this point estimate is accounted for making use of the variability in DR estimated from the previous step; in this manner, the point estimated is corrected and then weighted (or multiplied) by the probability of occurrence of the current class that contains the event. Finally, integration or summation of the point estimate of the fatigue damage rate (adjusted for variability and weighted for occurrence likelihood) over all metocean current classes leads to an empirical estimate of the long-term fatigue damage rate at the location of interest; as well, the probability of failure associated with that location alone can be estimated.

The procedure described above is employed in a study carried out using the NDP bare-riser model tests in uniform and sheared current flow fields. Metocean criteria are simulated by assuming relative likelihoods for the current profile groups used in the experiments. Although CF bending strains were measured at twenty-four strain sensors along the riser, in this study, we only use the strains measured at eight sensors to predict the long-term fatigue damage over the entire length of riser. In order to demonstrate the application and effectiveness of this empirical procedure, we select the location of sensor no. 5 (among the original twenty-four sensors) as our location of interest, and compare the estimated long-term fatigue damage for that location (based on the eight input sensors excluding sensor no. 5) with the "true" value which is calculated directly from the strains measured by sensor no. 5. The locations of the eight input sensors and the assumed location of interest (sensor no. 5) are illustrated in Fig. 5.2.

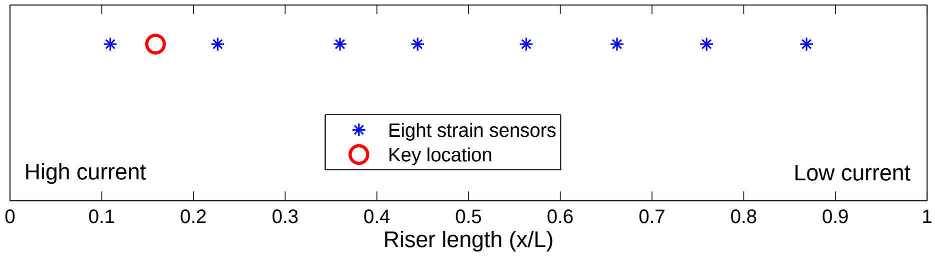

Figure 5.2: Locations of the eight input strain sensors and the key location of interest (assumed to be that of the location of strain sensor no. 5).

Given strains measured at the eight locations, WWA is employed to reconstruct the strain at any key location of interest. Note that WWA does not need physical information about the riser (such as the mass, bending stiffness, added mass coefficient, etc); only the measured response data are needed. Details related to the WWA technique are given in Chapters 3 and 4.

Stresses are directly computed from the strains using a Young's modulus, E, of 36.2×10^9 N/m^2 [10], [54]. The fatigue damage rate is then computed using the rainflow cycle-counting algorithm, Miner's rule, and the F-2 S-N curve (as discussed in Chapter 3).

5.2.1 Classification of Events based on Current Profile

To demonstrate the methodology for long-term fatigue damage estimation, we use the NDP bare-riser model data sets. The classification of events and their relative frequency of occurrence are simply assumed; this simulates the establishing of metocean criteria in a real-world situation. To begin, we assume that current profiles that can cause VIV occur 5% of the time. When such currents do not occur, we assume for this example that no fatigue dam-

Table 5.1: Classification of events according to current profile type.

Group	Current profiles (m/s)	Number of events	Probability of occurrence
G1	Uniform $U \geq 0.3$	24	0.05%
G2	Low shear $0.3 \leq U_{max} < 1.0$	7	4.50%
G3	Moderate shear $1.0 \leq U_{max} < 2.0$	11	0.35%
G4	High shear $U_{max} \geq 2.0$	6	0.10%
	Total	48	5.00%

age occurs. The forty-eight NDP bare-riser data sets, associated with VIV, are divided into four groups; assumed percent occurrence rates for each group are presented in Table 5.1. Note that, collectively, the four current profile groups are assumed to occur 5% of the time.

5.2.2 Uncertainty in Short-Term Fatigue Damage Estimation

The short-term fatigue damage at any key location resulting from a single event can be estimated using WWA with measurements at the eight sensors. The uncertainty or variability in the fatigue estimation can be assessed by means of cross-validation wherein estimations are compared with measurements as follows. Given a total of eight available sensors, we select one of these as the "target" sensor, and compute the DR value (defined earlier) for that sensor using cross-validation. By repeating this procedure for a different target sensor each time until all eight sensors have been selected, we obtain eight DR values for this single event. An empirical distribution of the DR values computed for all the events of a single group can be used to quantify the uncertainty in short-term fatigue damage estimation for that group.

The base-10 logarithms of the eight DR values computed for each of the available events are presented in the form of box-and-whisker plots in Figs. 5.3(a) and 5.3(b) for the 24 uniform current and the 24 sheared current events, respectively. The four current groups, G1 to G4, that contain subsets of these events are also indicated. The maximum current speed associated with each event is indicated on the horizontal axes of the plots. On each box-and-whisker plot, the central mark and the edges of the box represent the median, the 25^{th} percentile (q_1), and the 75^{th} percentile (q_3) of the data; the upper and lower whiskers extend out to $q_3 + 1.5(q_3 - q_1)$ and $q_1 - 1.5(q_3 - q_1)$, respectively. Data that fall outside the whiskers are treated as outliers; these are shown ad "plus" symbols. A study of Fig. 5.3 suggests that the DR values for all the events are clustered around unity and have extremes that roughly range from 0.1 to 10.

In the following, we assume that DR follows a lognormal distribution and we employ statistical methods to test this hypothesis. We take the natural logarithm of DR estimated for a group and linearly transform $\ln(DR)$ to a new variable, x, such that $x = \left(\ln(DR) - \lambda\right)/\zeta$, where λ and ζ are the sample mean and sample standard deviation, respectively, of $\ln(DR)$. If the new variable, x, is a standard normal random variable, then DR is a lognormal random variable. Two types of statistical tests—the Probability Plot Correlation Coefficient (PPCC) test and the Kolmogorov-Smirnov (KS) test—are

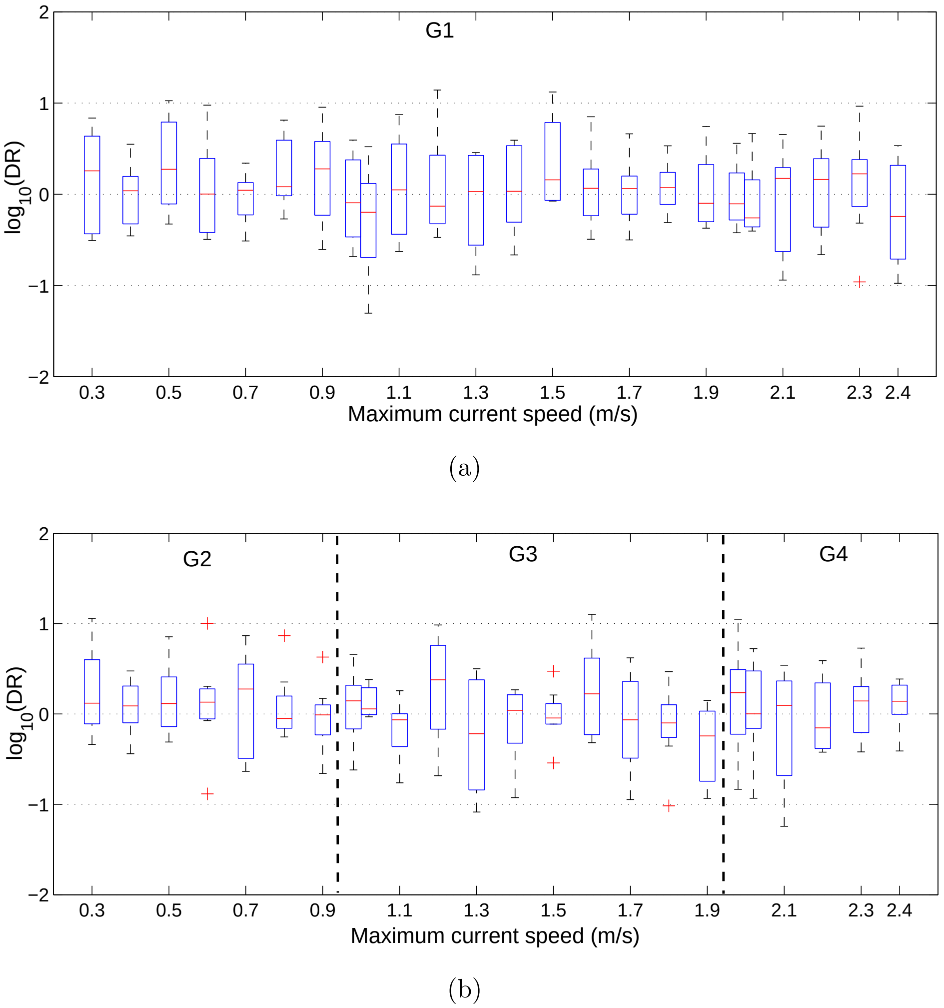

(a)

(b)

Figure 5.3: Damage Ratio (DR) estimates for: (a) uniform current data sets; and (b) sheared current data sets.

performed in order to test for normality of x. Details related to the PPCC test and the KS test are included in Appendixes D and E.

As graphically illustrated in Fig. 5.4, figures on the left show Q-Q plots and figures on the right show cumulative distribution function (CDF) plots for the variable, x. In the Q-Q plots, the sample x quantiles on the vertical axes are compared with the standard normal quantiles on the horizontal axes. The points (shown by crosses) generally lie along the diagonal line; this suggests that x is likely to be normally distributed. In the CDF plots on the right, the empirical CDF (represented by the dashed line) and its 95% confidence bounds (shown with light dotted lines) based on the data, x, are compared with the standard normal CDF (dark solid line). Results from the statistical tests for each group, summarized in Table 5.2, suggest that the data, x, associated with each of the four groups pass both the PPCC test and the KS test for normality at the significance level, $\alpha = 0.05$. Thus, we propose that x for each of the four groups can be modeled as a standard normal random variable; correspondingly, DR for each of the four groups is modeled as a lognormal random variable. Hence, we can write:

$$DR_i \sim LN\left(\lambda_i, \zeta_i^2\right); \quad i = 1 \text{ to } 4 \tag{5.1}$$

where λ_i and ζ_i are the sample mean and sample standard deviation, respectively, of $\ln(DR_i)$. The subscript, i, refers to the i^{th} group. Estimates of λ_i and ζ_i as well as their 95% confidence intervals (CIs) are provided in Table 5.3. As expected, the more samples a group has (for example, G1 has 192 samples), the narrower is the 95% CI on λ_i or ζ_i for that group. Note that, in any ongoing field measurement campaign, it is expected that as additional events are recorded, estimation of the distribution models for DR and, hence, of long-term fatigue damage estimates can be improved.

5.2.3 Long-Term Fatigue Damage and Failure Probability

We have seen that the uncertainty in the short-term fatigue damage estimation for each current profile group can be assessed by modeling DR

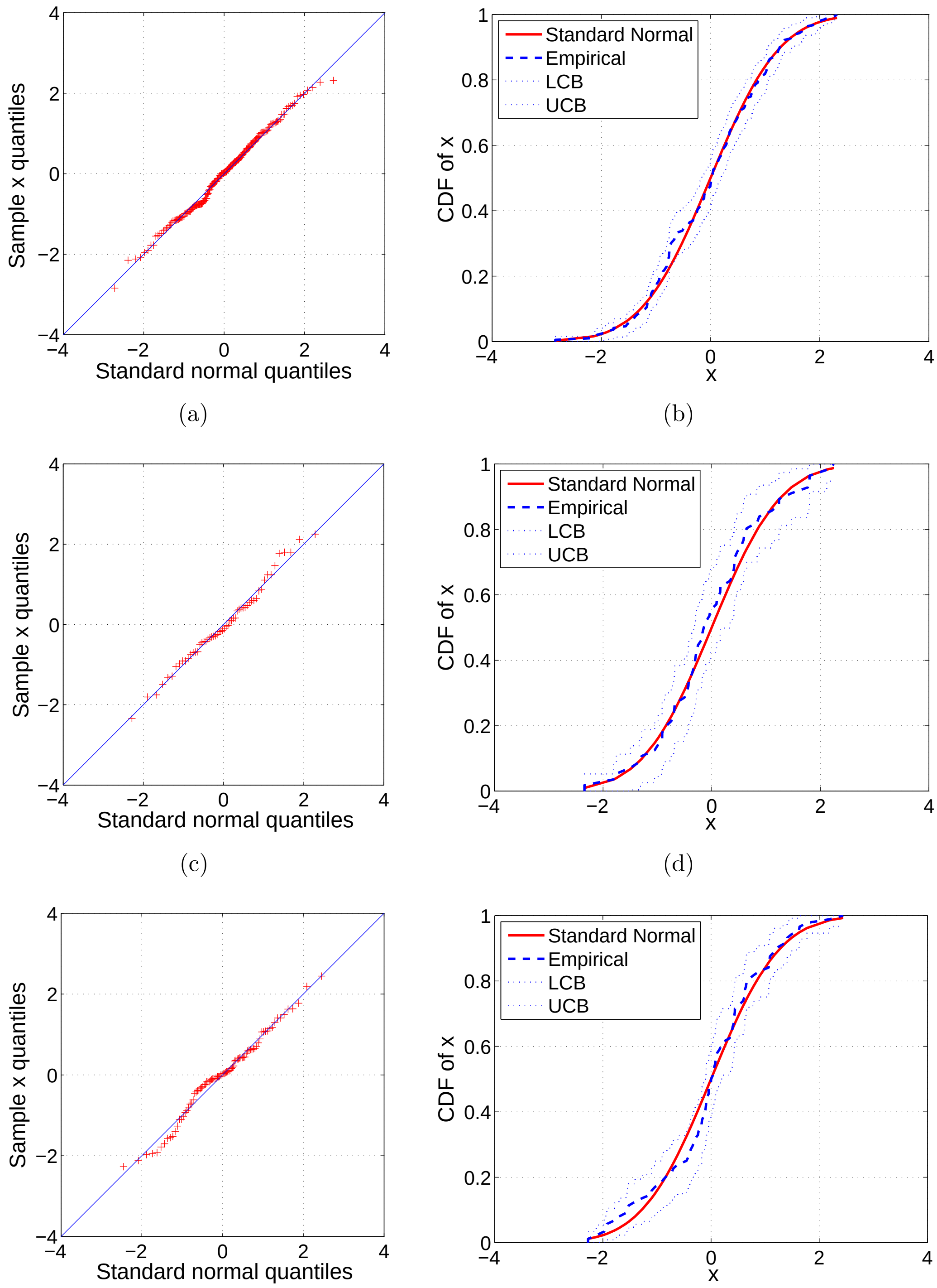
Sample x quantiles
Standard normal quantiles
CDF of x
x
Standard Normal
Empirical
LCB
UCB
−4
−2
0
2
4
0
0.2
0.4
0.6
0.8
1

(a) (b)

(c) (d)

(e) (f)

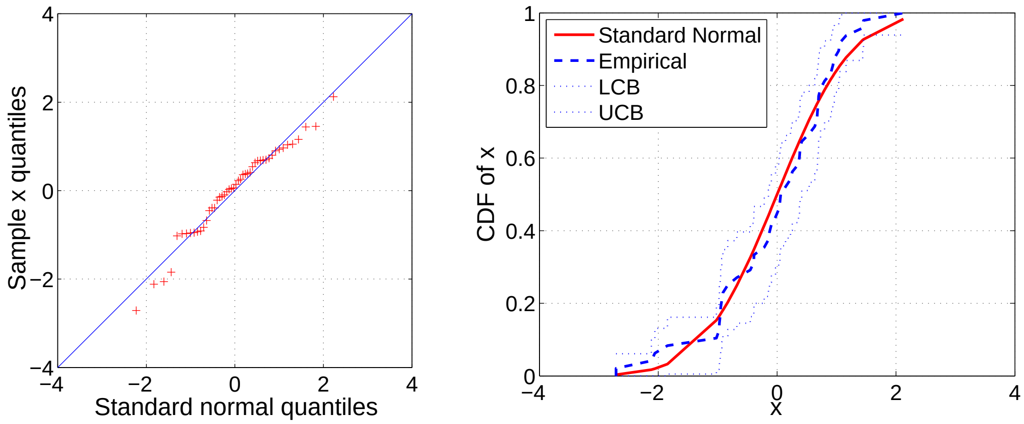

(g) (h)

Figure 5.4: Statistical tests for a normal distribution assumption for $\ln(DR)$: (a) PPCC test for group G1; (b) KS test for group G1; (c) PPCC test for group G2; (d) KS test for group G2; (e) PPCC test for group G3; (f) KS test for group G3; (g) PPCC test for group G4; and (h) KS test for group G4.

Table 5.2: Statistical tests for a normal distribution assumption for $\ln(DR)$ (n = no. of samples in each group; α = significance level for the test).

	PPCC test with $\alpha = 0.05$			KS test with $\alpha = 0.05$		
	r		$r_\alpha(n)$	k		k_α
G1	0.9971	$>$	0.9929	0.0659	$<$	0.0971
$n = 192$		Pass			Pass	
G2	0.9936	$>$	0.9796	0.0628	$<$	0.1782
$n = 56$		Pass			Pass	
G3	0.9917	$>$	0.9862	0.0901	$<$	0.1427
$n = 88$		Pass			Pass	
G4	0.9820	$>$	0.9768	0.0876	$<$	0.1922
$n = 48$		Pass			Pass	

as a lognormal random variable with empirically estimated parameters. This lognormal model will be used now to correct (i.e., endow with uncertainty) the "point estimate" of the fatigue damage rate estimated at the location of

Table 5.3: Parameters of the lognormal distribution for DR_i (the subscript, i, refers to the i^{th} group of events).

	λ_i	95% CI of λ_i	ζ_i	95% CI of ζ_i
G1 ($i = 1$)	0.10	[-0.06, 0.25]	1.09	[0.99, 1.21]
G2 ($i = 2$)	0.24	[-0.02, 0.50]	0.97	[0.82, 1.20]
G3 ($i = 3$)	-0.07	[-0.30, 0.15]	1.07	[0.93, 1.25]
G4 ($i = 4$)	0.09	[-0.22, 0.41]	1.09	[0.91, 1.37]

interest.

For the j^{th} event that belongs to the i^{th} group (denoted as Gi), it is possible to reconstruct strain time series at the location of interest with WWA using strains measured at the eight input sensors. A "point estimate" of the fatigue damage rate (for the j^{th} event) at the location of interest is computed based on the reconstructed strains and is denoted as $\hat{D}_i(j)$. This point estimate of the fatigue damage rate due to all the N_i events in the i^{th} group can be expressed as:

$$\hat{D}_i = \frac{1}{N_i}\sum_{j=1}^{N_i}\hat{D}_i(j); \quad j = 1, \ldots, N_i \tag{5.2}$$

Next, the point estimate for the i^{th} group's fatigue damage rate, adjusted by the uncertainty factor, DR, leads to:

$$D_i = \hat{D}_i / DR_i \tag{5.3}$$

Finally, the long-term fatigue damage rate is obtained by multiplying each D_i by its probability of occurrence, P_i, and summing over all the N_G metocean current classes as follows:

$$D_L = \sum_{i=1}^{N_G} D_i \cdot P_i = \sum_{i=1}^{N_G} \hat{D}_i \cdot P_i / DR_i; \quad i = 1, \ldots, N_G \tag{5.4}$$

Given the design life of the riser, T_d, the probability of fatigue failure can be estimated as follows:

$$P(\text{failure}) = P(D_L \geq 1/T_d) \tag{5.5}$$

In our example, the forty-eight NDP data sets are divided into four groups—so, $N_G = 4$ and $i = 1, \ldots, 4$. The point estimate of the fatigue damage rate (per year) for the i^{th} group, $\hat{D}_i$, the probability of occurrence of that group, P_i, and the empirically estimated statistical parameters, λ_i and ζ_i, for DR_i are summarized in Table 5.4. The magnitude of the product, $\hat{D}_i P_i$, suggests that groups G1, G3, and G4 are the main contributors to the long-term fatigue damage. Note that in order to compare with other example cases discussed later, the total number of time series for the i^{th} group, n_i, used to estimate λ_i and ζ_i for each group is also included in Table 5.4 (note that $n_i = N_i \times$ the number of available sensors). The long-term fatigue damage rate (per year), D_L, is expressed as a finite sum of lognormal random variables; it does not have a closed-form or standard distribution function but a non-parametric distribution can be easily established. For instance, results obtained using Monte Carlo simulation with 10^6 samples are summarized in Table 5.5. They suggest that the upper bound of the 95% CI of D_L is about 15 times that of its lower bound, and that the median value of D_L is close to the long-term fatigue damage rate (per year), D_{meas}, based entirely on measurements at the location of interest which is easily calculated as:

$$D_{meas} = \sum_{i=1}^{N_G} D_{i,meas} \cdot P_i; \quad D_{i,meas} = \frac{1}{N_i} \sum_{j=1}^{N_i} D_{meas,i}(j) \tag{5.6}$$

where $i = 1$ to N_G, $j = 1$ to N_i, $\sum_{i=1}^{N_G} N_i = N_T$, and $\sum_{i=1}^{N_G} P_i = 1$

Note that $D_{meas,i}(j)$ is the fatigue damage rate calculated based on the measured strains at the location of interest (here, sensor no. 5) for the j^{th} event in the i^{th} group. Note, too, that although the probabilities in Table 5.4 only sum to 5%, we have assumed that for the remaining 95% of the time, damage is negligible. Results presented should be interpreted with this understanding. In this example, we assume that the design life of the riser, T_d, is 25 years; the probability of failure over this time, as estimated by the use of Monte Carlo simulation with 10^6 samples, equals 1.8×10^{-3}, as indicated in Table 5.5.

Table 5.4: Parameters of the empirical model for the long-term fatigue damage rate estimation at the location of interest in the case of eight sensors.

	$\hat{D}_i$	$P_i(\%)$	λ_i	ζ_i	n_i
G1 ($i = 1$)	1.74	0.05	0.10	1.09	192
G2 ($i = 2$)	1.25×10^{-3}	4.50	0.24	0.97	56
G3 ($i = 3$)	0.40	0.35	-0.07	1.07	88
G4 ($i = 4$)	0.82	0.10	0.09	1.09	48

Table 5.5: Estimated and measured long-term fatigue damage rate per year and the probability of fatigue failure at the location of interest in the case of eight sensors.

D_L ($\times 10^{-3}$)		D_{meas} ($\times 10^{-3}$)	P(failure)
95% CI	Median		
[1.2, 17.9]	4.2	3.3	1.8×10^{-3}

The long-term fatigue damage rate at any location over the entire length of the riser can be similarly estimated (as illustrated above for one location) and compared with the long-term fatigue damage rate based entirely on measured values at the same location, without need for WWA application. As shown in Fig. 5.5, for various locations along the riser, the median value and the 95% CI of the estimated long-term fatigue damage rate per year are represented by the solid line and the dashed lines, respectively. The long-term fatigue damage rate based entirely on measured values at the locations of the eight input sensors and at the previously assumed key location of interest (sensor no. 5) are denoted by asterisks and an open circle, respectively. Strains were also measured at 15 other locations but these sensors were never used in the estimation process; they serve as "check points" and are represented by dots. These check points are to be understood as similar to the previous key location of interest (sensor no. 5) in that they are never used in reconstruction of strains anywhere (only the eight input sensors shown with asterisks in Fig. 5.2 are). Figure 5.5 shows that generally the median values of the estimated long-term fatigue damage rate are close to the damage rate based on directly measured values at those discrete locations; somewhat higher fatigue damage rates are indicated near the high-current end (i.e., where the current speed is highest in the case of the linearly sheared current cases).

5.3 Discussion and Sensitivity Studies

The long-term fatigue damage rate for various locations over the entire length of the riser as well as at the assumed key location of interest (sensor no. 5) were estimated by using strains measured at eight sensors. We repeat these computations with different assumptions in order to study the influence of the number of sensors and the number of events on fatigue damage rate estimation.

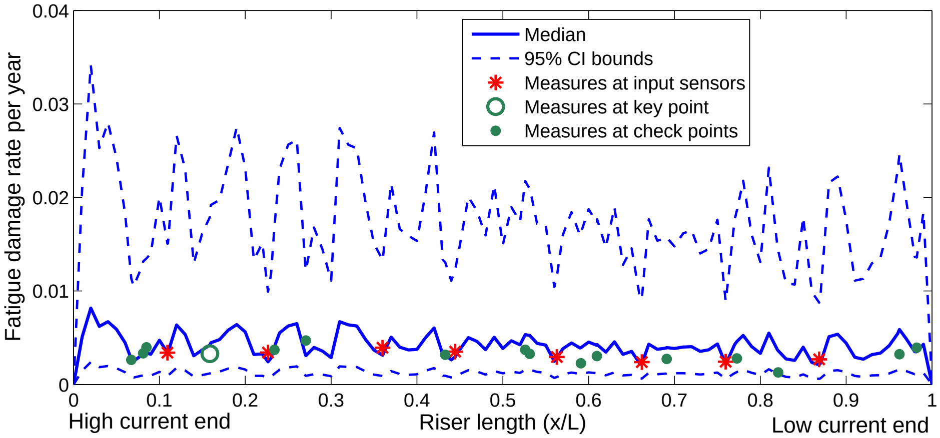

Figure 5.5: Estimated and measured long-term fatigue damage rate per year for various locations over the entire length of the riser in the case of eight sensors.

5.3.1 Effect of Number of Sensors

We assume that twenty-three sensors (all, except sensor no. 5) are available as input sensors. The grouping of events and the probability of occurrence of each group are assumed to be the same as in the previous case with eight input sensors. The long-term fatigue damage rate at various locations over the entire length of the riser is estimated in the same manner as was done before. The prediction at the same location of interest (sensor no. 5) is compared with that of the previous case (eight input sensors). For the location of interest (key location), parameters of the empirical model are presented in Table 5.6 and fatigue damage rate estimates are presented in Table 5.7. Compared with the previous case (eight sensors), the point estimates of the fatigue damage rate, $\hat{D}_i$, for groups G1 and G4, are larger when twenty-three input sensors are available, while that for group G3 is somewhat smaller. The net effect is that the median value of the long-term fatigue damage rate is slightly reduced (from 4.2×10^{-3} to 3.4×10^{-3}). More importantly, the WWA-related response reconstruction uncertainty, represented by ζ_i, is smaller with the larger number of sensors (and, hence, samples). This narrows the 95% CI on the long-term fatigue damage at the location of interest; the upper bound is only about 8 times as large as the lower bound now. Hence, the probability of failure also reduces to 5.6×10^{-5} from 1.8×10^{-3}. The long-term fatigue damage rate estimated for various locations over the entire length of the riser, as presented in Fig. 5.6, shows that generally the width of the 95% CI on the estimations is much narrower than in the previous case with eight input sensors. The maximum fatigue damage rates are again found to occur closer to the high-current end, with a general trend of decreasing fatigue damage rates towards the low-current end. One reason for this trend is that the sheared current profiles have increasing current speeds at the high-current end. This trend might also indicate that the influence of traveling waves, which are generated at the high-current end and dissipated while traveling towards the low-current end, is likely being captured by the WWA reconstruction.

Table 5.6: Parameters of the empirical model for the long-term fatigue damage rate estimation at the location of interest in the case of twenty-three sensors.

	$\hat{D}_i$	$P_i(\%)$	λ_i	ζ_i	n_i
G1 ($i = 1$)	2.66	0.05	0.18	0.74	552
G2 ($i = 2$)	8.78×10^{-4}	4.50	0.18	0.88	158
G3 ($i = 3$)	0.24	0.35	0.25	0.84	246
G4 ($i = 4$)	1.40	0.10	0.34	0.93	132

Table 5.7: Estimated and measured long-term fatigue damage rate per year and the probability of fatigue failure at the location of interest in the case of twenty-three sensors.

D_L $(\times 10^{-3})$ 95% CI	D_L $(\times 10^{-3})$ Median	D_{meas} $(\times 10^{-3})$	P(failure)
[1.3, 10.0]	3.4	3.3	5.6×10^{-5}

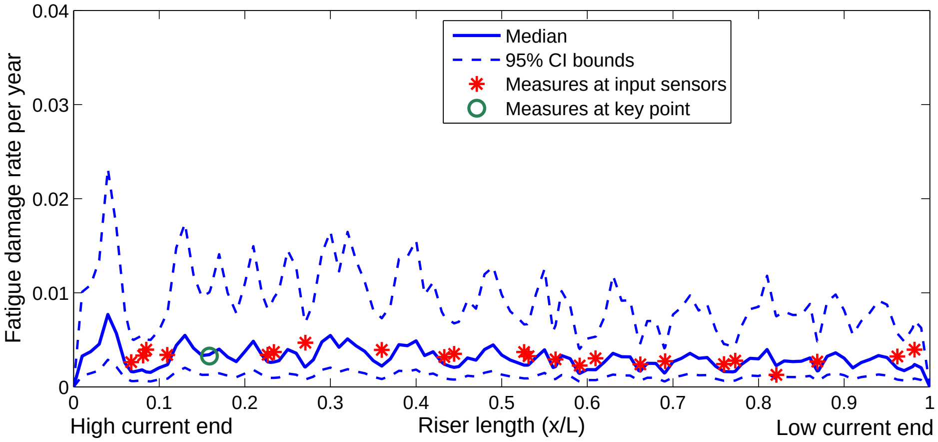

Figure 5.6: Estimated and measured long-term fatigue damage rate per year for various locations over the entire length of the riser in the case of twenty-three sensors.

5.3.2 Effect of Number of Events

We again assume that the same eight sensors (as in Fig. 5.2) are available, but now we assume that group G1 contains only six events, instead of 24. These six events are carefully chosen to cover the entire range of current speeds as the 24 events cover. The other three current profile groups (G2, G3, and G4) are assumed to remain unchanged. The probability of occurrence of each group is also assumed to remain unchanged. With this reduced number of events in G1, the long-term fatigue damage rate for various locations over the entire length of the riser is estimated using measurements from the eight input sensors; results are summarized in Fig. 5.7. Generally, even with this reduced data set, the estimated median values of the fatigue damage rate match those based directly on measurements reasonably well. To illustrate the effect of the number of events, the long-term fatigue damage rates estimated, while group G1 is assumed to include only six events, are plotted against those where group G1 includes all twenty-four events. In Fig. 5.8, the median values and the bounds on the 95% CI of the estimated long-term fatigue damage rates are plotted; the solid lines represent the case where group G1 contains twenty-four events and the dashed lines represents the case where G1 contains six events. In general, the fatigue damage rate variation indicates comparable estimates as well as comparable spatial patterns in the two cases. At a few locations, e.g., around $x/L \approx 0.25$, the 95% CI based on the smaller number of events is much wider than that based on the larger number of events; this is as expected since the smaller number of events in a group generally implies greater variability in fatigue damage estimates associated with that group. Note that since the long-term fatigue damage rate estimate at a specified location depends on contributions from all the current profile groups involved, the influence of changed assumptions for events in any one group has limited influence on the overall fatigue damage. Note too that a study on the influence of the number of events is instructive—in a real field monitoring campaign, new data that are recorded will first be assigned to a current profile group class or classes and then these new events will lead to updates on point estimates and variability in damage rate estimation for one or more groups. This study provides an empirical procedure to maintain updated information on the state of critical fatigue details on a riser as new data are recorded.

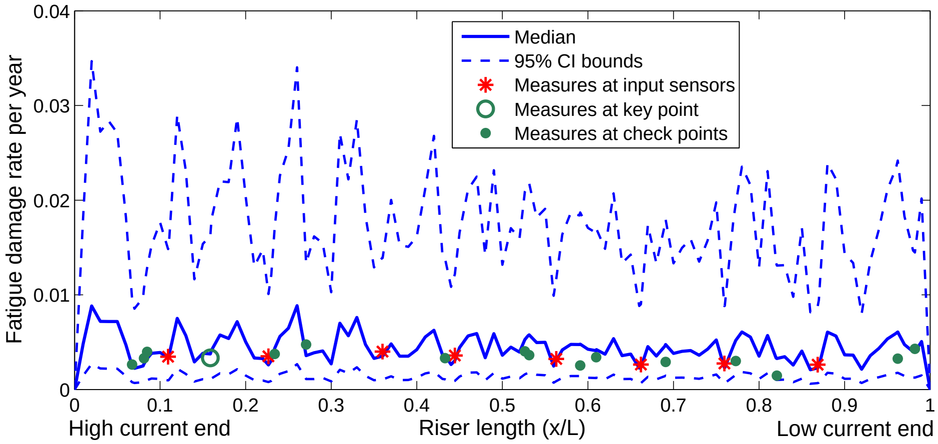

Figure 5.7: Estimated and measured long-term fatigue damage rate per year for various locations over the entire length of the riser in the case of eight sensors and assuming group G1 contains six events.

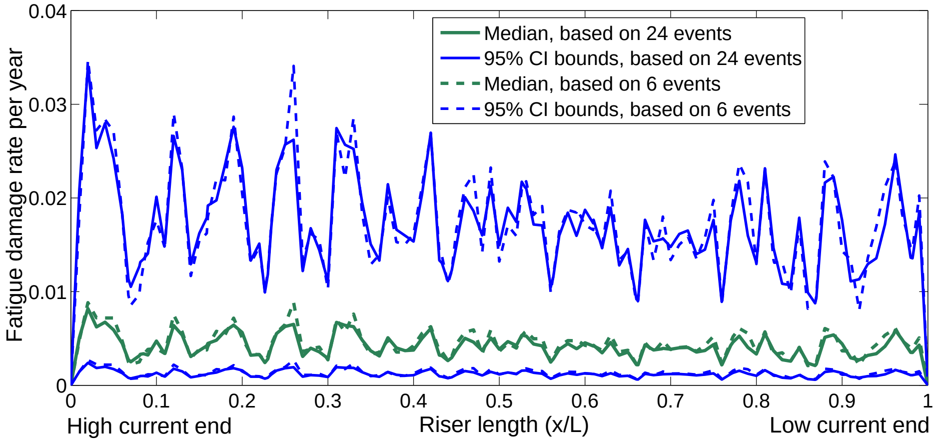

Figure 5.8: Estimated long-term fatigue damage rate per year over the entire length of the riser in the case of eight sensors—a comparison for when group G1 includes 6 events versus 24 events.

5.4 Conclusions

In this study, an empirical procedure, referred to as Weighted Waveform Analysis (WWA), was employed as part of a framework for long-term fatigue damage assessment and life prediction of instrumented marine risers that undergo vortex-induced vibration. The framework relies on first classifying all recorded data sets (or events) from the field monitoring campaign on the basis of contrasting metocean current groups. The probability of occurrence of each current group is assumed to be available from separate metocean studies. For each recorded event, this fully empirical WWA method is employed to assess the fatigue damage at any critical fatigue detail of interest along the length of the riser. The uncertainty or variability associated with the WWA method, with the use of a limited number of sensors, and with any other factors is also assessed using cross-validation which involves using WWA to reconstruct the response at target sensor locations where measurements are available (while the target itself is hidden and not used) and assessing the error in such reconstruction. After adjusting for uncertainty, the long-term fatigue damage at the critical location of interest is estimated by considering all recorded events, the current groups they belong to, and the likelihood of occurrence of each group. To demonstrate application of the framework, we used the NDP bare-riser model data sets to provide VIV events of interest. Using four simulated current groups, assuming eight sensors were available on the riser, and with the help of 48 recorded events, fatigue damage estimates were computed for various points along the riser. In addition, sensitivity studies were conducted to study the influence of the number of sensors and the number of events on fatigue damage rate prediction. The results showed that the proposed framework can be conveniently used to predict the long-term fatigue damage and remaining life of risers using only field measurements. The results also showed that the framework can easily accommodate new data as they become available and can, thus, provide useful fatigue damage estimate updates for the riser.

Chapter 6

Summary and Conclusions

6.1 Overview of Research Objectives

The work presented in this dissertation provides empirical approaches to predict long-term damage rates and life (associated with fatigue due to vortex-induced vibration (VIV)) for marine risers, based on measurements of riser response and accompanying current flow fields. In order to gain an understanding of VIV and associated fatigue damage, risers are often instrumented in field monitoring campaigns wherein the dynamic response in the form of strains and/or accelerations is recorded at several discrete locations along the length of the riser. Often, simultaneously, current velocity profiles at a nearby location are also recorded. The oil and gas industry has generally relied on analytical tools for VIV-related fatigue damage predictions for a riser subjected to specified current profiles. Most analytical and semi-empirical approaches rely on the use of a finite element model of the riser and simplifying assumptions on both the flow conditions and on the response characteristics. As an alternative, when field monitoring is undertaken, we demonstrated that we can employ empirical procedures (using a limited number of measurements) to estimate the fatigue damage rate at the locations where fatigue details are of interest on the instrumented riser. The fatigue damage rate associated with each recorded event (under specified current flow conditions) is called a "short-term" fatigue damage rate. The uncertainty in empirically estimated short-term fatigue damage rates can be assessed. Then, "long-term" fatigue damage rates can be estimated by integrating short-term fatigue damage rates over each current type, while making suitable and necessary corrections for uncertainty.

Such an empirical approach for fatigue damage and life estimation has some advantages over analytical or semi-empirical approaches in common use. First, only measured strain and/or acceleration data are required; neither physical properties of the riser nor simplifying assumptions on current profiles is needed. Second, the data and, thus, the empirical approach, explicitly accounts for the different response characteristics and the different current profiles experienced by the riser. Third, such fatigue damage and life estimation is easily updated as more data become available from continuing field monitoring campaigns.

6.2 Principal Contributions from Each Chapter

This dissertation consists of three major parts. In the first part, complex characteristics of the VIV response of long flexible marine risers were studied. In the second part, different empirical procedures were employed to reconstruct riser response and then estimate fatigue damage rate using data measured by a limited number of sensors. In the final part, the methodology for empirical long-term fatigue damage prediction for an instrumented marine riser was demonstrated. In the following, the principal contributions from each chapter are listed.

6.2.1 Characteristics of VIV Response of Long Flexible Marine Risers

In Chapter 2 of this dissertation, complex characteristics of VIV response experienced by long flexible marine risers are visualized and examined by spectral and other techniques applied to data obtained from the NDP bare-model riser experiments. Higher harmonics, non-stationary characteristics, variation in frequency content of the response, and traveling wave patterns are discussed.

Power spectral density (PSD) plots of acceleration/strain signals reveal the presence of strong higher harmonics in the VIV response of the model riser. A linear relationship is observed, as expected, between the frequencies of each harmonic mode and the input current speed; the proportionality constant estimated using least-squares fits shows that the Strouhal number associated with long flexible cylinders is smaller than that estimated from stationary cylinder experiments.

The temporal evolution and spatial variation of displacement orbits show that the VIV response of long flexible cylinders can be non-stationary and complex. Mathematical tools such as the Hilbert transform and the wavelet transform are useful to study complex characteristics of the VIV response. Using the Hilbert transform, instantaneous amplitudes and phase angles (associated with displacement orbits) can be estimated from measured cross-flow and in-line displacements; these can then be used to examine non-stationary characteristics of the riser response. Scalograms (describing squared coefficients of wavelet transforms) of measured acceleration or strain signals help to reveal the presence and variation of different harmonics in the riser response.

Traveling wave patterns are also observed in the VIV response, albeit with different characteristics for uniform versus sheared currents. In addition, we demonstrate how the added mass coefficient may be estimated from a traveling wave's propagation speed.

These various complex characteristics evident in measurements should be taken into account, if possible, in any response reconstruction or fatigue damage prediction studies on risers undergoing VIV.

6.2.2 Empirical Procedures for Fatigue Damage Rate Estimation

In Chapter 3 of this dissertation, different empirical fatigue damage estimation methods are tested on data sets comprising strains measured on the NDP model riser subjected to uniform and sheared currents. Five empirical methods were studied—they include Weighted Waveform Analysis (WWA), Modified WWA, Proper Orthogonal Decomposition (POD), Modal Phase Reconstruction (MPR), and a hybrid method that combines MPR and modified WWA. For each method, the theoretical formulation was first presented briefly and then its application was illustrated by an example wherein a single sensor was selected as the target sensor and, by using measurements from the remaining twenty-three sensors as inputs, the riser response was reconstructed at the location of the target sensor. The fatigue damage rate estimated using the reconstructed riser response was compared with the value based directly on the measurements at that target. The ratio of the estimated fatigue damage to that based on direct measurements there was used as an indicator of the accuracy of each empirical method. Two separate summary studies—one involving a larger number of available sensors on the riser (twenty-three) and another involving a small number (eight)—were carried out and estimated fatigue damage rates over the entire length of the NDP model riser were computed and the results discussed.

Based on the numerical studies presented, some concluding remarks follow:

(i) With careful selection of the riser modes for inclusion, the WWA method has the ability to preserve higher harmonics in the reconstructed riser response since the selected modes in the method are non-sequential. Because the modal weights are solved for at each time instant, non-stationary characteristics, if present, are inherently included in response reconstruction with this method. The WWA method works particularly well if only a small number of sensors are available and it relies on assumed mode shapes that are based on knowledge of the physical properties of the riser. The computation with the WWA method is fast.

(ii) The modified WWA method can account for the influence of higher harmonics as long as a large number of sensors are available. This method is more versatile in accounting for the effect of traveling waves than the WWA method. As with the WWA method, non-stationary characteristics are inherently account for, but this method is not well-suited for cases where only a small number of sensors are available since a greater number of modal weights need to be estimated than with WWA. The modified WWA method relies on assumed mode shapes and the computation is fast.

(iii) The POD method preserves frequency components and higher harmonics in the reconstructed riser response by empirical decomposition of the spatio-temporal data. POD relies only on data; the method identifies empirical mode shapes directly from data, without the need for physical properties of the riser. The POD scheme is the fastest among the five methods discussed in Chapter 3; however, it does not account for non-stationary response characteristics. The method is not well-suited for situations where only a small number of sensors is available because of inaccuracies in the reconstructed response that arise due to the need for interpolation or extrapolation.

(iv) As is the case for the POD method, the MPR method accounts for higher harmonics in the response and only relies on data, not on physical properties of the riser to estimate complex riser modes. MPR, however, is not well-suited for situations where the riser response exhibits strong non-stationary characteristics or when only a small number of sensors is available. The computation with the MPR method is more involved than with other methods such as WWA and POD. Importantly, MPR explicitly accounts for traveling waves in decomposing the measured response.

(v) The hybrid method (which combines the MPR and modified WWA methods) has the ability to account for higher harmonics and the effect of traveling waves; it works well even if only a small number of sensors are available. The hybrid method does not explicitly take into consideration non-stationary response characteristics, but the reconstruction even with fairly strong non-stationary response is superior to that with the POD and MPR methods. The hybrid method needs to assume modes in the second step of estimating modal weights for the derived complex MPR modes. Although the hybrid method is the slowest due to the greater computational effort relative to the other methods, it is the most accurate both for a large or small number of input sensors.

6.2.3 A Data-Driven Mode Identification Algorithm for Fatigue Damage Assessment

In Chapter 4 of this dissertation, the WWA procedure was improved in that the mode or waveform selection procedure was changed to require no assumptions on added mass coefficient and no information on riser physical properties. The fundamental natural frequency of the riser is estimated through separate estimation in turn of (i) the dominant riser response frequency through temporal data analysis—specifically, Fourier spectral analysis of the riser response; and (ii) the dominant wavenumber through spatial data analysis—specifically, Lomb-Scargle spectral analysis of the spatial covariance variation with sensor spacing. Then, mode selection for WWA follows by identifying riser mode numbers that line up with peaks in response power spectra. The relevant mathematical background for this less commonly used wavenumber identification procedure and its application were discussed briefly. By employing the improved WWA method on four NDP data sets, fatigue damage rates at various locations along the riser length were estimated using measurements from twenty-three sensors as inputs. These estimates were cross-validated against fatigue damage rates computed directly from measurements at the same (target) locations. The fatigue damage rates estimated from the improved WWA method were compared with those from the original WWA method. Results showed that, even without employing any information on the physical properties of the riser or any assumptions on added mass coefficients, the improved WWA method can estimate fatigue damage rates quite accurately from a limited number of strain measurements. The proposed wavenumber identification procedure may also be used to estimate the spatio-temporal averaged values of the added mass coefficient directly from the data and, thus, the method offers a possible approach for detailed studies of the relationship between the added mass coefficient and current velocity profiles, especially for long flexible risers.

6.2.4 Long-Term Empirical Prediction of Fatigue Damage

In Chapter 5 of this dissertation, we describe an empirical procedure for long-term fatigue damage assessment and life prediction of instrumented marine risers undergoing vortex-induced vibration. This procedure is demonstrated by using Weighted Waveform Analysis (WWA) with the NDP experimental data sets.

The framework relies on first classifying all recorded data sets (or events) from the field monitoring campaign on the basis of contrasting metocean current groups. The probability of occurrence of each current group is assumed to be available from separate metocean studies. For each recorded event, this fully empirical WWA method is employed to assess the fatigue damage at any critical fatigue detail of interest along the length of the riser. The uncertainty or variability associated with the WWA method, with the use of a limited number of sensors, and with any other factors is also assessed using cross-validation which involves using WWA to reconstruct the response at target sensor locations where measurements are available (while the target itself is hidden and not used) and assessing the error in such reconstruction.

After adjusting for uncertainty, the long-term fatigue damage at the critical location of interest is estimated by considering all recorded events, the current groups they belong to, and the likelihood of occurrence of each group.

To demonstrate application of the framework, we used the NDP bare-riser model data sets to provide VIV events of interest. Using four simulated current groups, assuming eight sensors were available on the riser, and with the help of 48 recorded events, fatigue damage estimates were computed for various points along the riser. In addition, sensitivity studies were conducted to study the influence of the number of sensors and the number of events on fatigue damage rate prediction. The results showed that the proposed framework can be conveniently used to predict the long-term fatigue damage and remaining life of risers using only field measurements. The results also showed that the framework can easily accommodate new data as they become available and can, thus, provide useful fatigue damage estimate updates for the riser.

6.3 Suggestions for Future Research

In this dissertation, we have developed alternative empirical methods for the estimation of fatigue damage rates at any location of interest on an instrumented marine riser where strains are measured at a limited number of locations. In addition, an approach for prediction of the empirical long-term fatigue life of the instrumented marine riser was established. This approach is based entirely on measured data; thus, intrinsic (possibly, complex) riser response characteristics resulting from different current flow fields are directly accounted for. In addition, uncertainty in fatigue damage estimations associated with the use of the empirical method for response reconstruction and with measurements are accounted for in the long-term predictions.

The development of this dissertation raises some questions which are relevant to discuss here since they are unresolved at the time of this writing. A few of these are briefly enumerated below.

1. In this study, strains measured by eight sensors in various spatial array arrangements are used to empirically reconstruct riser response over the entire span. Results show that with the Weighted Waveform Analysis (WWA) method, the distribution of the eight sensors so that they cover a large portion of the riser generally provides better response reconstruction than the use of eight clustered sensors. However, it would be useful to establish a quantitative criterion for an optimal sensor arrangement using a metric based on accuracy of the response reconstruction and fatigue damage estimation. Cross-validation, as used in this dissertation, may be employed in such a study.

2. In this study, sine functions were selected as basis functions (eigenfunctions) for the WWA method. This is reasonable because the natural mode shapes for the NDP model riser are close to sine functions. However, other functions, such as orthogonal polynomials, may be selected as basis functions and their applications with the WWA method for response reconstruction could be tested. Such alternative mode shapes may, in general, be needed for different riser end/boundary conditions. Even with known end conditions, alternative mode shapes might need to be derived that allow for local variations along the riser length that arise

due to, say, buoyancy modules; simple sine-like functions likely cannot capture local spatial features effectively.

3. Proper Orthogonal Decomposition (POD) proved to be an efficient technique to extract the most energetic modes directly from a suite of spatio-temporal data; no assumptions about the riser's physical properties are needed. Efficient interpolation of these discrete POD modal coordinates or mode shapes is needed, however, to make POD more appealing in riser response reconstruction.

4. The proposed empirical approach for the estimation of short-term fatigue damage rates and the prediction of long-term fatigue life of an instrumented marine riser was demonstrated to be quite efficient with data from model experiments. The capabilities of this framework for empirical fatigue life prediction would be better demonstrated by application to measurements from full-scale riser field monitoring campaigns. Continuous updating of damage and life estimation can also be demonstrated by real-time augmenting of new data as they become available.

Appendices

Appendix A

Norwegian Deepwater Programme High Mode VIV Experiment and Data Sets

The Norwegian Deepwater Programme (NDP) high mode VIV experiment was carried out by the Norwegian Marine Technology Research Institute (Marintek) in 2003, by horizontally towing a flexible cylinder (model riser) in the Ocean Basin test facility. The Ocean Basin is 50 m wide, 80 m long, and 10 m deep. The cylinder was made of fiberglass with an outer diameter of 27 mm, a wall thickness of 3.0 mm, and a length of 38 m. The length-to-diameter (L/D) ratio is about 1,400, which is close to the range of the L/D ratios of most drilling risers. By towing both ends of the cylinder at the same speed or by towing one end while holding the other end fixed, two types of current profiles—uniform or linearly sheared current profiles—were simulated. A bare-riser model and models with two types of strakes attached (for VIV mitigation) with different spatial coverage ratios were tested; a total of 341 data sets were generated. The objectives of the model test program were: (i) to improve the understanding of high-mode VIV response of flexible risers and associated fatigue damage; and (ii) to assess the effectiveness of the strakes in VIV mitigation [10].

The main objective of this dissertation is to establish a methodology to empirically predict the long-term fatigue damage rate of marine risers caused

Table A.1: NDP bare-riser data sets.

Current profiles	Max. current speed U_{max}(m/s)	Number of data sets
Uniform	0.3 - 2.4 (in steps of 0.1 m/s)	22
	1.0, 2.0 (additional)	2
Sheared	0.3 - 2.4 (in steps of 0.1 m/s)	22
	1.0, 2.0 (additional)	2
	Total	48

by VIV. Riser displacements and strains measured on the straked risers were significantly reduced compared with those on the bare riser [10]; thus, the fatigue damage caused by VIV was likely significantly reduced as well for the straked risers. Hence, the research documented in this dissertation is focused on the data sets obtained from the bare-riser model. There are 48 bare-riser data sets; the test matrix is presented in Table A.1.

Riser response was measured using 24 strain sensors (one sensor failed for some test runs; hence, in some cases, only 23 strain sensors were available) and 8 accelerometers for the cross-flow (CF) direction; similarly, in the in-line (IL) direction, measurements from 40 strain sensors and 8 accelerometers were available. Sensor locations are illustrated in Fig. A.1. Note that, at 8 points on the riser, both strains and accelerations in the CF and IL directions were measured; also, at 24 locations, strains in both the CF and IL directions were measured. All analyses are performed over a selected time window matching the measured time series of strains, accelerations, and displacements. This time window is based on the towing velocity of the riser; it was selected to remove transient effects in the data [10]. As illustrated in Fig. A.2, the total

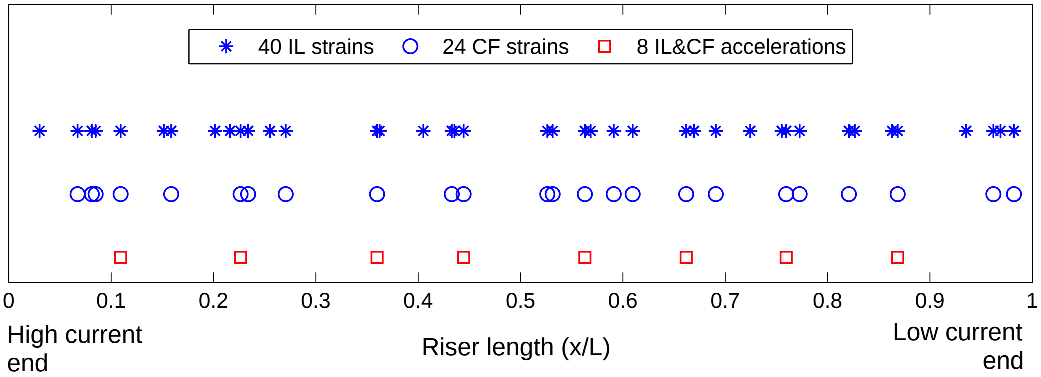

Figure A.1: Sensor locations in the in-line and cross-flow directions.

length of the time series for the NDP2350 data set is about 90 seconds; only the part included in the time window (colored in red) is selected for any analysis. Generally, for all the 48 bare-riser data sets, more than 100 cycles of vibrations are ensured within the selected time window. In this study, the length of record/data refers to the length of the relevant time window. In Fig. A.2, the figure at the top depicts the tension force along the towing direction measured at the towing end; the figure in the middle depicts the tension force along the riser axis direction measured at the towing end; and the figure at the bottom depicts the towing velocity measured at the towing end (i.e., the maximum current speed encountered by the model riser). Note that "negative" tension forces are only due to the sign convention employed.

Among the 341 data sets in total, six of them are publicly available at the VIV Data Repository [11]. This study utilized these public-domain data sets as example cases to illustrate details of the various empirical procedures in this dissertation; however, conclusions and discussions in this dissertation

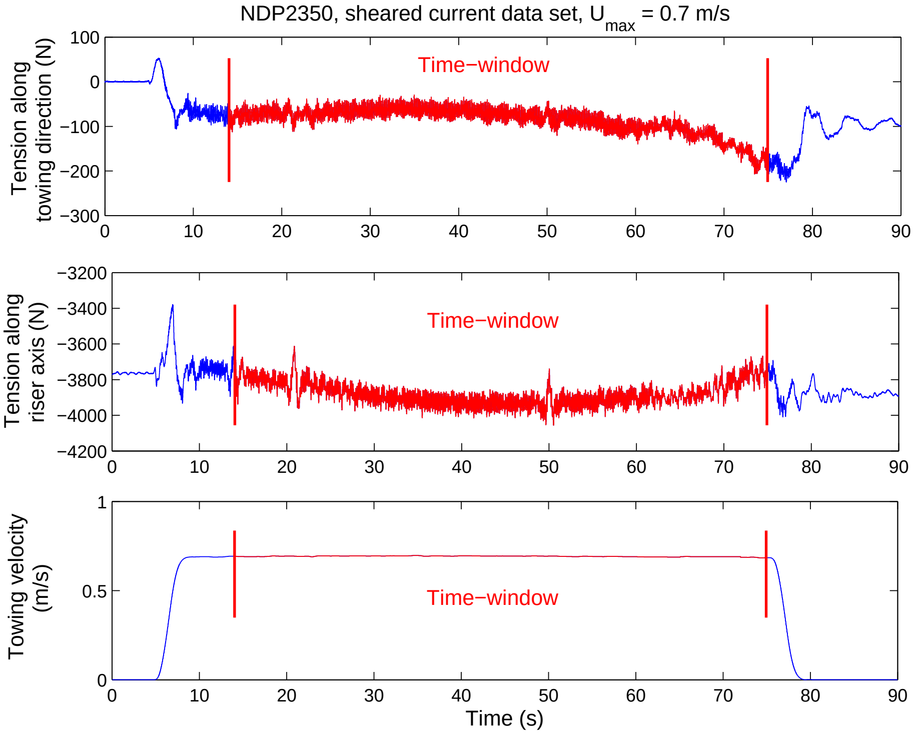

Figure A.2: Example identification of a time window for the NDP2350 (sheared current) data set with maximum current speed of 0.7 m/s.

are drawn based on analysis of all the 48 available bare-riser data sets.

Table A.2 summarizes the current profile types and RMS (root-mean-square) vales of the CF displacement normalized with respect to the diameter, D, of the cylinder for the six public-domain data sets. As illustrated, the RMS displacement values that were computed from the four bare riser data sets are relatively large; this response is assumed to be associated with VIV. In contrast, the oscillations are effectively suppressed by the attached strakes for the two straked risers; thus, their RMS displacement values are very small.

Table A.2: The six publicly available NDP data sets.

Event no.	Riser type	Current profile	Max. current speed (m/s)	Largest RMS CF-disp./D	Time window (s)
2120	Bare	Uniform	1.4	0.441	25
2150	Bare	Uniform	1.7	0.402	18
2350	Bare	Sheared	0.7	0.417	60
2420	Bare	Sheared	1.4	0.371	27
3050	Straked	Uniform	0.7	0.003	56
3120	Straked	Uniform	1.4	0.002	25

Table A.3: Physical properties of the NDP model riser.

Length (m)	38
Outer diameter (mm)	27
Wall thickness (mm)	3
Mass per unit length (kg/m)	0.933
Displaced water per unit length (kg/m)	0.576
Mean effective tension (N)	4000 to 6000
Bending Stiffness (N-m^2)	598.8

Note that, in Table A.2, the RMS CF displacement reported is based on the entire length of record and the largest value from all the eight accelerometer loggers is presented.

The important physical properties of the NDP model riser are listed in Table A.3. Additional details on the NDP experiments that relate to the test setup, other physical properties of the model riser, and the effectiveness of strakes in VIV suppression may be found in the work of Braaten and Lie [10] and Trim et al. [54].

Appendix B

Hilbert Transform and Analytic Signal

The Hilbert transform of a real-valued function, $x(t)$, is a another real-valued function, denoted by $H\{x(t)\}$, which can be defined and understood in two ways [6].

(i) *Definition as Convolution Integral*

The Hilbert transform of $x(t)$ is defined as:

$$H\{x(t)\} = \frac{1}{\pi}\int_{-\infty}^{\infty}\frac{x(\tau)}{t-\tau}\,\mathrm{d}\tau \tag{B.1}$$

Thus the Hilbert transform of $x(t)$ is equivalent to the convolution integral of $x(t)$ and $1/\pi t$, written as:

$$H\{x(t)\} = x(t) * \left(\frac{1}{\pi t}\right) \tag{B.2}$$

(ii) *Definition as $\pi/2$ Phase-Shift System*

Take the Fourier transform of both sides of Eq. B.2 and describe the Hilbert transform in the frequency domain as follows:

$$F\{H\{x(t)\}\} = F\{x(t)\}\cdot F\left\{\frac{1}{\pi t}\right\} = \begin{cases} X(f)\cdot e^{-i\pi/2} & \text{if } f>0 \\ X(f)\cdot e^{i\pi/2} & \text{if } f<0 \end{cases} \tag{B.3}$$

where $F\{\}$ is the Fourier transform operator, and the Fourier transform of $x(t)$ is denoted as $X(f)$, i.e., $F\{x(t)\} \equiv X(f)$. Equation B.3 indicates two important properties of the Hilbert transform. First, the Hilbert transform affects the phase of the original signal in a way that depends on the sign of its frequency, i.e., it shifts the phase $-\pi/2$ for positive frequencies and by $\pi/2$ for negative frequencies. Second, the Hilbert transform does not affect the amplitude of the original signal. For example, if $x(t)$ is a cosine function, its Hilbert transform is a sine function; and if $x(t)$ is a sine function, its Hilbert transform is a negative cosine function.

The analytic signal of a real-valued function, $x(t)$, can be constructed using its Hilbert transform and is expressed as:

$$z(t) = x(t) + iH\left\{x(t)\right\} \tag{B.4}$$

Rewriting Eq. B.4 in terms of complex polar coordinates, we have:

$$z(t) = A(t)e^{i\varphi(t)} \tag{B.5}$$

where $A(t)$ and $\varphi(t)$ are the envelop (amplitude) function and the phase function, respectively, of the original real-valued function, $x(t)$. They are defined as follows:

$$A(t) = \sqrt{z(t) \cdot z^*(t)}; \quad \varphi(t) = \arctan \frac{Imag\left\{z(t)\right\}}{Real\left\{z(t)\right\}} \tag{B.6}$$

where $z^*(t)$ is the complex conjugate of the complex-valued function, $z(t)$; also, $Imag\left\{z(t)\right\}$ and $Real\left\{z(t)\right\}$ are the imaginary and real parts, respectively, of $z(t)$.

Appendix C

Morlet Wavelet Transform

Give a function, $x(t)$, the wavelet transform, $W(s,t)$, is obtained through the convolution of $x(t)$ with a shifted and scaled parent wavelet function, $\Psi(t)$, as follows [30]:

$$W(s,t) = \frac{1}{\sqrt{s}} \int_{-\infty}^{\infty} x(\tau)\Psi^{*}\left(\frac{t-\tau}{s}\right) \mathrm{d}\tau \tag{C.1}$$

where the symbol * denotes complex conjugate; translation, τ, indicates the central location of the wavelet (window) function; and scale, s, is inversely proportional to frequency. By choosing different scale values, we can achieve different resolutions for the different frequency components of the signal—e.g., we can use a larger scale to ensure a finer resolution for lower frequencies and a smaller scale to permit a coarser resolution for higher frequencies. The wavelet coefficient, $W(s,t)$, gives an indication (or a measure) of the similarity between the wavelet function, $\Psi((t-\tau)/s)$, and the function of interest, $x(t)$, at time, t, and scale (frequency), s.

In this study, we use the Morlet wavelet as the parent wavelet function, because it is analogous to the Fourier transform which makes it convenient for harmonic analysis. In such analysis, the wavelet functions used in Eq. C.1 are the shifted and scaled version of the "parent" function. The Morlet wavelet function is expressed as follows:

$$\Psi(t) = e^{-t^2/2} e^{i2\pi f t} \tag{C.2}$$

Equation C.2 indicates that the Morlet wavelet is a Gaussian-windowed Fourier transform, with harmonics oscillating at the frequency, f.

Appendix D

Probability Plot Correlation Coefficient Test

The probability plot correlation coefficient (PPCC) test calculates the correlation coefficient, r, between the ordered data, x_i, and the corresponding fitted quantiles, Q_i, as follows [18]:

$$r = \frac{\sum_{i=1}^{n}(x_i - \bar{x})(Q_i - \bar{Q})}{\sqrt{\sum_{i=1}^{n}(x_i - \bar{x})^2 \sum_{i=1}^{n}(Q_i - \bar{Q})^2}} \tag{D.1}$$

where $\bar{x}$ and $\bar{Q}$ are the sample mean values of the data, x_i, and the fitted quantiles, Q_i, respectively, where n refers to the number of data. The correlation coefficient, r, quantitatively measures the linearity of the probability plot; and it is assumed that the closer r is to unity, the more likely it is that the data, x_i, are drawn from the fitted distribution.

In the special case of the normality test, Q_i is the median value of the standard normal order statistics, which is calculated as:

$$Q_i = \Phi^{-1}(q_i) \tag{D.2}$$

where $\Phi^{-1}()$ is the inverse cumulative distribution function of a standard normal random variable and q_i is the plotting position. In this study, the plotting position is selected as [9]:

$$q_i = \frac{i - 0.375}{n + 0.25}; \quad 1 \leq i \leq n \tag{D.3}$$

The null hypothesis (H_0) is that the data, x_i, follow a standard normal distribution, and the alternative hypothesis (H_1) is that the data, x_i, do not follow a standard normal distribution. H_0 can be rejected in favor of H_1 at a significance level, α, if $r < r_\alpha(n)$. The critical value, $r_\alpha(n)$ is a function of the significance level, α, and the number of data, n; its value may be estimated using a regression equation obtained by Monte Carlo simulation as follows[21]:

$$\begin{aligned} \ln\left(\frac{1}{1-r_\alpha(n)}\right) =& 1.29 + 0.283\ln(\alpha) \\ &+ \left(0.887 - 0.751\alpha + 3.21\alpha^2\right)\ln(n) \\ &\text{for} \quad 0.005 \leq \alpha \leq 0.1 \end{aligned} \tag{D.4}$$

Appendix E

Kolmogorov-Smirnov (KS) Test

The Kolmogorov-Smirnov (KS) test quantifies the similarity between the empirical cumulative distribution function (CDF) of the observations (data) and a reference CDF, by calculating the largest absolute value of their difference as follows:

$$k = \max(|F(x) - G(x)|) \tag{E.1}$$

$F(x)$ is the empirical CDF based on the data, x, and $G(x)$ is the reference CDF.

For the normality test as conducted in this dissertation, $G(x)$ is a standard normal CDF. The null hypothesis (H_0) is that the data, x, follow a standard normal distribution, and the alternative hypothesis (H_1) is that the observations, x, do not follow a standard normal distribution. H_0 can be rejected in favor of H_1 at the significance level, α, if $k > k_\alpha$, where the critical value, k_α, is tabulated in several references or may be obtained using the built-in function, kstest, which is part of the MATLAB® software.

Bibliography

[1] D. Alleyne and P. Cawley. A Two-Dimensional Fourier Transform Method for the Measurement of Propagating Multimode Signals. *Journal of Acoustical Society of America*, 89:1159–1168, 1991.

[2] API. *RP 2RD-1998, Design of Risers for Floating Production Systems (FPSs) and Tension-Leg Platforms (TLPs).* American Petroleum Institute, 1998.

[3] G.S. Baarholm, C.M. Larsen, and H. Lie. On Fatigue Damage Accumulation from In-Line and Cross-Flow Vortex-Induced Vibrations on Risers. *Journal of Fluids and Structures*, 22:109–127, 2006.

[4] Y. Bai, R. Bhattacharyya, and M.E. McCormick. *Pipelines and Risers.* Elsevier Science Ltd, Oxford, UK, 2001.

[5] P.W. Bearman. Vortex Shedding from Oscillating Bluff Bodies. *Annual Review of Fluid Mechanics*, 16:195–222, 1984.

[6] J.S. Bendat and A.G. Piersol. *Random Data Analysis and Measurement Procedures.* A Wiley-Interscience Publication, New York, Third Edition, 2000.

[7] P. Beynet, R. Shilling, M. Campbell, E. Tellier, and H. Howells. Full Scale VIV Response Measurements of a Drill Pipe in Gulf of Mexico Loop Currents. In *27th International Conference on Offshore Mechanics*

and Arctic Engineering, OMAE 2008, Paper no. 57610, Estoril, Portugal, 2008.

[8] R.D. Blevins. *Flow-Induced Vibration.* Krieger Publishing Company, Malabar, Florida, Second Edition, 2001.

[9] G. Blom. *Statistical Estimates and Transformed Beta-Variables.* John Wiley and Sons, New York, 1958.

[10] H. Braaten and H. Lie. NDP Riser High Mode VIV Tests. Main Report No. 512394.00.01. Norwegian Marine Technology Research Institue, 2004.

[11] Center for Ocean Engineering, Massachusetts Institute of Technology. Vortex Induced Vibration Data Repository, 2007. `http://oe.mit.edu/VIV`.

[12] F. Chasparis, Y. Modarres-Sadeghi, F.S. Hover, M.S. Triantafyllou, M.A. Tognarelli, and P. Beynet. Lock-In, Transient and Chaotic Response in Riser VIV. In *28th International Conference on Ocean, Offshore and Arctic Engineering, OMAE 2009*, Paper no. 79444, Honolulu, USA, 2009.

[13] T.Y. Chung. *Vortex-Induced Vibration of Flexible Cylinders in Sheared Flows.* PhD Dissertation, Massachusetts Institute of Technology, Cambridge, MA, 1987.

[14] Jason Dahl. *Vortex-Induced Vibration of a Circular Cylinder with Combined In-Line and Cross-Flow Motion.* PhD Dissertation, Massachusetts Institute of Technology, Cambridge, MA, 2008.

[15] T. Dirlik. *Application of Computer in Fatigue Analysis.* PhD Dissertation, University of Warwick, Coventry, UK, 1985.

[16] M. Dixon and D. Charlesworth. Application of CFD for Vortex-Induced Vibration Analysis of Marine Risers in Projects. In *Proceedings of the Offshore Technology Conference*, Paper no. 18348, Houston, USA, 2006.

[17] S.D. Downing and D.F. Socie. Simple Rainflow Counting Algorithms. *International Journal of Fatigue*, 4:31–40, 1982.

[18] J.J. Filliben. The Probability Plot Correlation Coefficient Test for Normality. *Technometrics*, 17 (1):111–117, 1975.

[19] W.R. Frank, M.A. Tognarelli, S.T. Slocum, R.B. Campbell, and S. Balasubramanian. Flow-Induced Vibration of a Long, Flexible, Straked Cylinder in Uniform and Linearly Sheared Currents. In *Proceedings of the Offshore Technology Conference*, Paper no. 16340, Houston, USA, 2004.

[20] K. Grosh and E.G. Williams. Complex Wave-Number Decomposition of Structural Vibrations. *Journal of Acoustical Society of America*, 93:836–848, 1993.

[21] J.H. Heo, Y.W. Kho, H. Shin, S. Kim, and T. Kim. Regression Equations of Probability Plot Correlation Coefficient Test Statistics from Several Probability Distributions. *Journal of Hydrology*, 355:1–15, 2008.

[22] K. Huang, H.C. Chen, and C.R. Chen. Vertical Riser VIV Simulation in Uniform Current. *Journal of Offshore Mechanics and Arctic Engineering*,

132:1–10, 2010.

[23] E. Huse, G. Kleiven, and F.G. Nielsen. Large Scale Model Testing of Deep Sea Risers. In *Proceedings of the Offshore Technology Conference*, Paper no. 8701, Houston, USA, 1998.

[24] N. Jauvtis and C.H.K. Williamson. The Effect of Two Degrees of Freedom on Vortex-Induced Vibration at Low Mass and Damping. *Journal of Fluid Mechanics*, 509:23–62, 2004.

[25] V.G. Jhingran. *Drag Amplification and Fatigue Damage in Vortex-Induced Vibration*. PhD Dissertation, Massachusetts Institute of Technology, Cambridge, MA, 2008.

[26] V.G. Jhingran and J.K. Vandiver. Incorporating the Higher Harmonics in VIV Fatigue Predictions. In *26th International Conference on Offshore Mechanics and Arctic Engineering, OMAE 2007*, Paper no. 29352, San Diego, USA, 2007.

[27] J. Jong. *The Quadratic Correlation between In-Line and Cross-Flow, Vortex-Induced Vibration of Long Flexible Cylinders*. PhD Dissertation, Massachusetts Institute of Technology, Cambridge, MA, 1984.

[28] P.M. Josefsson and C. Dalton. An Analytical/Computational Approach in Assessing Vortex-Induced Vibration of a Variable Tension Riser. *Journal of Offshore Mechanics and Arctic Engineering*, 132:1–7, 2010.

[29] A. Khalak and C.H.K. Williamson. Motions, Forces and Mode Transitions in Vortex-Induced Vibrations at Low Mass-Damping. *Journal of*

Fluids and Structures, 13:813–851, 1999.

[30] T. Kijewski and A. Kareem. Wavelet Transforms for System Identification in Civil Engineering. *Computer-Aided Civil and Infrastructure Engineering*, 18:339–355, 2003.

[31] G. Kleiven. Identifying VIV Vibration Modes by Use of the Empirical Orthogonal Functions Technique. In *21st International Conference on Offshore Mechanics and Arctic Engineering, OMAE 2002*, Paper no. 28425, Oslo, Norway, 2002.

[32] C.M. Larsen, R. Yttervik, K. Vikestad, and E. Passano. Empirical Model for Analysis of Vortex Induced Vibrations - Theoretical Background and Case Studies. In *20th International Conference on Ocean, Offshore and Arctic Engineering, OMAE 2001*, Paper no. 1203, Rio de Janeiro, Brazil, 2001.

[33] H. Lie and K.E. Kaasen. Modal Analysis of Measurements from a Large-Scale VIV Model Test of a Riser in Linearly Sheared Flow. *Journal of Fluids and Structures*, 22:557–575, 2006.

[34] J.H. Lienhard. Synopsis of Lift, Drag, and Vortex Frequency Data for Rigid Circular Cylinders. *Washington State University, College of Engineering, Research Division Bulletin 300*, 1966.

[35] N.R. Lomb. Least-Squares Frequency Analysis of Unequally Spaced Data. *Astrophysics and Space Science*, 39:447–462, 1976.

[36] D. Lucor, H. Mukundan, and M.S. Triantafyllou. Riser Modal Identification in CFD and Full-Scale Experiments. *Journal of Fluids and Structures*, 22:905–917, 2006.

[37] H. Marcollo, H. Chaurasia, and J.K. Vandiver. Phenomena Observed in VIV Bare Riser Field Tests. In *26th International Conference on Ocean, Offshore and Arctic Engineering, OMAE 2007*, Paper no. 29562, San Diego, USA, 2007.

[38] M. Matsuishi and T. Endo. Fatigue of Metals Subjected to Varying Stress. In *Japan Society of Mechanical Engineers*, Jukvoka, Japan, 1968.

[39] J.G. McDaniel and W.S. Shepard, Jr. Estimation of Structural Wave Numbers from Spatially Sparse Response Measurements. *Journal of Acoustical Society of America*, 108:1674–1682, 2000.

[40] Y. Modarres-Sadeghi, H. Mukundan, J.M. Dahl, F.S. Hover, and M.S. Triantafyllou. The Effect of Higher Harmonic Forces on Fatigue Life of Marine Risers. *Journal of Sound and Vibration*, 329:43–55, 2010.

[41] H. Mukundan. *Vortex-Induced Vibration of Marine Risers: Motion and Force Reconstruction from Field and Experimental Data.* PhD Dissertation, Massachusetts Institute of Technology, Cambridge, MA, 2008.

[42] H. Mukundan, Y. Modarres-Sadeghi, J.M. Dahl, F.S. Hover, and M.S. Triantafyllou. Monitoring VIV Fatigue Damage on Marine Risers. *Journal of Fluids and structures*, 25:617–628, 2009.

[43] M.S. Pantazopoulos. Vortex-Induced Vibration Parameters: Critical Review. In *13th International Conference on Offshore Mechanics and Arctic Engineering - OMAE*, volume 1, pages 199–255, 1994.

[44] W.H. Press, S.A. Teukolsky, W.T. Vetterling, and B.P. Flannery. Numerical Recipes in C: The Art of Scientific Computing. Chapter 13.8 Spectral Analysis of Unevenly Sampled Data. Cambridge University Press, Second Edition, 1992.

[45] T. Sarpkaya. Vortex-Induced Oscillations. *Journal of Applied Mechanics*, 46:241–258, 1979.

[46] T. Sarpkaya. A Critical Review of the Intrinsic Nature of Vortex-Induced Vibrations. *Journal of Fluids and Structures*, 19:389–447, 2004.

[47] J.D. Scargle. Studies in Astronomical Time Series Analysis II: Statistical Aspects of Spectral Analysis of Unevenly Spaced Data. *Astrophysical Journal*, 263:835–853, 1982.

[48] T. Srivilairit and L. Manuel. Vortex-Induced Vibration and Coincident Current Velocity Profiles for a Deepwater Drilling Riser. In *26th International Conference on Offshore Mechanics and Arctic Engineering, OMAE 2007*, Paper no. 29596, San Diego, USA, 2007.

[49] S.B. Swithenbank. *Dynamics of Long Flexible Cylinders at High-Mode Number in Uniform and Sheared Flows.* PhD Dissertation, Massachusetts Institute of Technology, Cambridge, MA, 2007.

[50] S.B. Swithenbank and J.K. Vandiver. Identifying the Power-In Region for Vortex-Induced Vibrations of Long Flexible Cylinders. In *26th International Conference on Ocean, Offshore and Arctic Engineering, OMAE 2007*, Paper no. 29156, San Diego, USA, 2007.

[51] M.A. Tognarelli, S.T. Slocum, W.R. Frank, and R.B. Campbell. VIV Response of a Long Flexible Cylinder in Uniform and Linearly Sheared Currents. In *Proceedings of the Offshore Technology Conference*, Paper no. 16338, Houston, Texas, 2004.

[52] M.A. Tognarelli, S. Taggart, and M. Campbell. Actural VIV Fatigue Response of Full Scale Drilling Risers: with and without Suppression Devices. In *27th International Conference on Offshore Mechanics and Arctic Engineering, OMAE 2008*, Paper no. 57046, Estoril, Portugal, 2008.

[53] M.S. Triantafyllou, G.S. Triantafyllou, Y.S.D. Tein, and B.D. Ambrose. Pragmatic Riser VIV Analysis. In *Proceedings of the Offshore Technology Conference*, Paper no. 10931, Houston, USA, 1999.

[54] A.D. Trim, H. Braaten, H. Lie, and M.A. Tognarelli. Experimental Investigation of Vortex-Induced Vibration of Long Marine Risers. *Journal of Fluids and Structures*, 21:335–361, 2005.

[55] J.K. Vandiver. Dimensionless Parameters Important to the Prediction of Vortex-Induced Vibration of Long, Flexible Cylinders in Ocean Currents. *Journal of Fluids and Structures*, 7:423–455, 1993.

[56] J.K. Vandiver and L. Li. *SHEAR7 V4.4 Program Theoretical Manual*. Massachusetts Institute of Technology, Cambridge, MA, 2005.

[57] J.K. Vandiver and C.H. Mazel. A Field Study of Vortex Excited Vibrations of Marine Cables. In *Proceedings of the Offshore Technology Conference*, Paper no. 2491, Houston, USA, 1976.

[58] J.K. Vandiver, S.B. Swithenbank, V. Jaiswal, and V.G. Jhingran. Fatigue Damage from High Mode Number Vortex-Induced Vibration. In *25th International Conference on Offshore Mechanics and Arctic Engineering, OMAE 2006*, Paper no. 9240, Hamburg, Germany, 2006.

[59] J.K. Vandiver, S.B. Swithenbank, V. Jaiswal, and H. Marcollo. The Effectiveness of Helical Strakes in the Suppression of High-Mode-Number VIV. In *Proceedings of the Offshore Technology Conference*, Paper no. 18276, Houston, USA, 2006.

[60] V. Jaiswal and J.K. Vandiver. VIV Response Prediction for Long Risers with Variable Damping. In *26th International Conference on Offshore Mechanics and Arctic Engineering, OMAE 2007*, Paper no. 29353, San Diego, USA, 2007.

[61] L. Wilhoit, C. Supan, E.K. Albaugh, and C. Jones. 2010 Deepwater Solutions and Records for Concept Selection. *Offshore magazine*, May 2010. `http://offshore-mag.com`.

[62] C.H.K. Williamson and R. Govardhan. Vortex-Induced Vibrations. *Annual Review of Fluid Mechanics*, 36:413–455, 2004.

[63] C.H.K. Williamson and R. Govardhan. A Brief Review of Recent Results in Vortex-Induced Vibrations. *Journal of Wind Engineering and Industrial Aerodynamics*, 96:713–735, 2008.

Vita

Chen Shi was born in Baoji, China on August 3rd, 1979, the son of Mr. Xinkui Shi and Mrs. Enfang Peng. He received the degree of Bachelor of Science in Civil Engineering in 2001 and the degree of Master of Science in Civil Engineering in 2004 from Tongji University. He entered the doctoral program in the Department of Civil, Architectural and Environmental Engineering at the University of Texas at Austin in 2006.

Permanent address: 45 Xibao Rd Apt 7-19-9
Baoji, Shaanxi, China 721006

This dissertation was typeset with LaTeX[†] by the author.

[†] LaTeX is a document preparation system developed by Leslie Lamport as a special version of Donald Knuth's TeX Program.